



UNIVERSITÀ
DEGLI STUDI
DI PADOVA

Sede Amministrativa: Università degli Studi di Padova

Dipartimento di Ingegneria Meccanica – Settore Materiali

SCUOLA DI DOTTORATO DI RICERCA IN : SCIENZA E INGEGNERIA DEI MATERIALI
CICLO XXII

**HYDROGEN STORAGE IN METAL AND COMPLEX HYDRIDES: FROM POSSIBLE NICHE
APPLICATIONS TOWARDS PROMISING HIGH PERFORMANCE SYSTEMS**

Direttore della Scuola : Ch.mo Prof. Gaetano Granozzi

Supervisore : Ch.mo Prof. Giovanni Principi

Dottorando : Filippo Agresti

A me tremavano un po' le gambe; provavo paura retrospettiva, e insieme una certa sciocca fierezza, per aver confermato un'ipotesi, e per aver scatenato una forza della natura. Era proprio idrogeno, dunque: lo stesso che brucia nel sole e nelle stelle, e dalla cui condensazione si formano in eterno silenzio gli universi.

Primo Levi

Il Sistema Periodico

Contents

Abstract	V
Sommario	VII
List of abbreviations	IX
Preface	1
Chapter 1 - The hydrogen and the need of a hydrogen based economy	7
1.1 The properties of hydrogen	7
1.3 The hydrogen as future energy carrier	8
1.4 The production of hydrogen	11
1.4.1 The production from fossil sources	11
1.4.2 The production from alternative sources	12
1.5 The problem of hydrogen storage	14
Chapter 2 - The hydrogen storage in metal hydrides	19
2.1 Introduction	19
2.2 Hydrogen absorption/desorption dynamics in metal hydrides	20
2.3 Thermodynamics	21
2.3.1 The Van't Hoff law and the stability of metal hydrides	21
2.3.2 The stability of ternary metal hydrides and the Miedema's rule	25
2.3.3 Destabilization of metal hydrides	26
2.3.4 Nanoscale metal hydrides	27
2.3 Kinetics	28
2.3.1 Solid state kinetic models	29
2.4 Hydrogen storage compounds	31
2.4.1 Binary and intermetallic hydrides	31
2.4.2 Mg and Mg-based hydrides	33
2.4.3 Complex metal hydrides	38
Chapter 3 - Preparation and characterization techniques	51

3.1 Introduction	51
3.2 The mechanical alloying and high energy ball milling	51
3.3 X-ray diffraction	55
3.3.1 The Bragg law	55
3.3.2 Instrumental setup	56
3.3.3 The Rietveld method	57
3.4 Gas reaction controlling with a volumetric Sievert's apparatus	58
3.5 Measurement of Specific Surface Area of solids by BET method	60

Chapter 4 - Reaction of hydrogen with the $\text{TiCr}_{1.78-x}\text{Mn}_x$ Laves

phase (C14) 65

4.1 Motivation for this study	65
4.2 Sample preparation and analysis of $\text{TiCr}_{1.78-x}\text{Mn}_x$ alloy	66
4.3 Structure of the $\text{TiCr}_{1.78-x}\text{Mn}_x$ alloy as cast and cycled	67
4.4 Thermodynamics of hydrogen a/d by the $\text{TiCr}_{1.78-x}\text{Mn}_x$ alloy	69

Chapter 5 - Hydrogen storage in Mg-Al based pellets 75

5.1 The problem of Mg-based upscaled system degradation with cycling	75
5.2 Samples preparation and analysis	77
5.3 Cycling of pellets	77
5.4 Structural analysis and PCI of pellets	80

Chapter 6 - Effect of high energy ball milling on the hydrogen storage

properties of Li-Mg-N-H system 89

6.1 The Li-Mg-N-H system	89
6.2 preparation of samples	90
6.3 Structure of milled, activated and cycled samples	91

Chapter 7 - Mechano-chemical direct synthesis of LiBH_4 and

improvement of decomposition kinetics 99

7.1 LiBH_4 , an intensively studied complex hydride	99
7.2 Direct mechanochemical synthesis of LiBH_4	101
7.2.1 Preparation of samples	101
7.2.2 dehydrogenation profiles of as milled samples	101
7.2.3 Structure and thermodynamics of synthesised samples	102
7.3 Improvement of dehydrogenation kinetics of LiBH_4 dispersed on modified multi-walled carbon nanotubes	105
7.3.1 Preparation of samples	105
7.3.2 Kinetic, structural and morphological characterization of samples	106
7.3.3 Interpretation of kinetic mechanism	108
7.3.4 Thermodynamic characterization	110

Chapter 8 - Concluding remarks 115

Curriculum Vitae 117

Acknowledgements 121

Abstract

A promising alternative to hydrogen storage in high pressure cylinders and cryogenic tanks is the hydrogen storage in solid form as metal hydrides or complex metal hydrides. However, much research is still necessary in this direction. In particular, the optimal pressure and temperature of operation for the use of a hydride-based tank in a PEM fuel cell-powered vehicle should remain in the of 1-10 atm and 25-120 °C, respectively. The further difficulty is related to the weight of the storing materials, which is still too high for efficient mobile applications compared to the amount of stored hydrogen.

The work reported in this thesis deals with systems belonging to several hydride classes such as complex hydrides, interstitial metal hydrides and magnesium-based hydrides. Improvements from the point of view of thermodynamic and kinetic properties are proposed and discussed on systems almost ready for niche applications and on other very promising systems but still far from hydrogen storage applications. Among the classical interstitial hydrides-forming alloys, the interaction of hydrogen with $\text{TiCr}_{1.78-x}\text{Mn}_x$ alloys, one of the most promising for the use in high pressure-solid state hybrid tanks, has been studied. Among the Mg-based hydrides, a compacted Mg-Al-based material is proposed in order to overcome the degradation problems found during the scaling up of MgH_2 as hydrogen storage medium. Concerning the complex hydrides, the kinetics improvement of the Li-Mg-N-H system by high energy ball milling processing is discussed and the problem of reversibility and slow decomposition kinetics of LiBH_4 has been faced.

Sommario

Una promettente alternativa allo stoccaggio dell'idrogeno in bombole ad alta pressione e in contenitori criogenici è lo stoccaggio dell'idrogeno allo stato solido utilizzando idruri metallici o idruri complessi. In ogni caso, molta ricerca è ancora necessaria in questa direzione. In particolare, la pressione e la temperatura di lavoro ottimali per un serbatoio da utilizzare in una vettura basata su celle a combustibili PEM dovrebbero rimanere rispettivamente negli intervalli 1-10 atm e 25-120 °C. L'ulteriore difficoltà è legata al peso dei materiali assorbenti, che è ancora troppo elevato rispetto alla quantità di idrogeno stoccata per applicazioni veicolari efficienti.

Il lavoro riportato in questa tesi riguarda sistemi appartenenti a diverse classi di idruri come idruri complessi, idruri metallici interstiziali, idruri a base di magnesio. Vengono proposti e discussi miglioramenti dal punto di vista termodinamico e cinetico apportati a sistemi ormai quasi pronti ad applicazioni di nicchia e ad altri molto promettenti ma ancora lontani da applicazioni per lo stoccaggio dell'idrogeno. Per quanto riguarda i classici idruri interstiziali, è stata studiata l'interazione dell'idrogeno con le leghe $\text{TiCr}_{1.78-x}\text{Mn}_x$, tra le più promettenti per l'utilizzo in serbatoi ibridi ad alta pressione. Riguardo gli idruri a base di magnesio, un materiale basato su Mg-Al compattato in pastiglie viene proposto per ovviare ai problemi legati allo "scaling-up" del MgH_2 . Per quanto riguarda la classe degli idruri complessi, viene discusso il miglioramento delle cinetiche di assorbimento/desorbimento di idrogeno grazie al trattamento con macinazione ad alta energia e vengono affrontati i problemi della reversibilità e della lenta cinetica di decomposizione del LiBH_4 .

List of abbreviations

a/d	absorption/desorption
BET	Brunauer-Emmett-Teller Theory
BM	Ball Milling
DSC	Differential Scanning Calorimetry
ESEM	Environmental Scanning Electron Microscope
LPG	Liquefied Petroleum Gas
MTBE	Methyl <i>tert</i> -Butyl Ether
MWCNTs	Multi-Walled Carbon Nanotubes
PCI	Pressure-Composition Isotherms
PEM	Polymeric Exchange Membrane
SMR	Steam Methane Reforming
SSA	Specific Surface Area
TPD	Thermal Programmed Desorption
XRD	X-Ray Diffraction

Preface

The continuous growth of world population and economic expansion of developing countries attempting to comply with the standards of the already industrialized countries, are among the causes of the increasing demand for energy and the alarming and continuous release of greenhouse gases. The technological challenge of our day is certainly satisfying the energy demand while maintaining the emission of greenhouse gases like methane (CH₄), nitrous oxide (N₂O), halocarbons, water vapour and especially CO₂, low enough to not disturb the environmental balance. Apart from water vapour, whose abundance depends on heating of seas and oceans, other greenhouse gases are directly emitted by human activities [1]. Anyway, the typical cause of global warming is believed to be carbon dioxide, the main end product of the use of fossil fuels during the production of thermal, mechanical and electrical energy. At the beginning of the 20th century the concentration of CO₂ in atmosphere was about 280 ppm, while the mean concentration in 2005 was about 379 ppm. The estimated growth rate of CO₂ in the atmosphere during the decade 1995-2005 is about 1.9 ppm yr⁻¹, the largest observed for any decade of the last 200 years [2]. As shown in fig. 1.1 the growth of the concentration of CO₂ and other greenhouse gases in the atmosphere during the industrial era has considerably affected the global temperature.

Globally, about 30% of CO₂ emissions into the atmosphere is caused by vehicles. If the level of technology for energy production and transport remains the same as today, for the near future a continuing rise in CO₂ emissions with a consequent increase of its concentration

in the atmosphere are expected. Fig. 2 shows the estimates of IPCC (Intergovernmental Panel on Climate Change) in a scenario of full economic development.

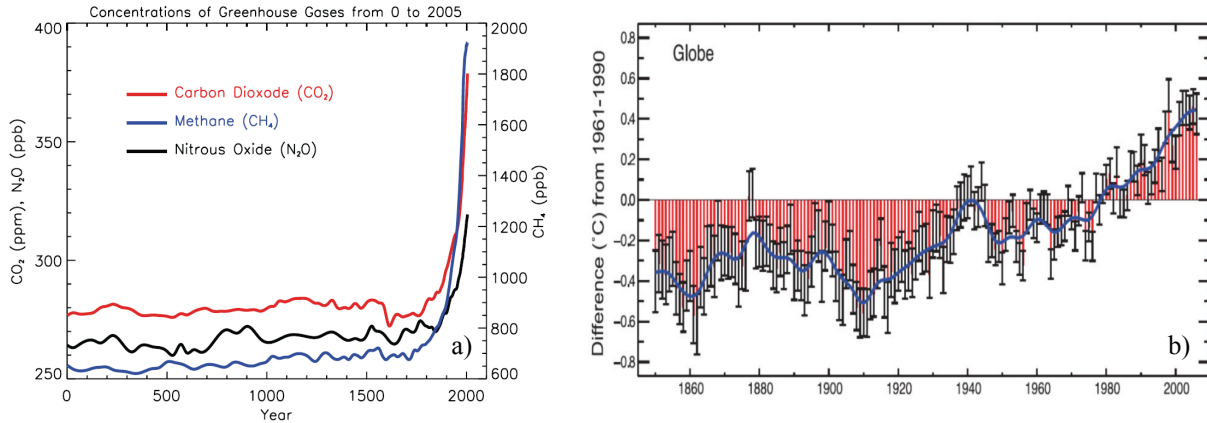


Figure 1. a) Atmospheric concentrations of main greenhouse gases over the last 2000 years [1]. b) Global and hemispheric annual combined land-surface air temperature for 1850 to 2006 [3].

As can be seen, the scenario is anything but reassuring, with a forecast for 2100 of a concentration of carbon dioxide beyond double than the preindustrial concentration. The challenge could only be win by increasing the efficiency of energy conversion systems and the simultaneous reduction in the consumption of hydrocarbons, with the expansion of sources with low or zero carbon dioxide emission, like natural gas, renewables, nuclear energy, confinement of produced CO_2 . Such a scenario should ideally be based on an energy carrier with the following characteristics:

- environmental impact, both global and local, almost zero;
- producible from several primary energy sources, interchangeable and available on a large scale in the future;
- preferentially distributed through a network.

The most promising energy carrier to satisfy these features is hydrogen. The advantages of hydrogen are various: low weight; amount of stored energy well above the current used fuels on a large scale such as diesel, natural gas or gasoline; absence of carbon dioxide, sulphur oxides and particulate in the exhausted gases. However, there are still many hurdles to overcome for hydrogen to become the energy carrier of the future. Hydrogen does not occur in nature as molecular hydrogen for immediate use but, as one of the most abundant elements on the Earth's crust, it must be extracted from water or hydrocarbons. To do that it is required to spend some energy, that is stored in the produced hydrogen and then converted using systems such as internal combustion engines or the more efficient fuel cells. Besides looking

for more efficient conversion systems, a major effort is being done to search for hydrogen storage systems, particularly for vehicular applications. The existing storage systems present several problems for vehicle applications, mainly related to safety and amount of stored hydrogen, in the case of gas in cylinders at high pressure, or energy necessary to obtain hydrogen in the liquid form and losses by evaporation, in the case of cryogenic tanks. An alternative is the storage in solid form. The most studied systems are metal hydrides, complex hydrides, chemical hydrogen storage carriers based on atomic hydrogen chemisorption and carbon nanotubes, zeolites, metal-organic frameworks (MOF), based on molecular hydrogen physisorption. However, much research is still necessary to improve this kind of materials. In particular, the optimal pressure and temperature of operation for a PEM fuel cell based vehicle should remain in the pressure and temperature intervals of 1-10 atm and 25-120 ° C, respectively [5]. The further difficulty is the weight of these materials, which is still too high for efficient mobile applications compared to the amount of stored hydrogen.

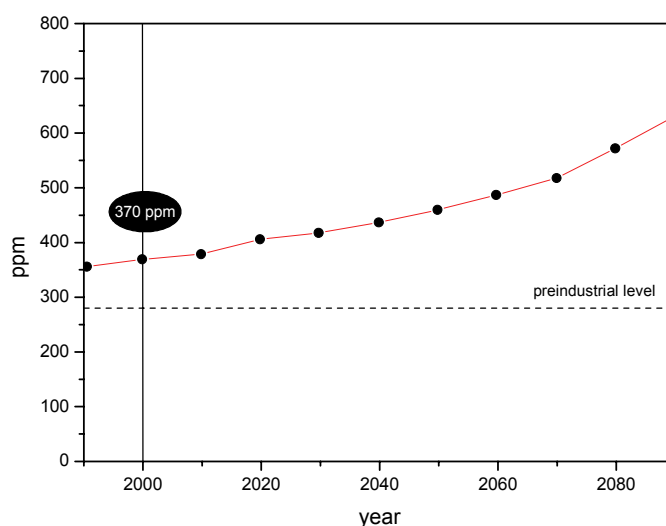


Figure 2. Prevision for CO₂ concentration in the atmosphere for the next years in a scenario of full economic development [4].

The current volumetric and gravimetric hydrogen storage targets of DOE (The American Department Of Energy) to be reached within 2010 are, respectively, 45 g/L and 6 wt% [6]. Much research has been addressed in the last years to metal and complex hydrides as good candidates to reach these targets in the field of hydrogen storage. The work reported in this thesis deals with systems belonging to several hydride classes such as complex hydrides, interstitial metal hydrides and magnesium-based hydrides. **Chapter 1** introduces basic information about hydrogen, the hydrogen-based economy and the problem of hydrogen storage; **Chapter 2** concerns literature data and theory about the hydrogen storage in metal hydrides, that is the main topic of the thesis, and includes an overview of the principal classes of solid state hydrogen systems; **Chapter 3** deals with preparation procedures, and

experimental techniques used during the work; from **Chapter 4** to **Chapter 7** four solid state hydrogen storage systems are presented, starting from the ones that more easily could be used in large scale or niche applications and moving towards other promising but still far from practical use. In **Chapter 4** the effect of Mn concentration in the $\text{TiCr}_{1.78-x}\text{Mn}_x$ Laves phases on the interaction with hydrogen is presented and discussed. **Chapter 5** deals with a hydrogen storage system based on Al-doped catalysed magnesium in the form of pellets. The main concern of **Chapter 6** is the effect of high energy ball milling on the absorption/desorption kinetics of the composite system $\text{LiNH}_2/\text{MgH}_2$. The topic of **Chapter 7** is LiBH_4 , one of the most studied and promising hydrogen storage materials due to its high theoretical gravimetric hydrogen capacity (18.4 wt%), but still far from being used practically for this purpose; particularly a novel mechano-chemical synthetic route and the improvement of decomposition kinetics through dispersion on multi-walled carbon nanotubes are presented. Finally, in **Chapter 8** conclusions and comments on the experimental results shown in the previous chapters are reported.

-
- [1] Forster, P., V. Ramaswamy, P. Artaxo, T. Berntsen, R. Betts, D.W. Fahey, J. Haywood, J. Lean, D.C. Lowe, G. Myhre, J. Nganga, R. Prinn, G. Raga, M. Schulz and R. Van Dorland, 2007: Changes in Atmospheric Constituents and in Radiative Forcing. In: *Climate Change 2007: The Physical Science Basis. Contribution of Working Group I to the Fourth Assessment Report of the Intergovernmental Panel on Climate Change* [Solomon, S., D. Qin, M. Manning, Z. Chen, M. Marquis, K.B. Averyt, M. Tignor and H.L. Miller (eds.)]. Cambridge University Press, Cambridge, United Kingdom and New York, NY, USA.
- [2] Core Writing Team, R. K. Pachauri, A. Reisinger, *Climate change 2007: Synthesis report*. IPCC Plenary XXVII (Valencia, Spain, 12-17 November 2007)
- [3] DOE Hydrogen program, 2005 Annual Progress Report, November 2005, available at: http://www.hydrogen.energy.gov/annual_progress05.html.
- [4] Multi-Year Research, Development and Demonstration Plan: Planned Program Activities for 2005-2015, Hydrogen Storage, available at: <http://www1.eere.energy.gov/hydrogenandfuelcells/mypp/index.html>
- [5] Ulf Bossel, *Well-to-Wheel Studies, Heating Values, and the Energy Conservation Principle*, European Fuel Cell Forum, 22 October 2003, available at: <http://www.efcf.com/reports/>
- [6] G. Principi, F. Agresti, A. Maddalena, S. Lo Russo, *The problem of hydrogen storage*, Energy (2009) **34**, 2087.

Chapter 1

The hydrogen and the need of an hydrogen-based economy

1.1 The properties of hydrogen

The hydrogen, discovered in 1776 by Henry Cavendish, is the most abundant element in the universe, but is not present in the atmosphere, being 14.4 times lighter than air. It is also one of the most abundant elements on the Earth's crust along with silicon and oxygen. Combined with oxygen, nitrogen and carbon is one of the key elements making up the plant and animal life. It is the lightest element, consisting only of a proton and an electron. In nature the isotope 2 called deuterium is also present, having also a neutron in the nucleus, but the hydrogen 1 is the predominant, being the 99.98 % of the natural mixture. The isotope 3, called tritium, with two neutrons in the nucleus, is produced only during nuclear reactions. Like many gaseous elements hydrogen is diatomic in nature, dissociating at high temperature. The gaseous hydrogen is a mixture of two different forms, the orthohydrogen (nuclei with parallel spins), which is about the 75% of the mixture, and the parahydrogen (with antiparallel spins). The hydrogen has the lowest boiling and melting points than any other substance except helium: solidifies at $-259.2\text{ }^{\circ}\text{C}$ and liquefies at $252.77\text{ }^{\circ}\text{C}$. At $0\text{ }^{\circ}\text{C}$ and at the pressure of 1 atm, it is in the gaseous form with a density of 0.089 g / liter. The atomic weight is 1.007 u.a. It combines easily with oxygen to form water. The reaction occurs slowly at low temperature but with explosive trend above $550\text{ }^{\circ}\text{C}$. The range of flammability is very wide, being between 4 and 75% by volume, and the range of detonation is between 18.5% and 59% by volume. The energy content of hydrogen per unit mass is higher than any other current fuel

[1.1], that directly comes from its *higher heating value*¹. Table 1.1 shows the main physical properties of molecular hydrogen.

Table 1.1 *Physical properties of molecular hydrogen* [1.2].

Molecular mass	2.01588 g/mole
Melting point	-259 °C (1,013 bar)
Boiling point	-253 °C (1,013 bar)
Critical temperature	-239,9 °C (12,98 bar)
Density (as a gas in standard conditions)	0.0838 Kg/m ³
Density (as a liquid at 253 °C)	70 Kg/m ³
Higher heating value	141.8 KJ/g
Lower heating value	119.9 KJ/g

In table 1.2 the heating values of hydrogen and of some common fuels are compared.

Table 1.2 *Heating values of some common fuels* [1.1].

Fuel	Higher heating value	Lower heating value
Hydrogen	141.8 KJ/g	119.9 KJ/g
Gasoline	47.5 KJ/g	44.5KJ/g
Diesel	47.5KJ/g	42.5 KJ/g
Methane	55.5 KJ/g	50.0 KJ/g

As can be seen, the heating values of hydrogen are by far the highest, which means that at the same mass hydrogen produces an amount of heat, and therefore energy, proportionally higher (e.g. 1 kg of hydrogen contains the same amount of energy of 2.1 kilograms of natural gas or 2.8 kg of gasoline).

1.2 The hydrogen as future energy carrier

Hydrogen is currently considered the best candidate as an energy carrier in the near future. In fact, hydrogen is a gas that burns in air according to the simple reaction:

¹ Defined as the amount of heat produced by complete combustion of a given quantity of fuel, where the water vapour produced by combustion is condensed and the heat is exploited. Similarly, the *lower heating value* is the amount of heat produced by complete combustion of a given quantity of fuel, where the water produced by combustion remains in the state of steam and heat is not exploited.



Since the only reaction product consists of pure water, in the case of an internal combustion engine the only pollutant is represented by water vapour and nitrogen oxides that are formed due to the high temperature of the process. Anyway, the amount of nitrogen oxides is far less compared to fossil fuels and no unburned hydrocarbons, sulfur dioxide (present especially in diesel fuel) or carbon dioxide are present. Hydrogen burns with a not bright flame at a flame temperature stoichiometrically higher than in methane (2127 °C against 1917 °C). Compared to methane, a triple volumetric amount is needed with hydrogen to get the same calorific value, but the flow velocity is three times higher. The required energy for ignition of hydrogen in air is considerably lower than of methane. Hydrogen is the ideal element for the fuel cell which, invented in 1839, has returned a subject of research in aerospace applications in the 60's after a century of lapse. A fuel cell is an electrochemical device that converts the energy of hydrogen directly into electricity and heat, without going through thermal cycles and therefore not affected by restrictions imposed on them by thermodynamics. In figure 3 it is shown schematically the operation of a fuel cell, which basically works similarly to a battery, producing electricity through an electrochemical process. Unlike a battery, however, the fuel cell consumes substances from outside and is therefore able to function without interruption, until the system is supplied with fuel and oxygen.

Hydrogen can be produced from fossil fuels, renewable energy sources, nuclear power. Concerning the production from renewable sources, the most clean and far more interesting, the processes are essentially two: using biomass or water. In the production of hydrogen from biomass none of the proposed processes to date have achieved an efficiency that can be exploited industrially, even if the premises are good. The production from water can be done through the splitting into its components (hydrogen and oxygen) through various processes, among which the most efficient is electrolysis. Schematically, the electrolytic process is the reaction:



The electrolysis is based on the inverse reaction occurring in fuel cells. Therefore, the entire process of production and consumption is environmentally sustainable if, as mentioned above, a corresponding amount of clean electricity is available to power the electrolysis process. One could immediately think to the sun as the source of this energy, exploitable through the use of photovoltaic conversion facilities. The current technology can be considered reliable and adequate, though not yet competitive. Indeed, through the use of photovoltaic, solar energy can produce electrolytic hydrogen and oxygen.

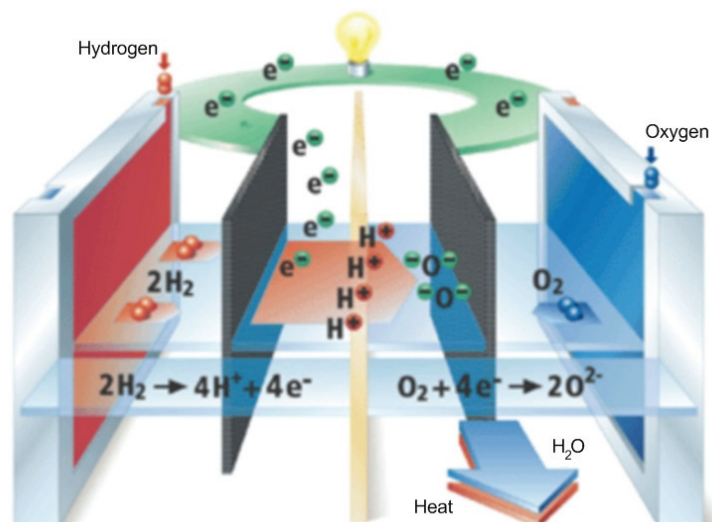


Figure 3. Working scheme of a fuel cell

As end product of the recombination of hydrogen and oxygen it generates a quantity of pure water almost equal to that of the starting one, thus closing the cycle with no emissions of pollutants. In principle, therefore, it would be possible to extract from water all the needed hydrogen in order to meet the clean energy needs of man kind. Actually, the problem is represented by costs. It is true that, virtually, it is possible to obtain pure hydrogen by electrolysis of water, but only when the technology will hopefully enable low cost production of electricity from renewable sources (or nuclear). The dissociation of water may also be obtained through thermochemical processes that need high temperature (800-1000 ° C) obtained from different sources (thermal solar energy, for instance). Research and development aimed to demonstrate the industrial feasibility of these processes are very interesting. Other processes are still studied in the laboratory scale, as photoconversion, which breaks down the water using biological or synthetic materials, and photoelectrochemistry, that uses the electric current generated by semiconductors.

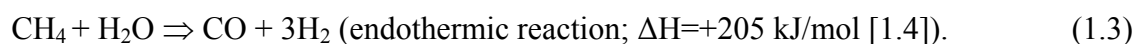
Hence, hydrogen is considered an ideal prospect for a future sustainable energy system, creating an incentive to the widespread use of renewable sources. In the short to medium term, hydrogen could be used in a transition technology making fossil fuels compatible with the environmental requirements. This, however, requires also the establishment of a wide system of integrated infrastructure to make the technological processes economic and reliable in all the stages (production, confinement of carbon dioxide generated in the process, transport, storage, end-use). In mobile applications there is not only the need to develop more efficient fuel cells, but also storage systems, transport and distribution networks comparable to those of conventional fuels.

1.3 The production of hydrogen

One of the key for the development of an hydrogen-based economy is a more efficient, cheap and environmentally acceptable hydrogen production. Nowadays, 95% of hydrogen is directly produced by companies that need it in industrial processes as an intermediate, as for the production of ammonia/urea or methanol, for the hydrogenation of organic compounds, in refineries, steel industries and so on. This production is mainly based on fossil fuels, using steam reforming of natural gas or gasification of coal. Production from renewable sources has only a few niche applications, in the case of electrolysis or gasification of biomass [1.3]. More details about the hydrogen production methods will be given in the next sections.

1.3.1 The production from fossil sources

More than the 48% of hydrogen is industrially produced by steam methane reforming (SMR). It is possible to apply this method also using hydrocarbons like ethane. It is not possible to use heavier hydrocarbons due to the high level of impurities they contain. About the heavier hydrocarbons, other methods like partial oxidation are more effective. The SMR is a reaction of methane with steam in presence of catalysts. On the industrial scale this reaction needs an operative temperature of 800 °C and a pressure of 2.5 MPa. The first stage consists of the methane decomposition to hydrogen and carbon monoxide. In the second stage, called “shift reaction”, carbon monoxide and water react to produce carbon dioxide and water. The chemical reaction that occur are the following:



The CO coming out from the "reformer" reacts with the steam, turning into CO₂ that is removed, producing pure hydrogen:



The neat reaction is then:



Actually, the process produces a mixture of CO, CO₂, H₂ and unreacted CH₄, called *syngas*, whose components must be separated. The efficiency of the process range between 60-80% depending on the scale of reformer [1.3]. In principle, large scale reformers are more efficient, but small scale reformers could be used in the next future in the hydrogen refuelling stations and for the direct use with fuel cells, since they operate at lower pressure and temperature (3

bar, 700 °C) [1.5]. In the traditional steam reforming the hydrocarbons are the source of both chemical and thermal energy: about 45% of used hydrocarbons is meant for the production of heat. The SMR is considerably cheap and convenient compared to other production methods like electrolysis. Moreover, the SMR involves a reduced impact on environment especially if combined with CO₂ confinement that is usually achieved by using alkaline solutions. A SMR plant that involves CO₂ has an electricity consumption that is about 60 % compared to traditional plants, mainly due to the need of CO₂ compression. But, it should be also considered that removing CO₂, the mixture has an higher heating value that leads to an higher efficiency of the furnace and, as a consequence, to a less methane consumption. The overall loss in efficiency is then about 5% [1.3].

An alternative production method is the coal and fossil fuels gasification. The process of gasification consists of partial, non catalytic, oxidation of a solid, a liquid or a gas with the aim of producing a gaseous fuel, mainly constituted by hydrogen, carbon monoxide and light hydrocarbons like methane. By means of gasification the coal is converted, partially or completely, in gaseous fuels that, after purification, can be used as fuels or as reagents in the industrial production of chemicals and fertilizers. The production of hydrogen by coal gasification is a technology with several commercial applications, but is competitive with the SMR only in the case the natural gas is too expensive or not easily available in the region. The process involves the reaction at high temperature (>800 °C) of pulverised and pre-treated coal with air (or oxygen) and steam, producing a mixture (*raw gas*) of H₂, CO, CO₂, traces of CH₄ and residual steam. As by-products of the process, it is also possible to find COS and H₂S that have to be removed from the raw gas. This gas mixture is then treated as in the case of the steam reforming in order to produce a stream of H₂ and CO₂. A plant for the gasification of coal is generally more complex than a the steam reforming plant due to several reasons: the coal has to be pre-treated before use (grinding, pulverization, etc.); need of an oxygen separation unit from air; need of a multi stage cleaning of raw syngas in order to remove particulate, sulphur, dust. The efficiency of these plants ranges between 60-70%, but considering the energy that is spent to remove sulphurs and CO₂, the efficiency drops to 49-53% [1.3].

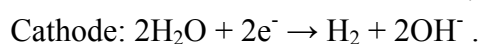
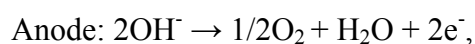
1.3.2 The production from alternative sources

Alternative hydrogen production routes are available, even though not competitive and not comparable with the production from fossil fuels. However, many efforts and research are being spent because these methods could become in the future the solution for the problem of CO₂ emissions and for the clean conversion of the energy produced from renewable sources to hydrogen.

One of the most mature methods is the gasification of biomass. The technology for production of hydrogen from biomass is strictly similar to the gasification of coal but, unlike the latter method, the gasification of biomass does not lead to the increase of CO₂

concentration in the atmosphere. Indeed, the biomass acts as a sink for carbon dioxide during the growing and then releases it during gasification. Thus, applying the technology of CO₂ sequestration, a large scale production of hydrogen from biomass could even lead to the decreasing of CO₂ concentration in the atmosphere. Even if the technology is mature, only small scale plants have been installed so far; the efficiency of these plants ranges within 50-60 % [1.3].

As seen in section 1.3, electrolysis of water, where water is decomposed using an electrochemical process, is the reverse process used in the fuel cells; a direct current and voltage are usually applied. The total process consists of two reactions occurring at the two electrodes:



Three types of electrolyzers are currently used: alkaline water electrolyzers, membrane electrolyzers (PEM electrolyzers) and high temperature electrolyzers. Alkaline water electrolyzers use the oldest and most common technology: a 20-40 % KOH solution is the electrolyte that flows between the electrodes made up of Ni or Cr-Ni; a diaphragm usually separates the two electrodes in order to avoid the mixing of the produced oxygen and hydrogen; the operating conditions of an alkaline water electrolyzers are temperature of 70-90 °C, cell voltage of 1.8-2.2 V, current density of 2-3 kA/m² and a power consumption of 4-5 kWh/Nm³ hydrogen. In these operating conditions the efficiency is 65-75% [1.5]. The PEM electrolyzers are in principle PEM fuel cells operating in reverse mode. The technology is still not competitive with alkaline electrolyzers due to higher electricity consumption. High temperature electrolyzers present an advantage from the point of view of efficiency because at working temperature of 800-1000 °C the electricity requirement decreases. This technology could be advantageous when the necessary heat is available from other processes.

Another way to split water in its elemental constituents is the thermochemical splitting. Actually, water can be split in H₂ and O₂ at temperatures above 2200 °C. Besides the high required temperature, the method is challenging due to the difficulty of separating hydrogen from oxygen at these temperatures. It is necessary to develop new materials and a cheap source of heat such as nuclear or solar thermal energy. It is possible to lower the operating temperature to 900 °C using two parallel thermal cycles that produce oxygen and hydrogen separately: the most common and promising is the sulphur-iodine process. However, the method is still a subject of basic research.

Solar energy can be directly used for hydrogen production using a photochemical process. The process needs a semiconductor having a band gap large enough to allow extraction of electrons from water, leading to water splitting. Photocatalysts can help the reaction, but the main drawback is their stability for long periods, being continuously in contact with water.

A challenging technology is the production of hydrogen from biological processes using micro-organisms. The process is based on the enzymatic conversion of electron and protons

into molecular hydrogen. There are three ways under study to achieve this purpose: hydrogen production from fermentation of biomass, photoproduction from bacteria and biophytolytic production by algae.

1.4 The problem of hydrogen storage

Besides the problem of finding the most efficient and economical way to produce hydrogen, still hindering its diffusion as an energy carrier, storage and transport are major concerns. Being hydrogen the lightest element, at 0 ° C and a pressure of 1 bar its density is only 0.090 kg/m³, while at -253 °C is a solid with a density of 70.6 kg/m³. It is obvious that it is not easy to store large amounts of hydrogen in gaseous form. With regard to mobile applications, the targets earlier set by the DOE (the Department of Energy of U.S.) are: 6.5 wt% (which expresses the percentage of the stored hydrogen mass vs. the mass of the tank) and 60 kgH₂/m³ (which represents the ratio of the mass of hydrogen vs. the volume of the tank). Recently, Since the 2005 targets have not been fulfilled [1.6], they have been modified to more realistic values: 5.5 wt% and 40 kgH₂/m³ to be reached within 2015 [1.7].

The unfamiliarity with the use of hydrogen as an energy source has raised several concerns regarding safety. Certainly, it is to recognize that hydrogen, because of its violent reaction with oxygen, should be treated with some caution. But it is also true that when hydrogen burns is consumed very rapidly, with flames directed upwards and with a thermal radiation of wavelength very low and easily absorbed by the atmosphere. By contrast, materials such as gasoline, diesel, LPG or natural gas are heavier than air and do not disperse, remaining a source of danger for much longer times. It was calculated, using experimental data, that the burning of gasoline vehicle lasts for 20-30 minutes, while for a hydrogen vehicle it does not last more than 1-2 minutes .

Currently, the most common method for hydrogen storage is the use of steel cylinders working at pressures up to 200 atm. However, in recent years cylinder with an experimental composite structure have been developed being able to work at pressures above 800 atm, and are then able to store 36 KgH₂/m³, about half of the density of liquid hydrogen. Further increase of working pressure would make the system too heavy because of the corresponding increase of the thickness of the cylinder walls to prevent dangerous leakages and explosions. Safety is a major concern regarding this method, especially for mobile applications. That is why in the future cylinders made of three layers will be used: an inner polymer, an intermediate carbon fiber capable of withstanding high stresses, an outer one protecting the system from mechanical and corrosive damages. The new cylinders are made up of aluminium reinforced externally by carbon-fiber composites, working at 450 atm, having passed the security test at 600 atm. The technology points to higher and higher pressures, but

repeated cycles of loading and unloading could induce the detachment of fibers from the polymer matrix, thus reducing the mechanical strength. Working at 450 atm it is possible to store about 4 wt% of H₂. The required high pressure is the major drawback for the use of this technology in mobile applications [1.8].

Hydrogen in liquid state appears very attractive for the high density (70.8 kg/m³ at 1 atm), but difficult for the low temperature boiling point at which must be led and maintained (-252 °C). Because of its low critical temperature (-239.9 °C), liquid hydrogen can be stored only in open systems, because above the critical temperature the liquid phase does not exist and the pressure in a closed system at room temperature could reach very high values. In addition, the major concerns of this technology are represented by the high costs required by the liquefaction process and the thermal insulation of the containers in order to limit losses due to the boiling off. The rate of boiling off from liquid hydrogen tank depends on the shape, the dimensions and the thermal insulation of the container. The losses can be reduced significantly for large containers (0.4% per day for a container-type Dewar of 50 m³ and 0.2% for one do 100 m³). Among the supporters of this technology there is the BMW company that in 2003 has developed in agreement with General Motors an automated system for the refuelling and has built a small fleet of cars with internal combustion engine fuelled by H₂. Nowadays, the cryogenic technology have reached a significant level thanks to the development of rockets (Shuttle, Ariane), but some drawbacks are against the exploit in vehicular applications: the cost of liquefaction and transport, evaporation and safety. Therefore, the widespread use of liquid hydrogen is still a concern [1.9].

One of the most promising technologies for hydrogen storage, especially for mobile applications, is the storage in solid form using hydrides. For this purpose metals, intermetallic compounds, alloys, complex hydrides are being studied. It is known that some metals and alloys are able to chemically absorb hydrogen and then to reversibly release it. At a given temperature and with a low hydrogen pressure, the host metal begins to dissolve a small quantity of hydrogen in solid solution (α -phase), after the dissociation of the H₂ molecule into atomic hydrogen at the surface of the material. When the pressure increases, the hydrogen concentration in the metal increases until the local interactions between hydrogen atoms become more and more important up to the nucleation and growth of the hydride phase β . As long as the solid solution and the hydride coexist, the pressure-composition isotherms (PCI curves) (hydrogen pressure at a given temperature as a function of hydrogen concentration in the material) present a plateau; the length of this plateau represents the hydrogen amount which can be reversibly stored at that temperature by small pressure changes. When the $\alpha \rightarrow \beta$ transition is completed, the hydrogen pressure again increases sharply with the concentration. The higher is the temperature the shorter is the length of the plateau pressure. The region of the diagram where the two phases coexist ends at a critical point T_C, over which the $\alpha \rightarrow \beta$ transition is direct. The equilibrium pressure (position of the plateau) strongly depends on the temperature and is related to the absolute values of enthalpy and entropy

changes, ΔH and ΔS , respectively. The working temperature of a metal/hydride system is fixed by the thermodynamic equilibrium pressure and by the overall reaction kinetics. In order to make metal hydrides interesting for the use in hydrogen reservoirs, the working pressure and temperature should be in the ranges from 1 to 10 bar and from -20 to 100 °C, respectively, corresponding to an enthalpy change between 28 and 48 kJ/mol of hydrogen. A further problem, already mentioned, concerns the weight of the absorbing material, thus light metal hydrides containing a high amount of hydrogen are preferable. Recently, hydrides of AB_5 (e.g. $LaNi_5$), AB (e.g. $FeTi$), AB_2 (e.g. ZrV_2) and A_2B (e.g. Mg_2Ni) types alloys have been commercialized and are supplied in special vessels. The weak point of this technology is the low gravimetric capacity (less than 1.5 wt%), which makes the reservoir too heavy for mobile applications [1.10]. The operating costs for a system based on hydrides include those related to the operations of cooling and heating during hydrogenation and dehydrogenation. The amount of heat required depends on the type of metal or alloy and its applications. In order to overcome these drawbacks, the research in this field is addressed towards light metal hydrides and complex hydrides of light metals. One of the most studied compounds is MgH_2 , due to its relatively high hydrogen gravimetric capacity (7.6 wt%). The use of magnesium presents two main difficulties. First, due to the high stability of $Mg-H$ bond, the plateau pressure of the system is too low in the temperature range of interest (it is only 0.36 mbar at 100 °C). In order to get desorption pressures near atmospheric, it is necessary to raise the temperature to about 300 °C. Moreover, even at 300 °C the hydrogenation and dehydrogenation reactions are extremely sluggish. It has been shown that the use of nanostructured magnesium hydride obtained by high energy milling is more convenient than the as received commercially produced crystalline material [1.11, 1.12]. The presence of sub-micrometric grains reduces the hydrogen diffusive path in solid phase and the high concentration of defects and grain boundaries offers preferential paths for hydrogen diffusion and nucleation sites for metallic Mg. Since Bogdanovich and Schwickardi [1.13] showed that $Na[AlH_4]$ can reversibly desorb and absorb hydrogen at moderate temperature and pressure if catalysed with a few mol% of Ti compounds, many efforts have been spent by the research on group I and II salts of $[AlH_4]^-$ (alanates), $[NH_2]^-$ (amides) and $[BH_4]^-$ (borohydrides) as materials for hydrogen storage. These compounds are very interesting due to their high gravimetric hydrogen capacity. Unlike interstitial metal hydrides, in these compounds hydrogen atoms are covalently coordinated by a central atoms in complex anions. The problems of many of these “complex” hydrides are the high decomposition temperature (when H_2 is released by the material) and the complexity of the recycling mechanism (reversibility possible only at high temperature and H_2 pressure). In order to overcome these problems, new synthetic routes for these materials have been studied, catalysts have been tested, confinement in nanostructures have been tried, but still the technology based on this class of materials is not ready for hydrogen storage applications [1.14].

- [1.1] Ulf Bossel, *Well-to-Wheel Studies, Heating Values, and the Energy Conservation Principle*, European Fuel Cell Forum, 22 October 2003, available at: <http://www.efcf.com/reports/>
- [1.2] Lide, D. R., ed., *Handbook of chemistry and physics* (1997), CRC Press LLC .
- [1.3] Mueller-Langer, F.; Tzimas, E.; Kaltschmitt, M. & Peteves, S., *Techno-economic assessment of hydrogen production processes for the hydrogen economy for the short and medium term*, International Journal of Hydrogen Energy (2007) **32**, 3797 - 3810 .
- [1.4] Hemmes K, De Groot A, Den Uil H, *Application potential of biomass related hydrogen production technologies to the Dutch energy infrastructure of 2020–2050* (2003), Energy Research Centre of the Netherlands (ECN).
- [1.5] Ball M., Wietschel M., *The Hydrogen Economy: Opportunities and Challenges*, Cambridge University Press.
- [1.6] FreedomCar & Fuel Partnership, *Hydrogen Storage Technologies Roadmap* (2005), available at: http://www.uscar.org/commands/files_download.php?files_id=82
- [1.7] Dillich S., *2009 DOE Hydrogen Program & Vehicle Technologies Program*, Merit Review and Peer Evaluation Meeting, 19th May 19 2009.
- [1.8] Irani R. S., *Hydrogen storage: high pressure gas containment*, MRS Bulletin (2002) 27, 680.
- [1.9] Wolf J., *Liquid-hydrogen technology for vehicles*, MRS Bulletin (2002) 27, 684.
- [1.10] G. Principi, F. Agresti, A. Maddalena, S. Lo Russo, *The problem of solid state hydrogen storage*, Energy (2009) 34, 2087.
- [1.11] G. Liang, J. Huot, S. Boily, A. van Neste and R. Schulz, *Catalytic effect of transition metals on hydrogen sorption in nanocrystalline ball milled MgH_2 -Tm (Tm = Ti, V, Mn, Fe and Ni) systems*, J Alloys Compd (1999) 292, 247
- [1.12] R. Schulz, J. Huot, G. Liang, S. Boily, G. Lalande and M.C. Denis *et al.*, *Recent developments in the applications of nanocrystalline materials to hydrogen technologies*, Mater Sci Eng A (1999) 267, 240.
- [1.13] Bogdanovich B., Schwickardi M., *Ti-doped alkali metal aluminium hydrides as potential novel reversible hydrogen storage materials*, J. Alloys Compd. (1998) 253-254, 1.

- [1.14] Orimo S., Nakamori Y., Eliseo J. R., Züttel A., Jensen C. M., *Complex hydrides for hydrogen storage*, Chem. Rev. (2007) 107, 4111.

Chapter 2

The hydrogen storage in metal hydrides

2.1 introduction

During the 60's it has been discovered that some intermetallic compounds such as Mg_2Ni , $LaNi_5$ and $TiFe$ can directly and reversibly react with hydrogen at temperatures of practical interest ($-20\div 380$ °C). These findings, accompanied by the oil and energy crisis of the 70's stimulated an intense research towards metal hydrides as hydrogen storage materials.

Several intermetallic compounds have the ability to store large quantities of hydrogen (with a ratio of hydrogen to metal atoms greater than 1), however most of these alloys composed of rare earth or transition metal show capabilities that do not go beyond $1\div 2$ wt% H_2 . Magnesium-based alloys are an exception, having a hydrogen capacity in the range $3.3\div 7.7$ wt%, and for this are very interesting.

So far, hundreds of metal hydrides that have been studied the potential practical use for the storage of hydrogen. The assessment is usually carried out considering the following points:

- Reversible hydrogen capacity;
- Range of operating pressure and temperature;
- Kinetics of the absorption/desorption (a/d) processes;
- Degradation of kinetics and storage capacity after repeated cycles of hydrogenation;
- Cost.

The hundreds of metal hydrides studied so far only partially meet the target parameters related to the points mentioned, and very often, where a target is satisfied another is not and vice versa. The research then proceeds in order to find the material that excels in all

considered aspects. In recent years this research has been extended to complex hydrides of light metals such as alanates, borohydrides, amides mixed with light metal hydrides. In this chapter details on the a/d dynamics, thermodynamics, kinetics and a review of metal hydrides and light metal hydrides is given.

2.2 Hydrogen absorption/desorption dynamics in metal hydrides

Considering the formation of a classical interstitial metal hydride, several interactions are responsible for hydrogen dissolving into the host lattice of a metal. The first one, the interaction of hydrogen molecule approaching the metal surface, is the Van der Waals force, which leads to physisorption, with typical energy $E_{\text{phys}} \approx 10 \text{ kJ}\cdot\text{mol}^{-1} \text{ H}$. Of course, not all the molecules colliding with the surface will remain attached, this depends on the geometry of impact and the surface site involved in the collision. The equilibrium distance for the physisorbed hydrogen molecule is about 0.2 nm from the metal surface. Afterwards, the molecule dissociate into two H atoms that are then chemisorbed at the surface. The molecule must overcome an activation barrier for dissociation that depends on the elements involved at the surface. Particularly, it has been found that the d electrons of the substrate tends to lower the barrier. Actually, for metals whose valence electrons are of type s , such as copper, the spontaneous dissociation of molecular hydrogen is not observed. At this stage, bound states are formed between the hydrogen orbital $1s$ and the states of the metallic substrate and the chemical bond has got an energy of 30÷60 kJ/mol H, which may vary slightly with the number of d electrons in the $3d$ series of transition metals [2.1]. The mobility of chemisorbed atoms on the surface allows them to interact and form a surface phase with a *fractional coverage*¹ sufficiently high. On surfaces that have a high concentration of lattice defects, as can be that of a catalyst, hydrogen is adsorbed preferentially at sites with high coordination and in the vicinity of steps. In fact, these sites, because of their unsaturation, have a higher chemical potential compared to a bulk site or to a mere surface site, thus showing a greater reactivity. In the next step atomic chemisorbed hydrogen diffuses through the layers below the surface, overcoming an activation barrier of approximately 40 kJ/mol. Then hydrogen can diffuse through interstitial sites in the bulk of the metal host overcoming another barrier that is of the order of 10 kJ/mol [2.2].

The presence of hydrogen results in a crystal lattice expansion proportional to the concentration of about 3-4 Å per atom of hydrogen. For concentration ratios of $H/M < 0.1$

¹ Defined as $\theta = \frac{n_o}{n_d}$, where n_o is the number of occupied sites and n_d the number of available ones.

(where H is the number of hydrogen atoms and M the number of metal atoms) hydrogen diffuses isothermally into the metal lattice and form a solid solution phase that will be called α in the following discussion.

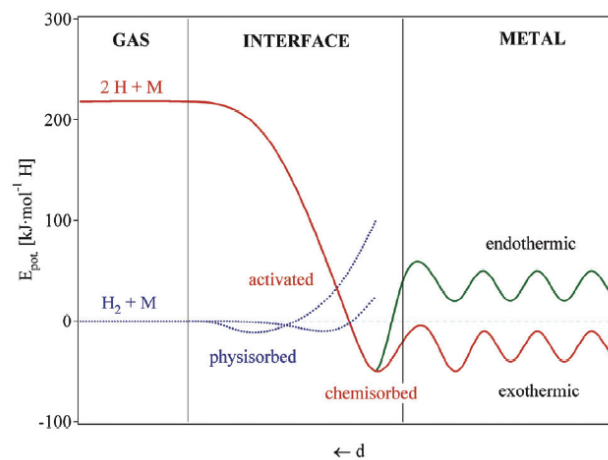


Figure 2.1 Potential energy curves for activated chemisorption on a metal surface and endothermic and exothermic solution in the bulk [2.1].

When the hydrogen concentration is high enough, usually when the ratio $H/M > 0.1$, the M-H interaction becomes important, resulting in the nucleation and growth of the metal hydride (β phase). During the coexistence of the α and β phases the volumetric expansion of the crystal lattice of the metal host can reach in many cases 10-20% and the ratio H/M can tend to 1 [2.3]. As a consequence, mechanical stress is accumulated at the grain boundaries, especially in brittle materials such as many intermetallic compounds, leading to the cracking of the material (*decrepitation*). The final hydride consists of a fine powder with a typical particle size of 10-100 μm [2.3].

2.3 Thermodynamics

2.3.1 The van't Hoff Law and the stability of metal hydrides

The purely thermodynamic aspects of the a/d processes are experimentally described by pressure-composition isotherms (PCI) usually obtained by volumetric or gravimetric measurements. An example of PCI curves obtained at different temperatures is schematically represented in Figure 2.2: the equilibrium pressure of the system is plotted as a function of the hydrogen dissolved into the material. When the solid solution α and hydride phase β coexist, the isotherms typically show a plateau whose length depends on the amount of hydrogen stored. In the region where all the material has been converted to the β phase, the hydrogen pressure starts to rise very rapidly with the hydrogen concentration. The top of the biphasic

region ends with a critical point T_C , above which the phase transition from α to β phase occurs continuously. The presence of a plateau in the biphasic region is ensured by the Gibbs' phase rule [2.4]:

$$F = 2 - \pi + N, \quad (2.1)$$

where F is the degree of freedom (and is equal to the number of independent variables which must be specified in order to fix the system, pressure and composition in this case), π is the number of present physical states in thermodynamic equilibrium with each other (solid, liquid and gas) and N is the number of components. In the monophasic region there are 2 physical states and 2 components and then both pressure and composition can be varied independently. Obviously, the addition of one more phase (the β phase during absorption) is counterbalanced by the loss of a degree of freedom and then the pressure doesn't change in the biphasic region.

Let's consider now a metal at certain temperature T being hydrogenated. Let's call a the concentration of hydrogen in the metal lattice when the plateau begins and b the concentration at which the plateau ends. We can write the following reaction related to the biphasic region:



that represents the absorption process of hydrogen in the host metal. This can be also written as:

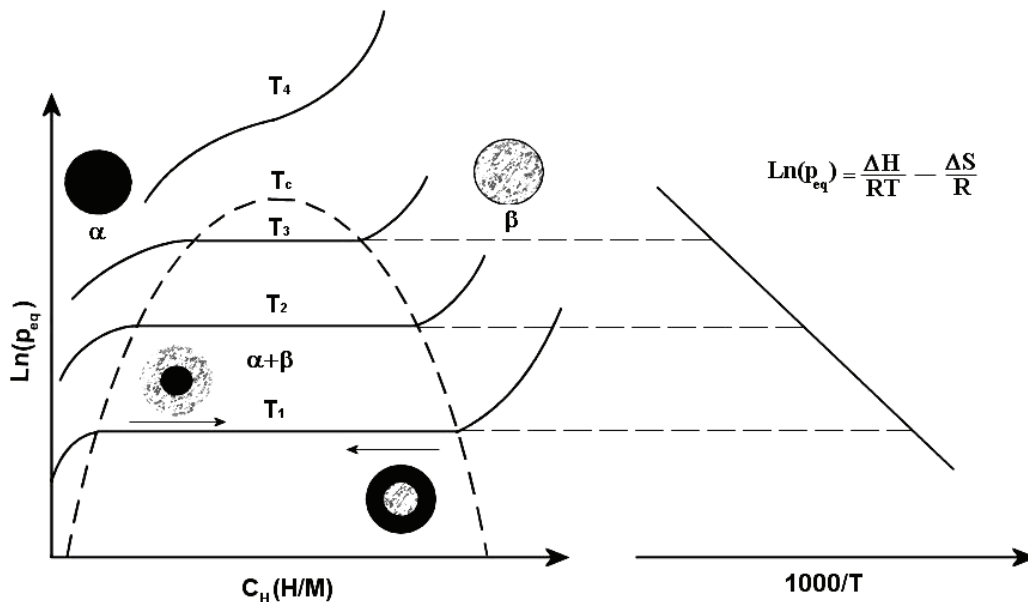


Figure 2.2 In the left hand side of the graph typical PCI absorption curves for a metal hydride are shown ($T_4 > T_3 > T_2 > T_1$). On the right hand side the construction of the van't Hoff plot is shown.

Since during a PCI the system is changing through equilibrium states, in each point of the curve the solid phase is in equilibrium with the gas phase, hence:

$$\frac{2}{b-a}(\mu_{MH_b} - \mu_{MH_a}) - \mu_{H_2} = 0, \quad (2.4)$$

where μ are the chemical potentials of the considered species. Analogously, in standard conditions the equation 2.4 becomes:

$$\frac{2}{b-a}(\mu_{MH_b}^0 - \mu_{MH_a}^0) - \mu_{H_2}^0 = \Delta G^0(a \rightarrow b), \quad (2.5)$$

where $\Delta G^0(a \rightarrow b)$ is the free energy change in standard conditions. Being MH_a and MH_b solids, it is reasonable to consider them in standard conditions in equation (2.4) too. Hence subtracting equation (2.4) from (2.5):

$$\Delta G^0(a \rightarrow b) = \Delta \mu_{H_2}^{plat} = RT \ln[p_{H_2}^{plat} (atm)]. \quad (2.6)$$

This is of course a value that remains constant by changing the plateau pressure and temperature, that are correlated quantities. Considering acceptable that the corresponding $\Delta H^0(a \rightarrow b)$ can be approximated with the heat of formation of the hydride ΔH^f , neglecting the partial heat of solubilisation of hydrogen into the solid solution, taking into account that $\Delta G^0(a \rightarrow b) = \Delta H^0(a \rightarrow b) - T \cdot \Delta S^0(a \rightarrow b)$ it is possible to write the equation (2.6) as:

$$\ln(p^{plat}) = \frac{\Delta H^f}{RT} - \frac{\Delta S^f}{R}. \quad (2.7)$$

This is the van't Hoff law, where ΔH^f and ΔS^f are the enthalpy and entropy of formation of the hydride, respectively. The entropy change corresponds essentially to the transition from molecular hydrogen to hydrogen dissolved in a solid and with a good approximation corresponds to the standard entropy of hydrogen ($S^0 = 130 \text{ J/K}\cdot\text{mol H}_2$), i.e. $\Delta S^f \approx -130 \text{ J/K}\cdot\text{mol H}_2$ for all the metal hydrides. This term leads to the evolution of heat during the absorption of hydrogen, $\Delta Q = T \cdot \Delta S$, which then makes the reaction exothermic; the same amount of heat must be provided in order to get the hydrogen desorbed. More significant, however, is the enthalpic term, it is in fact indicative of the stability of the metal-hydrogen bond. For instance, to get a pressure of 1 bar at 27 °C, i.e. the optimal conditions for practical applications, ΔH^f should be -39.2 kJ/mol H₂. The higher is this value, the greater the stability of the bond and therefore the higher the temperature at which it's possible to obtain a plateau pressure suitable for practical applications.

Both enthalpy and entropy of formation (or decomposition) can be obtained experimentally, the from the slope (the enthalpy) and from the intercept (the entropy) of the straight line in the Van't Hoff plot, as shown in Figure 2.2 and 2.3. The PCI curves present most often some hysteresis, and the plateau pressure is higher during absorption than during decomposition. This can happen for example if the mechanical stress accumulated during absorption is relaxed through plastic deformation [2.2].

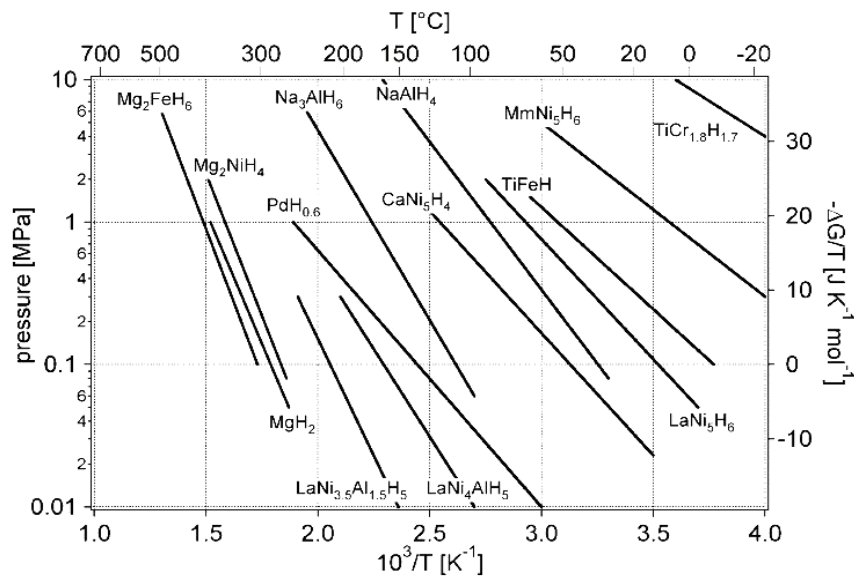


Figure 2.3 Van't Hoff plots of some metal hydrides [2.3].

There are several empirical models that allow the estimation of the stability and concentration of hydrogen in a metal hydride. The maximum amount of hydrogen corresponds to the number of interstitial sites for which the following two criteria can be applied: the distance between two hydrogen atoms occupying interstitial sites is at least 2.1 \AA [2.5] and the sphere that touches all nearest neighbours into the interstitial site that hosts the hydrogen atom must have a radius of at least 0.37 \AA [2.6]. Taking into account these values it can be found, in some cases, a theoretical density of hydrogen that is three times that of liquid hydrogen. Another general rule is that elements with electronegativity within 1.35 and 1.82 do not form stable hydrides, except for vanadium (1.45) and chromium (1.56) [2.7].

The stability of a binary hydride can be rationalized through a semiempirical model based on the electronic structure of the metal-hydrogen system. The absorption of hydrogen can be considered as an introduction of electrons and protons in the band structure of the host lattice. The electrons fill the empty states at Fermi level, while the presence of protons in the interstitial sites leads to a band with a strong s character that is around 4 eV below the Fermi level. The enthalpy of formation of binary hydrides MH_x is linearly correlated to the parameter $\Delta E = E_F - E_S$, where E_F is the energy of the Fermi level and E_S is the center of the lowest conduction band of the metal guest at occupied interstitial sites, which has a strong s character [2.8].

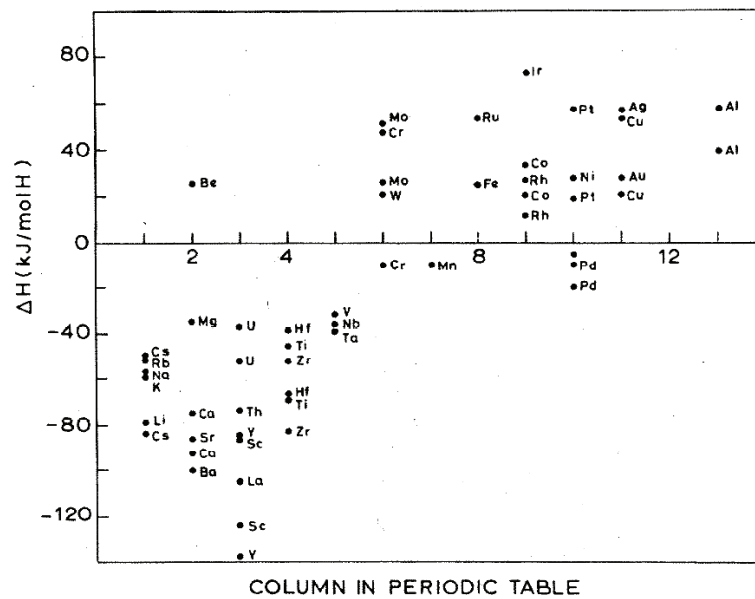


Figure 2.4 Enthalpies of formation of binary metal hydrides MH_x . Metals showing positive heats of formations don't lead spontaneously to hydrides. [2.8].

2.3.2 The stability of ternary metal hydrides and the Miedema's rule

Among the metals that react with hydrogen giving stable hydrides, only V and Mg fall in the range of temperature, pressure, and weight percentage of stored hydrogen interesting for applications. In particular, magnesium and Mg-based alloy raised a great interest especially for its high theoretical hydrogen content (7.6 wt%) and its low cost. Hydrogen reacts at high temperature with most of transition metals and their alloys to form hydrides. Electropositive elements such as yttrium, scandium, the lanthanides, actinides and elements belonging to the group of titanium and vanadium are the most reactive. The crystal structure usually remains that of the host metal, where the hydrogen is contained in octahedral or tetrahedral interstitial sites, or a combination of them. Only a small number of transition metal has no stable hydrides. Nevertheless, in the periodic table there is a considerable gap that ranges from group 6 (chromium) to group 11 (copper), in which the only hydrides are those of palladium ($PdH_{0.7}$), the unstable nickel hydride ($NiH_{<1}$) and the hydrides of chromium (CrH , CrH_2) and copper (CuH). Anyway, as discussed before, the simple binary hydrides except MgH_2 are not suitable for potential practical applications. More interesting are the hydrides of intermetallic compounds, because it is well known that by changing the metals that form the alloy it is possible to tailor the properties of the hydride and specially the thermodynamics. In the simplest case of ternary systems of the type AB_xH_n , the A element is typically a rare earth or alkaline earth metal, which tends to form a stable hydride, while the B component is a transition metal forming only unstable hydrides (Co, Ni, Cr, Fe, Mn or Al). An important feature of these compounds is that the operating pressure and temperature can be adjusted by

varying both the element A and B, so that the plateau pressure at a given temperature can be varied in this way even by two orders of magnitude. Basically, the larger the parameters of the host cell of the alloy, the lower the plateau pressure. In many cases it can be very advantageous to vary the x ratio to vary the characteristics of the PCI curves.

A semi-empirical model to predict the enthalpy of formation of ternary metal hydrides has been proposed by Miedema [2.9], also known as the “reverse stability” rule. According this rule the enthalpy of formation of a ternary metal hydride can be expressed in terms of binary enthalpies of formation:

$$\Delta H(AB_nH_{x+y}) = \Delta H(AH_x) + \Delta H(B_nH_y) - \Delta H(AB_n), \quad (2.8)$$

that means the more stable is the intermetallic host, the less stable is the hydride.

2.3.3 Destabilization of metal hydrides

In the previous section the common way to tailor the thermodynamic properties of metal hydrides has been introduced. The Miedema’s rule of “reverse stability” has been applied in that case to systems that do not undergo disproportionation during hydrogen cycling. This means that, starting from an unhydrogenated alloy AB_x , after hydrogenation an AB_xH_y compound is formed, unless any more stable hydride such as AH_z is formed. The term “destabilization” is used in the case a metal hydride AH_2 is mixed with a specie B that can form an alloy with the specie A during dehydrogenation of AH_2 [2.10].

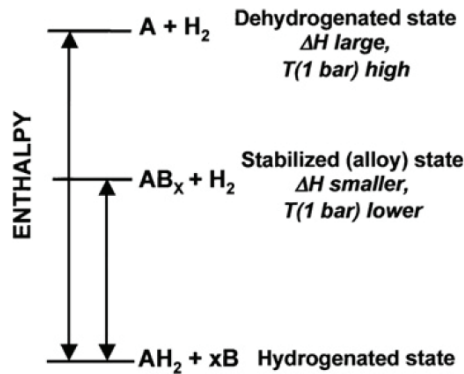
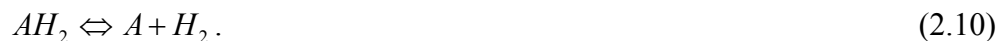


Figure 2.5 Generalized enthalpy diagram illustrating destabilization through alloy formation upon dehydrogenation [2.10].

As shown in the diagram in figure 2.5, in the case the enthalpy of formation of the alloy AB_x is less than that of A, the system will cycle according to the process:



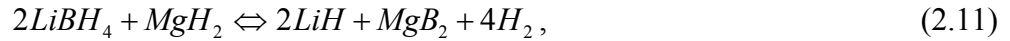
instead of:



Reaction (2.9) implies then a smaller enthalpy of formation of the hydride with respect to reaction (2.10), leading to an higher plateau pressure at the same temperature. This means

that, from thermodynamic and practical point of view, the destabilised system will work at a lower temperature to provide the hydrogen pressure required, for instance, by a fuel cell.

The principle has been exploited for several systems, starting from the pioneering work of Reilly for the Mg-Cu system [2.11], or in the cases of the Mg-Al [2.12], Mg-Si and Li-Si systems [2.13]. More recently, the chemical destabilization has been applied also to complex hydrides as LiBH₄ destabilised with MgH₂ [2.10] according the following desorption reaction:



where the formation of MgB₂ leads to reduced enthalpy of decomposition of LiBH₄ and MgH₂.

2.3.4 Nanoscale metal hydrides

In order to improve the thermodynamics, kinetics and reversibility, specially of light metal hydrides and complex hydrides, it has been proposed to confine or disperse them in nanoporous scaffolds or on high surface area materials, exploiting the favourable properties of nanostructured materials and avoiding sintering and agglomeration during cycling [2.10]. Several recent papers [2.14-2.17] have shown that specially the kinetics and reversibility are improved using this approach, even if no clear evidence of thermodynamic improvement has been reported so far. Anyway, favourable thermodynamic effect with respect to coarse grained materials have been reported in the case of a Pd-H system with a large interface-to-volume ratio [2.18, 2.19].

In the following the mathematical approach by Fichtner [2.20] to the thermodynamic problem will be reported. In the case of reaction of a metal with hydrogen as in reaction (2.10), taking into account the excess surface energy becomes very important for nanosized system, it is possible to calculate the molar free energy of formation of the hydride:

$$\Delta G(r) = \Delta G_0(r) + RT \ln \left(\frac{a_{AH_2}}{a_A p_{H_2}} \right) + \frac{3V_A E_{A \rightarrow AH_2}(\gamma, r)}{r}, \quad (2.12)$$

where r is the radius of the particle, V_A its the molar volume, a the chemical activity and γ the interfacial free energy. The most important term in the equation is $E_{A \rightarrow AH_2}(\gamma, r)$ that represents a surface energy term and is defined as:

$$E_{A \rightarrow AH_2}(\gamma, r) = \left[\gamma_{AH_2}(r) \left(\frac{V_{AH_2}}{V_A} \right)^{2/3} - \gamma_A(r) \right] + E_{ads}. \quad (2.13)$$

E_{ads} takes into account that the surface energy of the hydride and of the metal is reduced by hydrogen absorption on their surface. The enthalpy of hydride formation changes like in the case of equation (2.12):

$$\Delta H' = \Delta H_0 + \frac{3V_A E_{A \rightarrow AH_2}(\gamma, r)}{r}. \quad (2.14)$$

In this case also the $E_{A \rightarrow AH_2}(\gamma, r)$ term can influence the heat of formation, leading to the shift of hydrogen equilibrium according to the van't Hoff equation (2.7).

However this approach is probably not sufficient to explain more complex systems as in the case of a/d of nanoscale complex hydrides. For instance, a complex hydride like NaAlH_4 desorbs H_2 producing solid NaH and Al , two components unlike the case of the decomposition of a binary or ternary metal hydride when only one solid decomposition product is present. The two phases have to react together and with hydrogen to get back the initial complex hydride, that makes the reversibility of complex hydrides a bigger problem with respect to interstitial metal hydrides. Different is the case of LiBH_4 that melts before its decomposition and then the solid decomposition products (LiH and B) have to nucleate from a liquid. Even if nano-confinement will not be sufficient with complex hydrides to improve the thermodynamic properties, it has been shown that it's very useful to improve the kinetics, due to reduced diffusion distances, and reversibility, due to confinement of decomposition products in short distances. The interaction of the surface of the nano-support could also have a great influence on the kinetics of the systems, due to the high surface to volume ratio that could give rise to heterogeneous nucleation processes that, as a consequence, could lead to reduced reaction temperatures.

2.3 Kinetics

The possibility of practical use of a metal hydride is not only related to its thermodynamics and the maximum capacity of hydrogen, but of course also to its kinetics: the total process of a/d must occur in a reasonably short time. In a solid-gas system, as a metal hydride for hydrogen storage applications, it is not only the working temperature determining the rate of the overall process. In fact, crucial factors are the surface contamination by oxygen or water, the defectivity of both surface and bulk, the particle size and the presence of catalysts.

As already discussed in a previous section the hydrogen a/d mechanism in a metal/metal hydride system is made up of five intermediate processes:

1. physisorption of hydrogen molecules on the metal surface;
2. molecule dissociation and chemisorption of hydrogen atoms;
3. penetration of atomic hydrogen through the surface;
4. diffusion of hydrogen through the previously formed hydride layer;
5. nucleation and growth of the hydride at the α phase/ β phase interface.

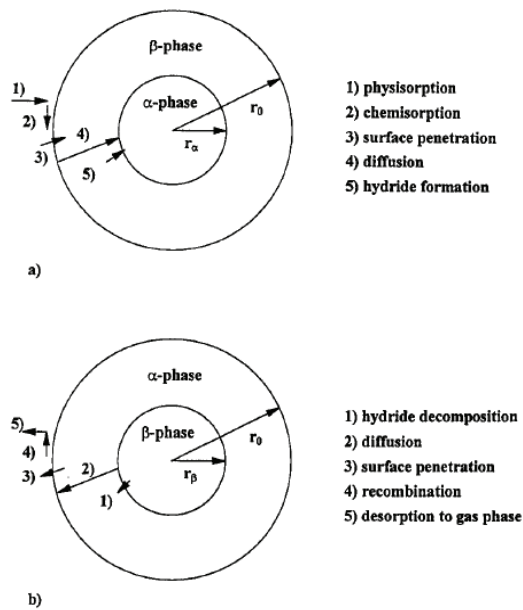


Figure 2.6 Intermediate steps of hydrogen absorption (a) and desorption (b) by a spherical metal/metal hydride particle [2.21].

Generally, it is possible to assume that only one of these is the rate limiting step (the slowest) of the overall reaction. Concerning the desorption process, the stages are the same, but occur in the opposite direction to give molecular hydrogen from the starting hydride phase. Anyway, not necessarily the rate limiting step is the same in both cases. Among the parameters that can be controlled externally, the rate of each stage is of course determined not only by temperature but also by the difference between the actual pressure and the equilibrium plateau pressure. In order to understand which is the limiting process of the reaction, mathematical models can be compared with the experimental data, even if it is difficult to obtain experimental kinetic data that meet the ideal conditions typical of models. For example, it is difficult to remain in isothermal conditions during the measurement due to exothermic/endothermic nature of reactions, to keep a constant pressure (especially while using volumetric devices for the measurements), or to control the surface contamination of samples. The kinetic models should be used carefully, because the behaviour of the kinetic curves is often very similar for the different models, that could lead to contradictory interpretation about the reaction mechanism [2.22]. It is very important to understand which is the slow step of the process in order to understand and improve the kinetic properties of a material.

2.3.1 Solid state kinetic models

The reaction rate of a solid state reaction can be written as:

$$\frac{d\alpha}{dt} = Ae^{\frac{-E}{RT}} f(\alpha), \quad (2.15)$$

where α is the reacted fraction, A the preexponential Arrhenius factor, E the activation energy of the process and $f(\alpha)$ are the algebraic expressions, reported in table 2.1, representing ideal solid state kinetic models, assuming a simple and homogeneous geometry of the system. The reported D_n models are mathematically obtained with the assumption that the rate limiting step is due to diffusion of a chemical specie through the solid, n gives the number of dimensions along which the diffusion occurs. The case D_4 is that of three-dimensional diffusion through a thickening layer [2.23]. In the case of the R_n models the rate limiting step is due to the advancement of the product layer, giving rise to cylindrical-shaped products in the case of R_2 and to the so called “shrinking core morphology” in the case of R_3 mechanism [2.24]. The A_m model has been developed since 1939 by Johnson, Mehl and Avrami [2.25-2.28] and refers to a nucleation and growth kinetic mechanism. In many real systems deviations from these models are expected due to heterogeneity of the samples [2.29].

The experiments can be performed in several heating conditions, mostly isothermal and linear heating experiments are performed. In the case of isothermal experiments, equation (2.15) can be integrated as follows:

$$\int_0^\alpha \frac{d\alpha}{f(\alpha)} = k \int_0^t dt, \quad (2.16)$$

where $k = Ae^{\frac{-E}{RT}}$ is constant. Equation (2.16) can be written more simply as:

$$g(\alpha) = kt. \quad (2.17)$$

Table 2.1 Algebraic expressions for the $f(\alpha)$ and $g(\alpha)$ functions for the most common mechanisms in solid-state reactions [2.30].

mechanism	symbol	$f(\alpha)$	$g(\alpha)$
phase boundary controlled reaction (contracting area, i.e., bidimensional shape)	R2	$(1 - \alpha)^{1/2}$	$2[1 - (1 - \alpha)^{1/2}]$
phase boundary controlled reaction (contracting volume, i.e., tridimensional shape)	R3	$(1 - \alpha)^{2/3}$	$3[1 - (1 - \alpha)^{1/3}]$
unimolecular decay law (instantaneous nucleation and unidimensional growth)	F1	$(1 - \alpha)$	$-\ln(1 - \alpha)$
random nucleation and growth of nuclei (Johnson–Mehl–Avrami equation) ^a	A_m	$m(1 - \alpha)[- \ln(1 - \alpha)]^{1-m}$	$[- \ln(1 - \alpha)]^{1/m}$
two-dimensional diffusion (bidimensional particle shape)	D2	$1/[- \ln(1 - \alpha)]$	$(1 - \alpha) \ln(1 - \alpha) + \alpha$
three-dimensional diffusion (tridimensional particle shape) (Jander equation)	D3	$\frac{3(1 - \alpha)^{2/3}}{2[(1 - \alpha)^{1/3}]}$	$[1 - (1 - \alpha)^{1/3}]^2$
three-dimensional diffusion (tridimensional particle shape) (Ginstein–Bronshtein equation)	D4	$\frac{3}{2[(1 - \alpha)^{-1/3} - 1]}$	$(1 - 2\alpha/3) - (1 - \alpha)^{2/3}$

^a This formal kinetic law generally applies for random nucleation and growth of nuclei, although they are two different processes with different kinetic parameters. The nuclei are generally formed during the induction period. Thus, the $\alpha-t$ (or T) plots usually represent the growth process from preexisting nuclei.

Plotting the right $g(\alpha)$ against time should lead to a straight line whose slope is k . The algebraic expressions for the $g(\alpha)$ are also reported in table 2.1. In the case of non-isothermal experiments it is convenient to write equation (2.15) in its logarithmic form:

$$\ln\left(\frac{d\alpha/dt}{f(\alpha)}\right) = \ln A - E/RT. \quad (2.18)$$

If a correct $f(\alpha)$ has been considered, the plot of the left-hand side of equation (2.18) versus the inverse of temperature should lead to a straight line whose slope is the activation energy E , and intercept the logarithm of the preexponential factor [2.29].

2.4 Hydrogen storage compounds

2.4.1 Binary and intermetallic hydrides

The bond between hydrogen and a metal can be of three types: ionic, covalent and metallic. Among these three types the metallic bond has properties suitable for hydrogen storage. Several simple metals can react with hydrogen leading to hydrides: rare earths like Ce, Pr, Nd, La; transition metals like Mn, V, Fe, Pd; alkali and alkaline earth metals like Li and Mg (actually in this case the bond is ionic or covalent, respectively). However, among the mentioned metals only V and Mg fulfil the requirements of working temperature, pressure, and weight percentage of stored hydrogen interesting for applications. In particular, magnesium and magnesium-based alloys attracted a great interest especially for their high theoretical hydrogen capacity (7.6 wt% for pure Mg) and low cost. This class of materials will be discussed extensively in the next section.

Hydrogen reacts at high temperature with most of transition metals and their alloys to form hydrides. Electropositive elements such as yttrium, scandium, the lanthanides, actinides and elements belonging to the group of titanium and vanadium are the most reactive. The crystal structure of the formed hydride phase remains unchanged with respect to that of the host metal, where hydrogen is contained in octahedral, tetrahedral interstitial sites or a combination of both. This is the reason why these compounds are called “interstitial metal hydrides”. Only a small number of transition metals has no stable hydrides. However, there is a considerable gap in the periodic table that ranges from Group 6 (chromium) to Group 11 (copper), in which the only hydrides are those of palladium ($\text{PdH}_{0.7}$), the unstable nickel metal hydride ($\text{NiH}_{<1}$), the hydrides of chromium (CrH , CrH_2) and copper (CuH). But, as already discussed, the binary hydrides are generally not suitable for practical applications.

From this point of view, more interesting are the hydrides of intermetallic compounds. In the simple case of ternary systems of the type AB_xH_n , in which varying the elemental composition it is possible to “tailor” the hydrogen absorbing properties of the material. The

element labelled as A is typically a rare earth or alkaline earth metal, which tends to form a stable hydride, while the element B is a transition metal, which only forms unstable hydrides (Co, Ni, Cr, Fe, Mn or Al). It has been found that in several intermetallic compounds for which the ratio of the molar amount of component B and component A takes the values $x=0.5, 1, 2.5$, the H/M ratio is higher than 2 [2.31].

An important feature of these compounds is that the operating pressure and temperature can be adjusted varying both the element A and B: the plateau pressure at a given temperature can be varied in this way even by two orders of magnitude. Basically, the larger the cell parameters of the host alloy (and as a consequence the volume of the interstitial sites), the lower is the plateau pressure. In many cases it can be very advantageous to vary the x ratio in order to change the characteristics of the PCI curves. Unfortunately, in most cases, both types of variation result in a reduced hydrogen capacity with respect to the stoichiometric intermetallic AB_x .

Concerning the AB_5 -type intermetallic compounds for the storage of hydrogen, $LaNi_5$ has been the most studied. It gives rise to a whole family of compounds by replacing the A and B element. Lanthanum is usually replaced by the so-called "Mischmetal", a low cost mixture of rare earths that can be easily found in nature, while nickel can be partially replaced by elements such as Mn, Cr, Fe, Al, Co, Cu, Sn, Ge, Si. These substitutions can greatly alter the thermodynamic properties of the system. This family of compounds absorbing around 1.5 wt% hydrogen is easily activated, the operating temperature and pressure are always very close to ambient and the PCI curves show small hysteresis and flat plateaus. The drawbacks of these systems are the low gravimetric hydrogen capacity and the degradation after relatively few a/d cycles [2.32].

Table 2.2 Main classes of intermetallic compounds that form hydrides.

Intermetallic compound family	Prototype	Hydride	Structure	Capacity (wt%)
AB_5	$LaNi_5$	$LaNiH_6$	hexagonal	da 1.0 a 1.9
AB_2	$ZrV_2, ZrMn_2, TiMn_2$	$ZrV_2H_{5.5}$	hexagonal or cubic	da 0.2 a 2.8
AB	TiFe, ZrNi	TiFeH ₂	cubic	da 1.0 a 1.9
A_2B	Mg_2Ni, Ti_2Ni	Mg_2NiH_4	cubic	da 0.3 a 3.5

Even the AB_2 type alloys (also known as "Laves phases") aroused considerable interest as materials for hydrogen storage. There are three types of crystalline structures: cubic C15 ($MgZn_2, ZrV_2, TiCr_2$ low temperature phase, $ZrCr_2$ high temperature phase), hexagonal C14 ($MgCu_2, ZrCr_2$ low temperature phase, $TiCr_2$ high temperature phase, $ZrMn_2$), hexagonal C36 ($MgNi_2$). The ability of storing hydrogen is relatively high when the substituent of the A element is Zr or Ti; when it is a rare earth, the compound tends to disproportionation and

amorphization, making it less attractive for applications. The element B is typically a 3d element as V, Cr, Mn, Fe or combination of them. In general, the AB₂ compounds are appreciated for good reaction kinetics, longer life and lower cost compared to the systems of the type LaNi₅. The AB₂ type intermetallic compounds show in several cases a greater capacity than those of AB₅ type, but are more sensitive to gaseous impurities. Small amounts of oxygen can cause a permanent loss of capacity for an AB₂ compound, while for an AB₅ the loss is only partial. One of the advantages, especially for the AB₅ and AB₂ types, is the metal segregation at the surface: this leaves a greater abundance of the element B on the surface that usually favours the adsorption and dissociation of hydrogen molecules [2.33].

The AB family is mentioned mainly for historical reasons. ZrNi was the first intermetallic compound discovered to be able to absorb hydrogen, while TiFe represents the first application of an intermetallic compound in a hydrogen powered car. The last compound has a capacity of around 1.9 wt% H₂ and its constituents are very cheap. However, the process of activation of this material is problematic for the easy formation of a titanium oxide layer and, moreover, high temperatures and pressures are also required to achieve a reversible maximum capacity of hydrogen. These difficulties have contributed to the abandonment of such materials [2.32].

A₂B type alloys have C16 cubic structure. The material with the best performance among the alloys of this family is Mg₂Ni, able to absorb about 3.6 wt% hydrogen. The operating temperatures allowing plateau pressures higher than 1 atm are above 250 °C, but the presence of Ni, which plays a catalytic activity for the adsorption and dissociation of hydrogen, allows favourable absorption/desorption kinetics [2.33]. This material will be discussed in more detail in the next section.

2.4.2 Mg and Mg-based hydrides

Magnesium is an alkaline earth metal with atomic number 12, is the eighth most abundant element on earth's crust and constitutes about 2% of it. Due to its abundance, its cost is very low. It is a silver-white metal whose dust is very reactive and highly flammable in air. The density of 1.74 g/cm³, makes it one of the lightest elements in solid state. Its crystal structure is hcp, while the β-MgH₂ hydride that forms reacting with hydrogen has the tetragonal structure of rutile. In specific conditions it can also form a γ-MgH₂ phase, metastable at ambient temperature and pressure, having orthorhombic structure. β-MgH₂ is a stable compound, its ΔH of formation is -74.5 kJ/mol [2.34], meaning that the hydride decomposition and the subsequent hydrogen release from the system can only occur at temperatures above 300 °C with an equilibrium pressure of interest for practical applications (a few tenths higher than the atmospheric pressure). This is a major drawback for a material that is candidate for the use in hydrogen tanks for vehicular applications. In fact, part of the energy produced by an internal combustion engine or a fuel cell should be used to heat up the

reservoir to the working temperature. As said, the theoretical hydrogen capacity of magnesium is 2 hydrogen atoms per metal atom that, taking into account the low density of this element, means a capacity of 7.6 wt% H₂.

A further important concern of pure magnesium is its very slow kinetics both during hydrogen desorption and absorption. The slow reaction kinetics of magnesium with hydrogen can be partially justified by the fact that the "sticking coefficient" of hydrogen on the Mg surface is low ($\sim 10^{-6}$), that means only a very small portion of hydrogen molecules impinging to the surface remain stucked after the impact [2.35]. It should be also mentioned that the activation barrier for the dissociation of hydrogen depends strongly on the geometry of the adsorption site and, in the case of magnesium, this barrier is too high to allow a fast kinetic. Moreover, the growth of a MgH₂ thick layer during the absorption process is the cause of a more and more difficult diffusion of atomic hydrogen to the nucleus of magnesium due to its low diffusivity through the hydride phase. When the hydride thickness reaches 30-50 μm , the reaction stops almost completely. These problems can be partially solved (more efficiently if compared to the problem of hydride stability), reducing by high energy ball milling the crystalline domains size of the phases and/or adding suitable catalysts.

The high energy ball milling, developed around 1966, is a non-equilibrium technique used to produce powders with special features. Used initially for the dispersion of oxides in high strength iron and nickel alloys for the aerospace industry, it is still an established industrial technology for the production of ferromagnetic amorphous sheets used in electrical transformers obtained by sintering the powders. More recently, high energy ball milling has been used in order to obtain nanocrystalline powders of Mg and Mg-based systems for hydrogen storage applications, used particularly to improve the kinetic properties. It is easily possible to obtain nanocrystalline materials characterized by grain sizes less than 100 nm. The reduced grain size leads to a faster diffusion of hydrogen through the hydride layer, whose thickness in this case is limited to the grain size. Besides this, the milling process leads to a substantial increase of specific surface area resulting in much more reactive new and clean surfaces. An example of the effect of high energy ball milling on the kinetic properties of Mg is shown in Figure 2.7.

The use of catalysts in the Mg-based materials is also crucial to achieve acceptable kinetic properties. The use of one or more catalysts is often associated to high energy ball milling, which not only allows the reduction of grain size to nanoscale, but also allows the uniform dispersion of the catalyst in within the material. The main classes of catalysts used in these systems are some simple transition metals (Ni, Co, Ti, Fe) and transition metal oxides. Moreover, several studies have shown that combining magnesium with intermetallic compounds as LaNi₅, FeTi or ZrFe_{1.4}Cr_{0.6}, it is possible to significantly improve the absorption/desorption kinetics at temperatures above 300 °C [2.36].

The catalytic activity of these metals or alloys occurs in one of the stages of the a/d process, which likely is the dissociation of the hydrogen molecule at the metal surface. The binding

energy of atoms in the hydrogen molecule is 4.7 eV, comparable to the binding energy of metals, even if the bond length is much smaller compared to the lattice parameters of metals. Thus, the dissociative chemisorption needs much work to increase the bond distance and break it: it is then necessary that the single hydrogen atom shares its electron with the substrate in order to achieve a new electronic configuration. If the substrate consists of a simple or noble metal, the antibonding level $1\sigma_u$ of the hydrogen molecule mixes with the electronic levels of the metal (M) that have the same symmetry, forming the bonding and antibonding levels H-M. When the bonding level wins the competition, then the chemisorption takes place. The approach of the hydrogen molecule to the surface and subsequent dissociation, however, are hindered by the Pauli repulsion due to overlapping of the $1\sigma_g$ orbital of hydrogen with the filled s bands of the substrate. The presence of such a repulsion results in the activation barrier of dissociative process [2.37].

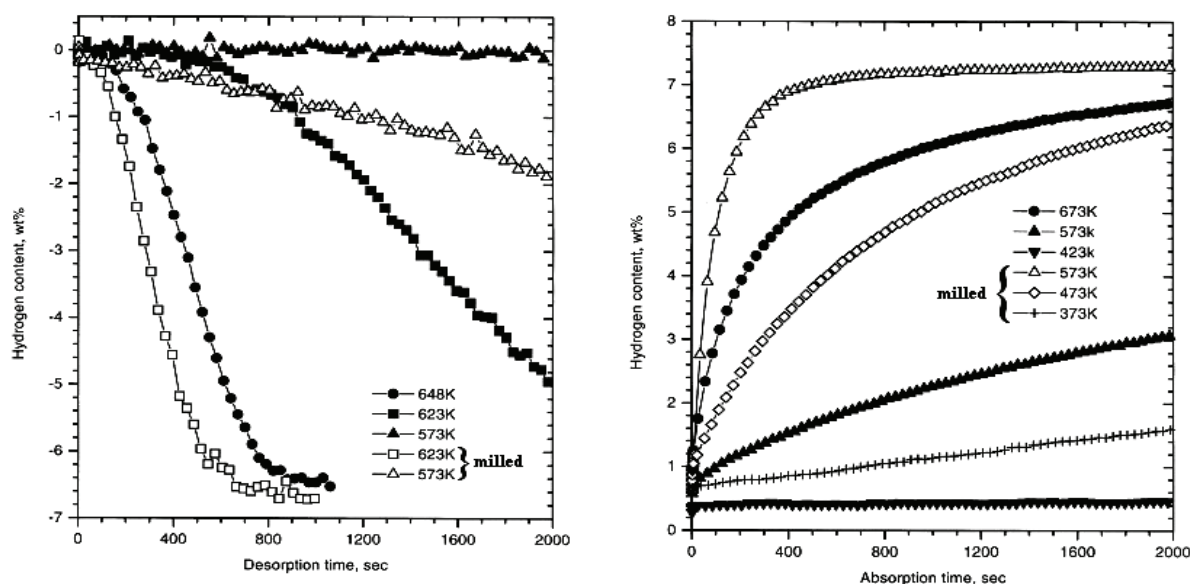


Figure 2.7 Comparison of absorption/desorption kinetics at different temperatures in the case of a simple MgH_2 sample and one processed by high energy ball milling (milled) [2.38].

In the case of a transition metal, there is an effect that sums to those mentioned, due to the presence of d -type orbitals incompletely filled. When the hydrogen molecule approaches the surface, the electrons of the s band of the substrate can be transferred to the d band. Now, since the orbital d is much more localized than s , it slightly overlaps with the binding orbital $1\sigma_g$ of the hydrogen molecule, weakening the Pauli repulsion. The reduction of this repulsion practically cancels the activation barrier of dissociative process, and the system does not pass through the physisorption of the hydrogen molecule, but is absorbed directly as dissociated [2.37]. This mechanism shows that many transition metals absorb hydrogen dissociatively, while simple and noble metals do not.

In addition to some transition metals, their oxides also appear to be excellent catalysts for magnesium processed with the technique of high energy ball milling. Transition metal oxides such as Nb_2O_5 , V_2O_5 , TiO_2 , Al_2O_3 , Sc_2O_3 , Cr_2O_3 , CuO , Fe_3O_4 , Mn_2O_3 , may also show catalytic properties superior to those of constituting transition metals. The mechanisms by which these oxides carry out their catalytic activity is not yet clear, but it is likely related to the ability of the transition elements to have different valence states and therefore different electronic configurations [2.36].

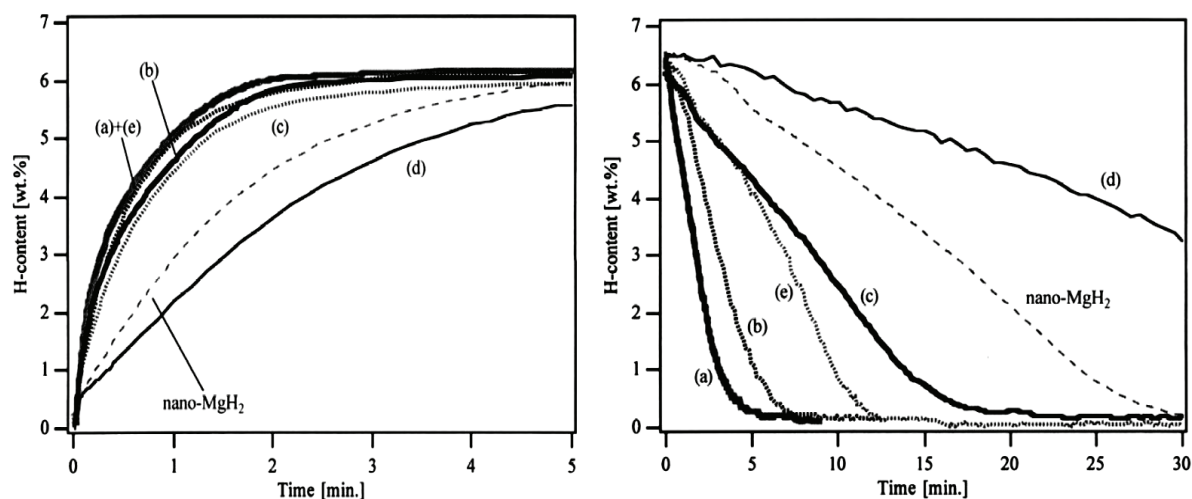


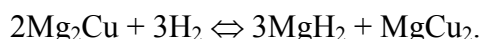
Figure 2.8 Absorption/desorption curves of $\text{MgH}_2/(\text{Me}_x\text{O}_y)_{0.01}$ samples at 300°C . (a) $\text{MgH}_2/(\text{V}_2\text{O}_5)_{0.01}$; (b) $\text{MgH}_2/(\text{TiO}_2)_{0.01}$; (c) $\text{MgH}_2/(\text{Al}_2\text{O}_3)_{0.01}$; (d) $\text{MgH}_2/(\text{SiO}_2)_{0.01}$; (e) $\text{MgH}_2/(\text{Sc}_2\text{O}_3)_{0.01}$ [2.35].

The local electronic structure is very important for catalysis. Several studies have shown that perfect TiO_2 or other oxides surfaces and single crystals are inert to the H_2 molecule. In the case of a magnesium alloy catalyzed with titanium or vanadium, for example, considering the great affinity of these two metals with oxygen, the possible formation of oxides of titanium or vanadium leads to total loss of catalytic transition metal. For these reasons, it is believed that the catalytic effect is given by the large number of lattice defects induced by high energy milling on the surface of the oxides [2.35].

The major problem in the use of magnesium-based materials is still the high thermodynamic stability of the hydride phase. Many studies, conducted in recent years have shown that the magnesium hydride plateau pressure is not changed by surface treatment, adding catalysts, unless alloys such as Mg_2Ni , Mg_2Cu , Mg_2Al_3 , Mg_2Co , Mg_2Fe , ReMg_{12} ($\text{Re}=\text{Ce}$, La) and $\text{La}_2\text{Mg}_{17}$ are formed. These intermetallic compounds can be divided into three categories according to their behaviour:

1. Compounds that form ternary hydrides such as: $\text{Mg}_2\text{Ni} + 2\text{H}_2 \leftrightarrow \text{Mg}_2\text{NiH}_4$;
2. Compounds that show a reaction of disproportionation, forming two hydrides such as: $2\text{CeMg}_{12} + 27\text{H}_2 \leftrightarrow 2\text{CeH}_3 + 24 \text{MgH}_2$;

3. Compounds that give, after disproportionation, only magnesium hydride as:



Many other compounds can be obtained by partial substitution of magnesium with metals like V, Cr, Mn, Fe, Ni, Cu, Zn in its alloys with rare earths, or partially replacing nickel with Be, Co, Fe, Mn in Mg₂Ni-like compounds.

As can be seen from table 2.3, the only magnesium alloy showing a substantial change in the enthalpy of hydride formation, and therefore being less stable than MgH₂, is Mg₂Ni. Compared to the others, although showing a lower capacity of hydrogen, it is characterized by faster kinetics, both in absorption and desorption. The synthesis of other Mg alloys presents, moreover, some more difficulties. For these reasons Mg₂Ni is the most studied magnesium alloy for hydrogen storage.

Table 2.3 Magnesium alloys forming hydrides.

Intermetallic compound	Hydride	Capacity (wt%)	Formation enthalpy (kJ/mol)
Mg ₂ Ni	Mg ₂ NiH ₄	3.6	-64.5
Mg ₂ Cu	MgH ₂ +MgCu ₂	2.6	-77.1
Mg ₂ Fe	Mg ₂ FeH ₆	5.4	-77.4
Mg ₂ Co	Mg ₂ CoH ₅	4.5	-86.0

Reacting with hydrogen, it forms the ternary hydride Mg₂NiH₄, whose ability to reversibly store hydrogen was discovered in 1968 by Reilly and Wiswall [2.39]. Mg₂NiH₄ has been studied in recent years not only as a promising metal hydride for hydrogen storage, but also to improve the capacity of the electrodes in nickel-metal hydride (NiMH) batteries [2.40]. As already discussed, the maximum hydrogen content of this hydride is 3.6 wt% and enthalpy of formation of the hydride is -64.5 kJ/mol. Theoretically, Mg₂Ni shows a single very flat plateau between 0.1 and 1.33 H/M in the case it is pure, as shown in Figure 2.9a. However, in most cases it is difficult to avoid the presence of unalloyed magnesium in the sample. This because Mg₂Ni is synthesised by induction melting in an inert atmosphere starting from equal parts by weight of nickel and magnesium.

Because of the presence of an eutectic point in the phase diagram of the Mg-Ni system between Mg and Mg₂Ni, it is almost inevitable the presence of pure magnesium. In this case, as can be seen in Figure 2.9b, there is a second plateau at lower pressures due to the presence of MgH₂. Of course, the length of the first plateau is proportional to the amount of pure magnesium initially present in the system. In addition to the Mg₂NiH₄ compound it is also possible to find in this system another stable phase: Mg₂NiH_{0.3}. It is also possible to find supersaturated metastable phases: Mg₂NiH, Mg₂NiH_{1.2} and Mg₂NiH_{1.8} [2.39].

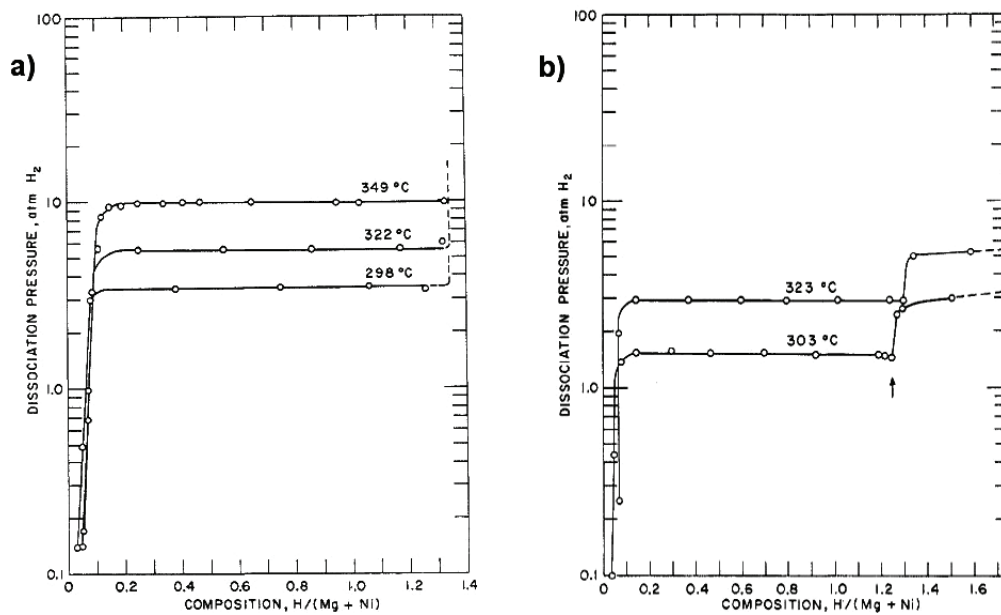


Figure 2.9 PCI curves of a pure Mg₂Ni sample (a) and one with traces of Mg (b). The arrow shows the point where the second plateau starts [2.39].

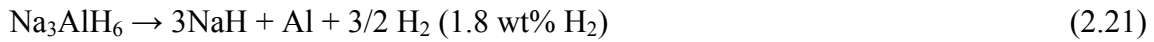
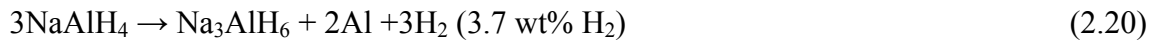
2.4.3 Complex metal hydrides

Alkaline and alkaline earth metals salts of [AlH₄]⁻, [NH₂]⁻ and [BH₄]⁻ anions, alanates, amides and borohydrides, respectively, have been extensively studied in recent years as promising systems for solid state hydrogen storage. These materials are commonly called “complex” hydrides, even if only alanates contain metal complex anions. For “amides” we will intend a mixture of an alkali metal or alkaline earth metal amide and a binary hydride. In this class of materials hydrogen is covalently bonded to the central element of the anion, unlike classical hydrides where hydrogen occupies interstitial sites. The reason why complex hydrides are considered very promising for this application is the high gravimetric hydrogen content even if many efforts are being addressed by the research in order to overcome the problem of the high kinetic barriers to both dehydrogenation and rehydrogenation of these materials in solid state.

The first family of complex hydrides studied for hydrogen storage purposes have been alanates, since Bogdanovich and Schwickardi discovered that doping NaAlH₄ with selected Ti-based catalysts it was possible to considerably improve the hydrogen a/d kinetics [2.41]. Group I alanates desorb hydrogen in the 200-300 °C temperature range (201 °C, 265 °C and 290 °C for Li, Na and K, respectively) [2.42] according to the total reaction:



The further decomposition of the binary metal hydride occurs only at temperatures too high for applications (>400 °C). Ashby and Kobez discovered that the total reaction 2.19 occurs in two steps in the case of NaAlH₄ [2.43]:



This two step reaction has been also confirmed by PCI measurements [2.41]. The same behaviour has been found through DSC measurements in the case of LiAlH₄ by Block and Gray [2.43]. They found that the first step (analogous to reaction (2.20)) occurs in the temperature range 187-218 °C, releasing 5.3 wt% H₂ with a $\Delta H = -10$ kJ/mol H₂. The latter value means that this step is exothermic and then that the reverse reaction, since the entropy change must be negative, is nonspontaneous in all the conditions. The second step (analogous to reaction (2.21)) occurs in the range 228-282 °C, releasing 2.6 wt% H₂ with $\Delta H = 25$ kJ/mol H₂. Concerning KAlH₄, the first step leading to the hexahydride occurs at 300 °C, a much higher temperature compared to NaAlH₄. Unlike the alkali metal alanates, Fichtner et al. [2.44] found that Mg(AlH₄)₂ decomposes at 163 °C without the formation of an hexahydride:



MgH₂ then decomposes at 287 °C producing metallic Mg leading to a total release of 9.3 wt% H₂. Unfortunately, since the first step of the decomposition reaction is exothermic, the rehydrogenation of decomposition products to magnesium alanate is thermodynamically not allowed. It seems then that only NaAlH₄ is a good candidate as a material of this class for solid state hydrogen storage. As already reported, Bogdanovich and Schwickardi found that evaporation of a suspension of NaAlH₄ in a solution of Ti(OBu)ⁿ (titanium tetra-*n*-butoxide) and β -TiCl₃ in diethyl ether (a few mol% with respect to NaAlH₄) gives a material with dramatically enhanced kinetic properties compared to the undoped material [2.41].

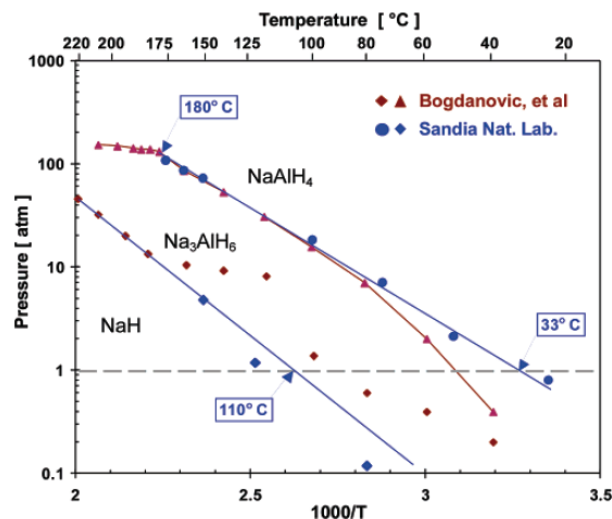
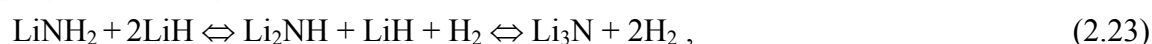


Figure 2.10 Van't Hoff plot of the equilibria: $\text{NaAlH}_4 \leftrightarrow 1/3(\alpha\text{-Na}_3\text{AlH}_6) + 2/3\text{Al} + \text{H}_2$ and $\alpha\text{-Na}_3\text{AlH}_6 \leftrightarrow 3\text{NaH} + \text{Al} + 3/2\text{H}_2$ [2.46].

It has also been found that further cyclability and kinetic improvement can be achieved by mechanical mixing of the alanate and the Ti-based catalysts [2.45]. This discovery allowed then to remove the high kinetic barrier preventing NaAlH₄ to be a reversible system for hydrogen storage and moreover aimed more research on other complex hydrides. Despite the very encouraging results from the kinetic point of view, as shown in figure 2.10, only the equilibrium $\text{NaAlH}_4 \Leftrightarrow 1/3(\alpha\text{-Na}_3\text{AlH}_6) + 2/3\text{Al} + \text{H}_2$ reaction allows a H₂ equilibrium pressure viable for onboard applications ($\Delta H=37$ kJ/mol H₂), while for the second equilibrium equation $\alpha\text{-Na}_3\text{AlH}_6 \Leftrightarrow 3\text{NaH} + \text{Al} + 3/2\text{H}_2$ 110 °C are required for a pressure of 1 atm. Hence, if the only heat produced by the fuel cell can be used to achieve the hydride working temperature, only the first equilibrium can be exploited, limiting the total H₂ capacity of this system to 3.6 wt%.

It has been recently found that selected mixtures of amides plus binary hydrides can show favourable thermodynamic properties for the hydrogen a/d processes. Chen et al. [2.47] observed that ball milled mixtures of LiNH₂ and LiH begin to desorb hydrogen at temperatures as low as 150 °C and the complete hydrogen desorption ends to about 400°C. The proposed decomposition reactions are:



whose mechanism is based on the ultrafast reaction between NH₃ and LiH [2.48]. According this mechanism, LiNH₂ decomposes producing Li₂NH and NH₃ which reacts very fast with LiH to give again some LiNH₂ and resulting in H₂ desorption.

Other authors [2.49, 2.50] explained the process according to an acid-base mechanism assuming that the hydrogen molecule is formed by the close contact of positive H^{δ+} and negative H^{δ-} hydrogen ions carried by the amide and the hydride, respectively. A hydrogen amount of 6.5 wt% is released during the first step, while a total theoretical reversible hydrogen amount of 10.4 wt% could be obtained from both reactions. Despite the high content of hydrogen released during the first step of reaction (2.23) and the relatively low desorption temperature, the plateau pressure in desorption mode at 280 °C was only 1 atm and it is much lower in the case of the second step. Hence, further destabilisation of the mixed system LiNH₂ + LiH is required in order to use it practically. Orimo et al. [2.51] suggested that in the LiNH₂ crystal the bonding between Li⁺ cation and [NH₂]⁻ anion has ionic character and in consequence partial substitution of Li by Mg (more electronegative element than Li) would decrease the interaction of Li⁺ with [NH₂]⁻ leading to destabilisation. The predicted thermodynamic behaviour was first observed separately by Luo [2.52] and Xiong et al. [2.53]. The correct interpretation of the process was achieved by Yang et al. [2.54] who found that, starting from the ball milled mixture, by means of a heat treatment at high hydrogen pressure the following reaction of activation occurs:



The obtained mixed products can be used to reversibly release and absorb hydrogen, according to the reaction:



The theoretical hydrogen capacity of the material is 5.6 wt%, with an operating temperature around 200°C. The great potentiality of this material lies in the fact that the desorption enthalpy is within the interval from 34 to 41.6 kJ/mol H₂ [2.52-2.56]. This allows to obtain plateau pressures higher than 1 atm at temperatures lower than 100 °C. A limit consists in the kinetic properties; in particular for a complete hydrogen absorption a time of 3-4 hours is required at 220 °C [2.54]. A proposed dehydrogenation mechanism [2.42], schematically shown in figure 2.11, is based on Li⁺ diffusion from LiH to Mg(NH₂)₂ transforming [NH₂]⁻ into [NH]²⁻ and H⁺. The latter is attracted by the H⁻ of LiH leading to H₂ formation and desorption.

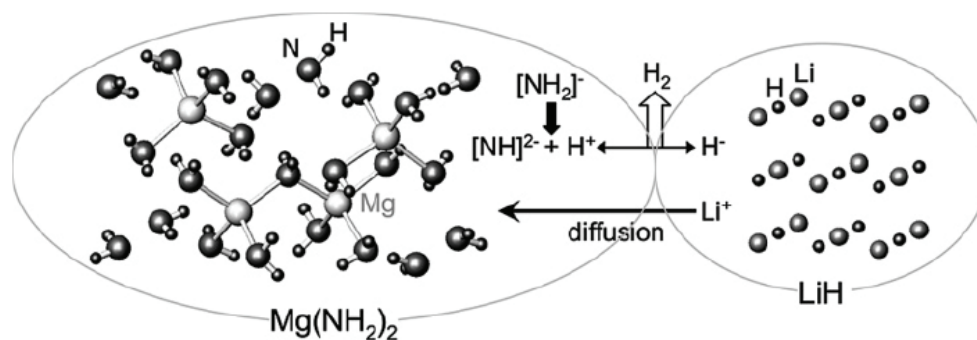
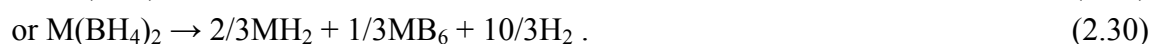


Figure 2.11 Schematic desorption mechanism in the system $\text{Mg}(\text{NH}_2)_2 + \text{LiH}$ [2.42].

Borohydrides or, more correctly, tetrahydroborates are saline compounds where hydrogen is covalently bonded to boron in a tetrahedral anion where B is in the centre and H atoms are located in the four corners. The negative charge of the complex anion is balanced by a metal, a transition metal, an alkali metal or an alkaline earth ion. This class of compounds has been commonly used as reducing agents in both organic and inorganic synthesis. Especially alkali metal and alkaline earth borohydrides have recently attracted a lot of interest in the field of solid state hydrogen storage due to their very high gravimetric hydrogen content. Alkali metal borohydrides decompose according to the following reactions:



Alkaline earth borohydrides decompose according this reaction:



The first and most studied borohydride for hydrogen storage purposes is LiBH₄. The DCS profile of LiBH₄ (see figure 2.12) shows two sharp peaks at relatively low temperature and

one much broader after 330 °C, all endothermic. The first at 107 °C corresponds to a polymorphic transition from the low temperature orthorhombic $Pnma$ structure to the high temperature hexagonal $P6_3mc$ structure, the second at 277 °C corresponds to the melting and the third broad peak to the dehydrogenation [2.57]. LiBH_4 starts decomposing above 300 °C according the following overall reaction:



releasing 13.4 wt% H_2 . Not all the theoretical hydrogen content can be easily released, due to the high stability of LiH which desorbs hydrogen only above 730 °C [2.58].

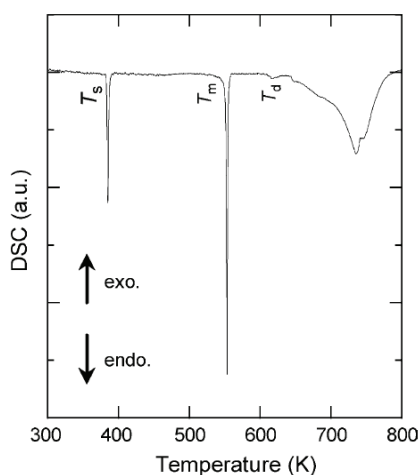


Figure 2.12 DSC profile of LiBH_4 . The sample was heated under 0.1MPa of hydrogen at a rate of 10 K/min. [2.57].

Anyway, the dehydrogenation mechanism involves several intermediate steps: at low heating rates at least three desorption peaks are evident [2.59]. Evidence of the formation of the intermediate phase, a borohydride cluster $\text{Li}_2\text{B}_{12}\text{H}_{12}$, came recently from Raman spectroscopy and XRD [2.60]. In addition to the relatively high decomposition temperature, the problem of using LiBH_4 as a hydrogen storage material is related the complexity of the recycling mechanism: as reported by Orimo et al. [2.57], reaction (2.30) is reversible only in extreme conditions (at 350 bar H_2 and 600 °C). Two absorption mechanisms have been proposed for the reabsorption of hydrogen by LiH and B :

1. LiH and B boron react with each other giving an intermediate phase that subsequently reacts with hydrogen to produce LiBH_4 ;
2. B and H_2 react with each other to produce diborane that is known to readily react with alkali hydrides to produce the corresponding borohydride [2.61].

The problem of the second mechanism is that, being the reaction of hydrogen with B endothermic, the reaction will only proceed at high temperature and pressure [2.42]. It is very important to understand the actual mechanism that leads to the formation of LiBH_4 from the

decomposition products, in order to select the right catalysts that can improve the reaction kinetics.

Other light metal borohydrides are currently being investigated for hydrogen storage applications, among them $\text{Mg}(\text{BH}_4)_2$ [2.62-2.64] that decomposes desorbing a theoretical 14.9 wt% H_2 between 280 °C and 430 °C, and $\text{Ca}(\text{BH}_4)_2$ [2.65-2.68] that decomposes desorbing a theoretical 8.7 wt% H_2 above 330 °C [2.67]. It has been reported that the frequency of the stretching and bending modes of hydrogen atoms in the anion and the melting point of the borohydride are correlated to the electronegativity of the cation [2.69]. Then the thermodynamic properties of the series $\text{M}(\text{BH}_4)_n$ ($\text{M}=\text{Li}, \text{Na}, \text{K}, \text{Mg}, \text{Sc}, \text{Cu}, \text{Zn}, \text{Zr}, \text{Hf}; n=1-4$) have been investigated by first principle calculations [2.70]. As shown in figure 2.13, where the heat of formations of several borohydrides have been related to the Pauling electronegativity of the cation, it has been found that the charge transfer between the metal cation and the complex anion is responsible of the thermodynamic stability of the borohydride.

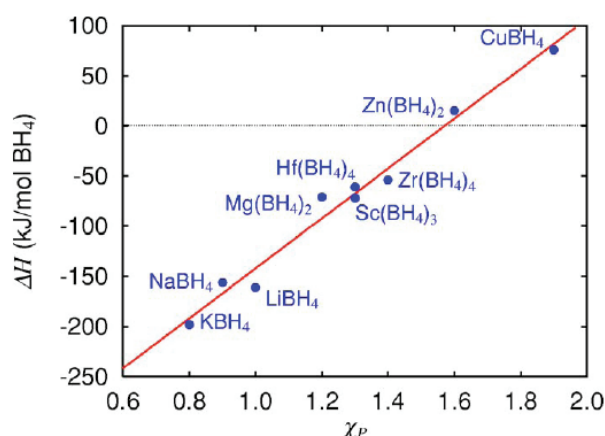


Figure 2.13 Correlation between the heat of formation of metal borohydrides and the Pauling electronegativity of the metal cation [2.70].

As seen, complex hydrides have very attractive features like fast a/d kinetics in the case of alanates, thermodynamics and cyclability in the case of amides, high gravimetric hydrogen capacity in the case of borohydrides. However, many are the problems that could be overcome in order to get a good system for solid state hydrogen storage. In particular, in the case of alanates the reversible capacity is not enough for a practical use, in the case of amides, in addition to low capacity, the potential evolution of ammonia could be a problem, finally in the case of borohydrides reversibility and slow reaction kinetics represent the major limitations.

- [2.1] Shlapbach, L., *Surface properties and activation*, In: Hydrogen in intermetallic compounds II (1992), Springer-Verlag Berlin Heidelberg.
- [2.2] David, E., *An overview of advanced materials for hydrogen storage*. J. Mater. Process. Tech. (2005) 162-163, 169.
- [2.3] Züttel A., Wenger P., Sudan P., Mauron Ph., Orimo S., *Hydrogen density in nanostructured carbon, metals and complex materials*, Mat. Sci. Eng. B (2004) 108, 9.
- [2.4] Atkins P, De Paula J., *Physical Chemistry 7th edition*, Oxford University Press.
- [2.5] Switendick A.C, *Band structure calculations for metal hydride systems*, Z. Phys Chem. (1979) 117, 89.
- [2.6] Westlake D.J., *A geometric model for the stoichiometry and interstitial site occupancy in hydrides (deuterides) of LaNi₅, LaNi₄Al and LaNi₄Mn*, J. Less Comm. Metals (1983), **91**, 275.
- [2.7] Züttel A., *Hydrogen storage methods*, Naturwissenschaften (2004) 91,157.
- [2.8] Griessen R., Driessen A., *Heat of formation and band structure of binary and ternary metal hydrides*, Phys. Rev. B (1984) 30, 4372.
- [2.9] Miedema A. R., *The electronegativity parameter for transition metals: Heat of formation and charge transfer in alloys*, J. Less Comm. Metals (1973), **32**, 117.
- [2.10] Vajo J. J., Olson G. L., *Hydrogen storage in destabilized chemical systems*, Scripta Mater. (2007) **56**, 829.
- [2.11] Reilly J.J., Wiswall R.H., *Reaction of hydrogen with alloys of magnesium and copper*, Inorg. Chem. (1967) **6**, 2220.
- [2.12] Zaluska A., Zaluski L., Ström-Olsen J.O., *Structure, catalysis and atomic reactions on the nano-scale: a systematic approach to metal hydrides for hydrogen storage*, Appl. Phys. A (2001) **72**, 157.
- [2.13] Vajo J. J., Mertens F., Ahn C. C., Bowman R. C., B. Fultz, *Altering Hydrogen Storage Properties by Hydride Destabilization through Alloy Formation: LiH and MgH₂ Destabilized with Si*, J. Phys. Chem. B (2004) **108**, 13977.
- [2.14] De Jongh P. E., Wagemans R. W. P., Eggenhuisen T. M., Dauvillier B. S., Radstake P. B., Meeldijk J. D., Geus J. W., de Jong K. P., *The Preparation of Carbon-Supported Magnesium Nanoparticles using Melt Infiltration*, Chem. Mater. (2007) **19**, 6052.

- [2.15] Gross A. F., Vajo J. J., Van Atta S. L., Olson G. L., *Enhanced Hydrogen Storage Kinetics of LiBH_4 in Nanoporous Carbon Scaffolds*, J. Phys. Chem. C (2008) **112**, 5651.
- [2.16] Fichtner M., Zhao-Karger Z., Hu J., Roth A., Weidler P., *The kinetic properties of $\text{Mg}(\text{BH}_4)_2$ infiltrated in activated carbon*, Nanotechnology (2009) **20**, 204029.
- [2.17] Cahen S., Eymery J. B., Janot R., Tarascon J. M., *Improvement of the LiBH_4 hydrogen desorption by inclusion into mesoporous carbons*, J. Power Sources (2009) **189**, 902.
- [2.18] Eastman J. A., Thompson L. J., Kestel B. J., *Narrowing of the palladium-hydrogen miscibility gap in nanocrystalline palladium*, Phys. Rev. B (1993) **48**, 84.
- [2.19] Weissmueller J., Lemier Ch., *Lattice Constants of Solid Solution Microstructures: The Case of Nanocrystalline Pd-H*, Phys. Rev. Lett. (1999) **82**, 213.
- [2.20] Fichtner M., *Properties of nanoscale metal hydrides*, Nanotechnology (2009) **20**, 204009.
- [2.21] Martin M., Gommel C., Borkhart C., Fromm E., *Absorption and desorption kinetics of hydrogen storage alloys*, J. Alloys Compd. (1995) **238**, 193.
- [2.22] Gerard N., Ono S., *Hydride formation and decomposition kinetics*, In: Hydrogen in intermetallic compounds II (1992), Springer-Verlag Berlin Heidelberg.
- [2.23] Osovizkya A., Blochb J., Mintzb M. H., Jacoba I., *Kinetics of hydride formation in massive LaNi_5 samples*, J. Alloys Compd. (1996) **245**, 168.
- [2.24] Hana J.S., Pezatzb M., Jai-Younga L., *A study of the decomposition of magnesium hydride by thermal analysis*, J. Less Comm. Metals (1987) **130**, 395.
- [2.25] Johnson W.A., Mehl. H.F., Trans. Am. Ceram. Soc. (1939) **51**, 416.
- [2.26] Avrami M., *Kinetics of Phase Change. I General Theory*, J. Chem. Phys. (1939) **7**, 1103.
- [2.27] Avrami. M., *Kinetics of Phase Change. II Transformation-Time Relations for Random Distribution of Nuclei*, J. Chem. Phys. (1940) **8**, 212.
- [2.28] Avrami M., *Granulation, Phase Change, and Microstructure Kinetics of Phase Change. III*, J. Chem. Phys. (1941) **9**, 177.

- [2.29] Pérez-Maqueda L. A., Criado J. M., Sánchez-Jiménez P. E., *Combined Kinetic Analysis of Solid-State Reactions: A Powerful Tool for the Simultaneous Determination of Kinetic Parameters and the Kinetic Model without Previous Assumptions on the Reaction Mechanism*, Phys. Chem. A (2006) **110**, 12456.
- [2.30] Gotor F. J., Criado J. M., Malek J., Koga N., *Kinetic Analysis of Solid-State Reactions: The Universality of Master Plots for Analyzing Isothermal and Nonisothermal Experiments*, J. Phys. Chem. A (2000) **104**, 10777.
- [2.31] Züttel A., *Materials for hydrogen storage*, Materials Today (2003) **6**, 24.
- [2.32] Bououdina M., Grant D., Walker G., *Review on hydrogen absorbing materials-structure, microstructure, and thermodynamic properties*, Int. J. Hydrogen Energ. (2005) **31**, 177.
- [2.33] Dantzer P., *Properties of intermetallic compounds suitable for hydrogen storage applications*, Mat. Sci. Eng. A (2002) **329-331**, 313.
- [2.34] Sandia National Laboratories – Hydride Information Centre, available at: <http://hydpark.ca.sandia.gov/>
- [2.35] Oelerich W., Klassen T., Bormann R., *Metal oxides as catalysts for improved hydrogen sorption in nanocrystalline Mg-based materials*, J. Alloys Compd. (2000) **315**, 237.
- [2.36] Liang G., Shultz R., *The reaction of hydrogen with Mg-Cd alloys prepared by mechanical alloying*, J. Mater. Sci. (2004) **39**, 1557.
- [2.37] Harris J., Andersson S., *H₂ dissociation at metal surfaces*, Phys. Rev. Lett. (1985) **55**, 1583.
- [2.38] Huot J., Liang G., Boily S., Van Neste A., Shultz R., *Structural study and hydrogen sorption kinetics of ball-milled magnesium hydride*, J. Alloys Compd. (1999) **293-295**, 495.
- [2.39] Reilly J.J., Wiswall R.H., *The reaction of hydrogen with alloys of magnesium and nickel and the formation of Mg₂NiH₄*, Inorg. Chem. (1968) **7**, 2254.
- [2.40] Zaluski L., Zaluska A., Ström-Olsen J.O., *Hydrogen absorption in nanocrystalline Mg₂Ni formed by mechanical alloying*, J. Alloys Compd. (1995) **217**, 245.

- [2.41] Orimo S., Nakamori Y., Eliseo J. R., Züttel A., Jensen C. M., *Complex hydrides for hydrogen storage*, Chem. Rev. (2007) **107**, 4111.
- [2.42] Ashby E. C., Kobetz P., *The direct synthesis of Na₃AlH₆*, Inorg. Chem. (1966) **5**, 1615.
- [2.43] Block J., Gray A. P., *The Thermal Decomposition of Lithium Aluminum Hydride*, Inorg. Chem. (1965) **4**, 304.
- [2.44] Fichtner M., Fuhr O., Kircher O., *Magnesium alanate - a material for reversible hydrogen storage?*, J. Alloys Compd. (1997) **356-357**, 418.
- [2.45] Jensen C. M., Zidan R., Mariels N., Hee A., Hagen C., *Advanced titanium doping of sodium aluminum hydride: segue to a practical hydrogen storage material?*, Int. J. Hydrogen Energ. (1999) **24**, 461.
- [2.46] Jensen C.M., Gross K.J., *Development of catalytically enhanced sodium aluminum hydride as a hydrogen-storage material*, J. Appl. Phys. A (2001) **72**, 213.
- [2.47] Chen P., Xiong Z., Luo J., Lin J., Lee Tan K., *Interaction of hydrogen with metal nitrides and imides*, Nature (2002) **420**, 302.
- [2.48] Hu Y. H., Ruckenstein E., *Ultrafast Reaction between LiH and NH₃ during H₂ Storage in Li₃N*, J. Phys. Chem. A (2003) **107**, 9737.
- [2.49] Chen P., Xiong Z., Luo J., Lin J., Tan K. L., *Interaction between Lithium Amide and Lithium Hydride*, J. Phys. Chem. B (2003) **107**, 10967.
- [2.50] Lu J., Fang Z. Z., Sohn H.Y., *A Dehydrogenation Mechanism of Metal Hydrides Based on Interactions between H^{δ+} and H*, Inorg. Chem. (2006) **45**, 8749.
- [2.51] Orimo S., Nakamori Y., Kitahara G., Miwa K., Ohba N., Noroitake T., Towata S., *Destabilization and enhanced dehydriding reaction of LiNH₂: an electronic structure viewpoint*, Appl. Phys. A (2004) **79**, 1765.
- [2.52] Luo W., *(LiNH₂-MgH₂): a viable hydrogen storage system*, J. Alloys Compd. (2004) **381**, 284.
- [2.53] Xiong Z. T., Wu G. T., Hu J. J., Chen P., *Ternary Imides for Hydrogen Storage*, Adv. Mater. (2004) **16**, 1522.
- [2.54] Yang J., Sudik A., Wolverton C., *Activation of hydrogen storage materials in the Li-Mg-N-H system: Effect on storage properties*, J. Alloys Compd. (2006) **430**, 334.

- [2.55] Xiong Z., Hu J., Wu G., Chen P., Luo W., Gross K., Wang J., *Thermodynamic and kinetic investigations of the hydrogen storage in the Li–Mg–N–H system*, J. Alloys Compd. (2005) **398**, 235.
- [2.56] W. Luo, E. Rönnebro, *Towards a viable hydrogen storage system for transportation application*, J. Alloys Compd. (2005) **404–406**, 392.
- [2.57] Orimo S., Nakamori Y., Kitahara G., Miwa K., Ohba N., Towata S., Züttel A., *Dehydriding and rehydriding reactions of LiBH₄*, J. Alloys Compd. (2005) **404–406**, 427.
- [2.58] Züttel A., Borgschulte A., Orimo S., *Tetrahydroborates as new hydrogen storage materials*, Scripta Mater. (2007) **56**, 823.
- [2.59] Züttel A., Wenger P., Rentsch S., Sudan P., Mauron Ph., Emmenegger Ch., *LiBH₄ a new hydrogen storage material*, J. Power Sources (2003) **118**, 1.
- [2.60] Orimo S., Nakamori Y., Ohba N., Miwa K., Aoki M., Towata S., Züttel A., *Experimental studies on intermediate compound of LiBH₄*, Appl. Phys. Lett. (2006) **89**, 21920.
- [2.61] Soldate A. M., *Crystal Structure of Sodium Borohydride*, J. Am. Chem. Soc. (1947) **69**, 987.
- [2.62] Li H. W., Kikuchi K., Nakamori Y., Miwa K., Towata S., Orimo S., *Effects of ball milling and additives on dehydriding behaviors of well-crystallized Mg(BH₄)₂*, Scripta Mater. (2007) **57**, 679.
- [2.63] Matsunaga T., Buchter F., Mauron P., Bielman M., Nakamori Y., Orimo S., Ohba N., Miwa K., Towata S., Züttel A., *Hydrogen storage properties of Mg[BH₄]₂*, J. Alloys Compd. (2008) **459**, 583.
- [2.64] Soloveichik G. L., Gao Y., Rijssenbeek J., Andrus M., Kniajanski S., Bowman R. C., Hwang S., Zhao J., *Magnesium borohydride as a hydrogen storage material: Properties and dehydrogenation pathway of unsolvated Mg(BH₄)₂*, Int. J. Hydrogen Energ. (2009) **34**, 916.
- [2.65] Miwa K., Aoki M., Noritake T., Ohba N., Nakamori Y., Towata S., Züttel A., Orimo S., *Thermodynamical stability of calcium borohydride Ca(BH₄)₂*, Phys Rev. B (2006) **74**, 155122.

- [2.66] Barkhordarian G., Jensen T. R., Doppiu S., Bolsenberg U., Borgschulte A., Gremaud R., Cerenius Y., Dornheim M., Klassen T., Bormann R., *Formation of $\text{Ca}(\text{BH}_4)_2$ from Hydrogenation of $\text{CaH}_2+\text{MgB}_2$ Composite*, J. Phys. Chem. C (2008) **112**, 2743.
- [2.67] Kim J., Jin S., Shim J., Cho Y. W., *Reversible hydrogen storage in calcium borohydride $\text{Ca}(\text{BH}_4)_2$* , Scripta Mater. (2008) **58**, 481.
- [2.68] Wang L., Graham D. D., Robertson I. M., Johnson D. D., *On the Reversibility of Hydrogen-Storage Reactions in $\text{Ca}(\text{BH}_4)_2$: Characterization via Experiment and Theory*, J. Phys. Chem. C (2009) **113**, 20088.
- [2.69] Orimo S., Nakamori Y., Züttel A., *Material properties of MBH_4 ($M=\text{Li, Na, and K}$)*, Mater. Sci. Eng. B (2004) **108**, 51.
- [2.70] Nakamori Y., Miwa, K., Ninomiya, A., Li H. W., Ohba N., Towata S., Züttel A., Orimo S., *Correlation between thermodynamical stabilities of metal borohydrides and cation electronegativities: First-principles calculations and experiments*, Phys. Rev. B (2006) **74**, 45126.

Chapter 3

Preparation and characterization techniques

3.1 Introduction

This chapter deals with the main preparation procedures and experimental techniques used during the work. In particular, theory and technical details are presented on: mechanical alloying of which high energy ball milling is a branch, a powerful preparation technique for nanocrystalline materials and the preparation of homogeneous mixtures; gas volumetric Sievert's measurements, used for the characterization of kinetics and thermodynamics of hydrogen absorption/desorption (a/d) by materials; X-Ray Diffraction, which provides important structural and microstructural information on solids, analysed by Rietveld refinement; Measurement of specific surface area of solids by BET (Brunauer-Hemmet-Teller) method, which provides information on high surface area materials.

3.2 The mechanical alloying and high energy ball milling

The mechanical alloying is a non equilibrium solid state powder processing technique developed around 1966 by John Benjamin and co-workers [3.1-3.3]. The technique, initially developed to produce fine, uniform dispersions of oxides (Al_2O_3 , Y_2O_3 , ThO_2) in nickel-base alloys to be used in gas turbines for the aerospace industry. It is worth noting that these materials cannot be obtained by the conventional powder metallurgy method. It is still an

established industrial technology for the production of ferromagnetic amorphous sheets used in electrical transformers obtained by powder sintering. It has been subsequently exploited for the production of nanocrystalline powders, to obtain metastable phases, to extend the solubility limits of solid solutions, to finely mix powders and to obtain mechano-chemical reactions. Along with other non equilibrium techniques, such as rapid solidification from liquid state, plasma processing, ion implantation and vapour deposition, the processed material is brought to a metastable state by an external dynamic forcing (storing of mechanical energy by plastic deformation in this case). The processed materials are then “quenched” in a frozen state that can give interesting physical and mechanical properties.



Figure 3.1 SPEX 8000M shaker mill (left) and home made vial with stainless steel balls (right).

The process consists of loading the powder material into a vial along with a grinding medium, generally represented by stainless steel balls. The motion applied to the vial and the applied energy depend on the type of used mill.

Shaker mills are the most commonly used in the laboratory scale, since they allow to mill only 10-20 g of powder, but with an efficiency far higher compared to other mill types. The mill used in the works presented in this thesis is a SPEX 8000M shaker mill, one of the most efficient available on the market. In this mill the shaking motion is combined with lateral movements of the vial resulting in a 8 shape trajectory. Because of the amplitude of the motion of about 5 cm and the frequency of about 1200 rpm, the speed of the balls inside the vial is particularly high (about 5 m/s) and the force of the ball's impact as well. For this reason in this case it is possible to use the words *high energy ball milling*. In figure 3.1 the mill and the home made vial that have been used in the presented research are shown. The vial is equipped with a valve allowing to vary the milling atmosphere and pressure using an inert gas like Ar or other gases in the case of reactive milling (e.g. H₂ or N₂ to obtain hydrides or nitrides).

In *planetary* mills, as a planet moves around the sun, the vial spins on his own axis and at the same time in the opposite direction around a central axis. These mills allow to process a few hundred grams of powder and, due to the planetary motion, the centrifugal forces alternatively act in the opposite direction allowing the grinding balls to apply on the powder a friction and a impact effect as represented in figure 3.2. Even if the speed of the balls is

generally higher than in shaker mills, the frequency of the impacts is lower. Thus, the planetary mills are less efficient than the shaker mills [3.4].

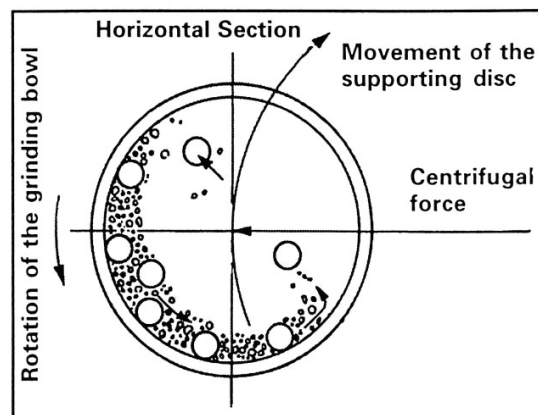


Figure 3.2 Schematic representation of ball motion in a planetary mill [3.4].

In the *attritor* mills, the milling occurs in a stationary vial filled with balls and the powder by the stirring action of a vertical rotating central shaft with horizontal arms (impellers). The rotation speed of the central shaft is about 250 rpm (4.2 Hz) [3.5]. In this type of mills it is possible to process larger quantities of powder (from 0.5 to 40 Kg) [3.4]. A drawing of the vial of an attritor mill is represented in figure 3.3.

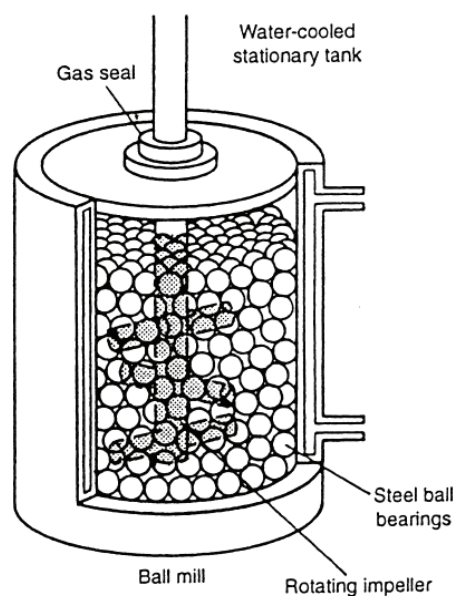


Figure 3.3 Vial of an attritor mill [3.4].

The mechanical alloying process is influenced by several factors. It is well known that the properties of the final product, particle size distribution, degree of disorder, amorphization, and final stoichiometry, depend on the milling conditions. These factors are:

- type of mill;
- the milling media material (e.g., ceramics, stainless steel, and tungsten carbide);

- milling atmosphere (e.g., air, nitrogen, hydrogen or an inert gas);
- milling environment (e.g., dry milling or wet milling);
- milling ball-to-powder weight ratio;
- milling temperature;
- milling time.

During high-energy milling the powder particles are repeatedly cold welded, fractured and rewelded. The force of the impact plastically deforms the powder particles leading to work hardening and fracture. The new surfaces created enable the particles to weld together and this leads to an increase in particle size. Since in the early stages of milling the particles are soft (if we are using either ductile-ductile or ductile-brittle material combination), their tendency to weld together and form large particles is high. With continued deformation, the particles get work hardened and fracture by a fatigue failure mechanism. Fragments generated by this mechanism may continue to reduce in size. At this stage, the tendency to fracture predominates over cold welding. Figure 3.4 shows an example of the dependence of particle size and powder morphology according the mentioned mechanism.

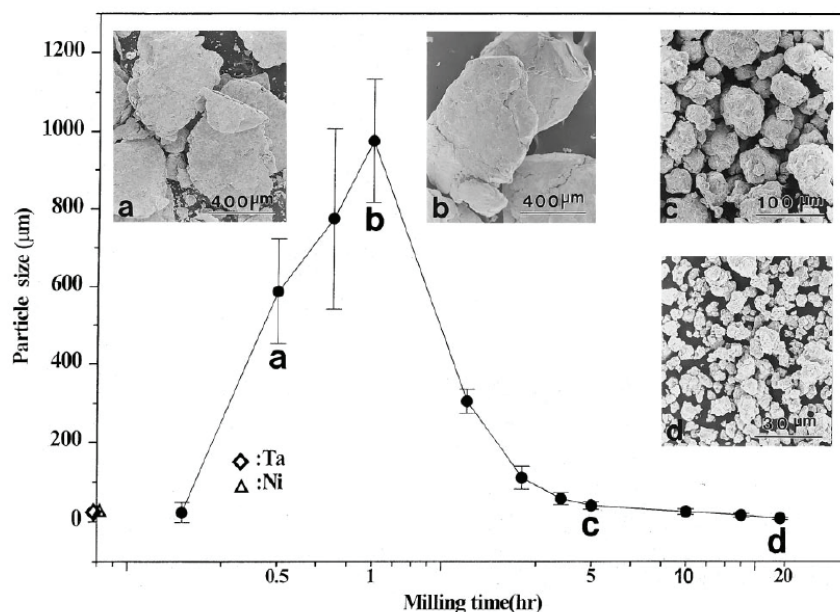


Figure 3.4 Particle size distribution of a nickel-base alloy caused by tendency of small particles to weld together and large particles to fracture under steady-state conditions [3.4].

The mechanism for formation of nanocrystalline materials by the ball milling technique has been proposed by Fecht [3.6], who summarized the phenomenology into three stages. The first stage is the plastic deformation produced in the crystal lattices of the ball milled powders by slip and twinning. During this stage of milling, the atomic level strain increases as a result of increasing the dislocation density. In the second stage, due to the successive accumulation of the dislocation density, the crystals are disintegrated into subgrains that are initially separated by low-angle grain boundaries. The formation of these subgrains is attributed to the

decrease of the atomic level strain. In the third stage further ball milling causes further deformation which leads to subgrain size reduction so that the orientation of the final grains becomes random in crystallographic orientations and hence the direction of slip varies from one grain to another.

3.3 X-ray diffraction

3.3.1 The Bragg law

X-ray diffraction, discovered by Max von Laue in 1912, is a versatile and non-destructive analytical technique that allows to study the structural and microstructural characteristics of crystalline matter. It is based on the elastic interaction of a monochromatic X-ray with the atomic lattice of the studied substance and follows the Bragg law, which will be derived in the following.

Referring to figure 3.5, let's consider rays I and Ia striking atoms K and P in the first plane of atoms. The atoms scatter the incident radiation in all directions, but only in the directions I' and Ia' the scattered beams can be in phase reinforcing one another. This only happens if the difference in length of path between the wave fronts XX' and YY' is equal to:

$$QK-PR = PK \cos(\theta) - PK \cos(\theta) = 0, \quad (3.1)$$

Similarly, the rays scattered by all the atoms in the first plane in a direction parallel to I' are in phase and add their contributions to the diffracted beam. This will be true of all the planes separately, and it remains to find the condition for reinforcement of rays scattered by atoms in different planes. Rays I and 2 , for example, are scattered by atoms K and L , and the path difference for rays IKI' and $2L2'$ is

$$ML+LN = d' \sin(\theta) + d' \sin(\theta) = 2d' \sin(\theta). \quad (3.2)$$

This is also the path difference for the overlapping rays scattered by S and P in the direction shown, since in this direction there is no path difference between rays scattered by S and L or P and K . Scattered rays I' and $2'$ will be completely in phase if this path difference is equal to a multiple integer n of λ :

$$n\lambda = 2d' \sin(\theta). \quad (3.3)$$

This relation was first formulated by W. L. Bragg. It states the essential condition satisfied for a h, k, l family of planes when X-ray reflection (or diffraction) occurs. n is called the order of reflection and can assume all the integer values respecting the relationship:

$$\frac{n\lambda}{2d'} = \sin(\theta) \leq 1. \quad (3.4)$$

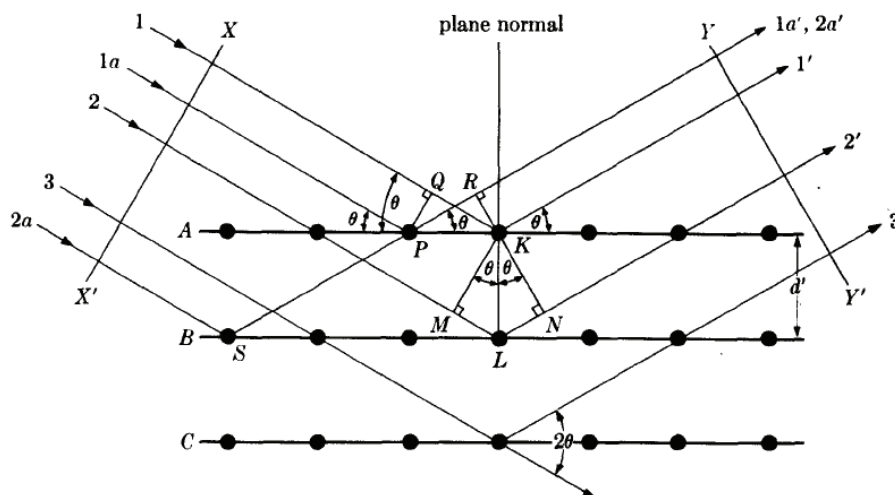


Figure 3.5 Diffraction of X-rays by a crystal [3.7].

3.3.2 Instrumental setup

In the work presented in this thesis a Philips PW1820/00 diffractometer with the $\text{Cu-K}\alpha$ radiation ($\lambda=1.5418 \text{ \AA}$) has been used. As shown in figure 3.6, representing the working scheme of the instrument, the diffractometer allows measurements with two geometries. The geometry used in this work, represented on the right, is the so called Bragg-Brentano, under which both the sample and the detector rotate during the scan, but the angular velocity of the detector is twice that of the sample. In this way, the incidence and reflection angles remain equal to each other during the scan with respect to the sample plane.

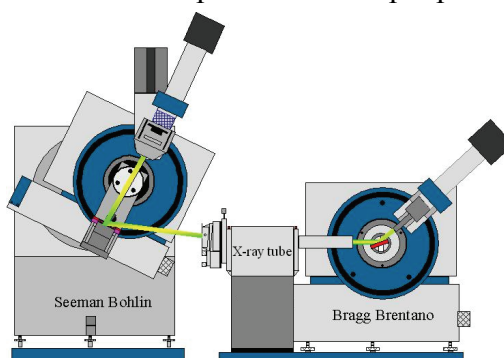


Figure 3.6 Scheme of the diffractometer.

It is a parafocusing geometry according which a divergent beam coming from the X-ray tube passes through a divergence slit and a Soller slit collimator before reaching a plane sample; the diffracted beam is then focused by the sample to the detector after passing through a second Soller slit and a receiving slit. The parafocusing effect is ensured by the fact that the focus of the X-ray tube and the detector are at the same distance from the axis of the goniometer; it is important that the sample is flat and positioned on the axis of the goniometer. The second geometry is the so called Seeman-Bohlin (shown on the left) whereby the angle of incidence remains constant and very low respect to the sample plane

during the measurement (2° - 5°), while only the detector is moved. This geometry is useful when analyzing thin films in order to minimize the contribution of the substrate.

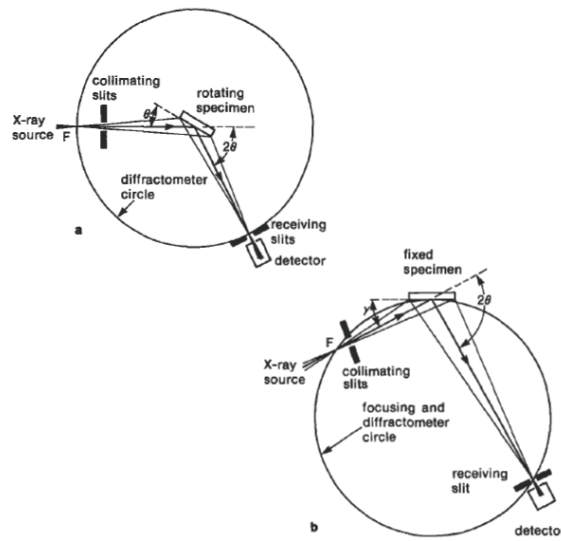


Figure 3.7 Bragg-Brentano (a) and Seeman-Bohlin (b) para-focusing geometries [3.8].

3.3.3 The Rietveld method

The qualitative and quantitative analysis of XRD profiles was carried out using the Rietveld method. It is an iterative minimization procedure, based on a function including several structural and microstructural parameters of the system. The method was developed during the 60's and was at the beginning only restricted to the refinement of atomic positions from neutron diffraction profiles [3.9]. The refinement method is based on individual intensities y_{ci} at every 2θ of a powder diffraction profile and not based on integrated intensities, as for single crystal structure refinements [3.10]. It is based on the complete diffraction profile, including background, called originally "full pattern refinement" for this reason. Basing the calculation on individual intensities is very useful because, especially in the case of powder diffraction, it overcomes the problem of the systematic (due to cubic or trigonal symmetry), and accidental (due to poor resolution) peak overlaps. The information hidden in a powder diffraction profile that can be obtained by Rietveld fitting include: lattice parameters and space group derived from peak positions; crystal domain size and residual stress/strain from the broadening and FWHM of the peaks; qualitative and quantitative phase analysis.

According to the method, the individual diffraction intensities can be calculated according the function:

$$y_{ci} = s \sum_H L_{\bar{H}} |F_{\bar{H}}|^2 \phi(\theta_i - \theta_{\bar{H}}) O_{\bar{H}} A + y_{bi}, \quad (3.5)$$

where s is a scale factor depending on several factors as the intensity of the incident radiation and the amount of sample interacting with it; \bar{H} is a vector of the reciprocal space representing the h th Bragg reflection, due to the family of planes represented by the Miller

indices (h, k, l); $L_{\bar{H}}$ includes the Lorentz factor depending on the symmetry of the crystal structure; $\phi(\theta_i - \theta_{\bar{H}})$ is the value of the function representing the reflection profile at the angular position θ_i ; $O_{\bar{H}}$ is the preferred orientation factor; A is absorption factor; $F_{\bar{H}}$ is a structural factor represented as follows:

$$F_{\bar{H}} = \sum_{j=1, \dots, n} N_j f_j \exp[2\pi i \bar{H} \cdot \bar{X}^j] \exp\left[-B_j \sin^2 \frac{\theta}{\lambda^2}\right], \quad (3.6)$$

where j runs over the n atoms in the asymmetric unit; \bar{X}^j is the vector of real space representing the position of j^{th} atom. f_j is the atomic shape factor of the j^{th} atom, indicating how the electrons respond to the electromagnetic field; B_j are the atomic (isotropic) Debye-Waller factors and N_j the occupation number of each crystallographic site.

Using the data obtained from an X-ray diffraction profile it is possible to calculate the quantity S that should be minimized during the refinement:

$$S = \sum_i w_i (y_{oi} - y_{ci})^2, \quad (3.7)$$

where y_{oi} is the intensity of each step, y_{ci} is the value calculated from equation (3.5) and w_i the weight of each observation point.

Obviously, the larger the number of known parameters, the more reliable are the obtained results. Moreover, it is important that the starting parameters are reasonably close to the final values in order to reach the convergence with small changes of the parameter to be refined. Many shape functions have been proposed in order to improve the interpolation of the peaks, where further parameters have been included, taking into account peak asymmetry and broadening, crystalline domain size and residual stress/strain.

3.4 Gas reaction controlling with a volumetric Sievert's apparatus

The characterization of solid-gas reactions studied in this thesis work has been performed through a *Gas Reaction Controller* provided by *Advanced Materials Corporation (Pittsburgh)*. It is a volumetric Sievert's apparatus, whose basic working scheme is shown in figure 3.8, allowing the measurement of absorption/desorption kinetics, at constant temperature and quasi-constant pressure giving information on the speed and mechanisms of absorption and desorption of a gas from a solid sample. It also allows the measurement of the system equilibrium pressures at constant temperature (PCI curves, Pressure Composition Isotherms). The equipment can be controlled using a LabView-based software installed on a computer connected to the instrument, allowing to set the experimental conditions and to program automatic measurements tables. Figure 3.9 shows the control panel from which all the operations of the machine can be followed. The figure reproduces schematically the

system of calibrated volumes. The sample is placed within a sample holder (sample CH1) of about 2 cm³, capable of operate up to 200 atm of hydrogen. During the measurements, the sample holder is placed inside an oven controlled by the software, which can vary the sample temperature from room temperature up to 500 ° C. A *k*-type thermocouple in direct contact with sample provides the temperature measurement. It is possible to perform measurements even at low temperatures using a thermal bath consisting of dry ice or liquid nitrogen. The highly sensitive pressure gauges are based on the detection of the deformation of steel membranes. They are of two types: one working in the range 0-20 atm (LP0 in figure 3.9) and capable of an accuracy of 0.003 atm, the second type (HP0, HP1 and HP2 in Figure 3.9) working up to 200 atm and having an accuracy of 0.03 atm. The measurements can be performed in manual mode, but usually are carried out automatically, using one of the following standards:

Soak Mode: Useful to get information about hydrogen absorption kinetics. The sample chamber, previously evacuated, is connected to the “high pressure manifold” (see figure 3.9) containing hydrogen. The hydrogen pressure is chosen high enough to be higher than the plateau pressure of the system when the pressure equilibrium is reached after the opening of the connecting valves. Obviously, during the measurements the pressure cannot be kept constant, even if the volumes are large enough to obtain measurements with small pressure drops with respect to the plateau pressure. Data concerning pressure, temperature and amount of absorbed gas vs. time are periodically collected. The absorbed gas amount is calculated from the pressure drop since all the volumes are calibrated. A third order virial expansion of the ideal gas law is used for the calculation:

$$n = (pv / RT) / \left\{ 1 + B(T) \frac{n}{v} + C(T) \frac{n^2}{v^2} + D(T) \frac{n^3}{v^3} \right\}, \quad (3.8)$$

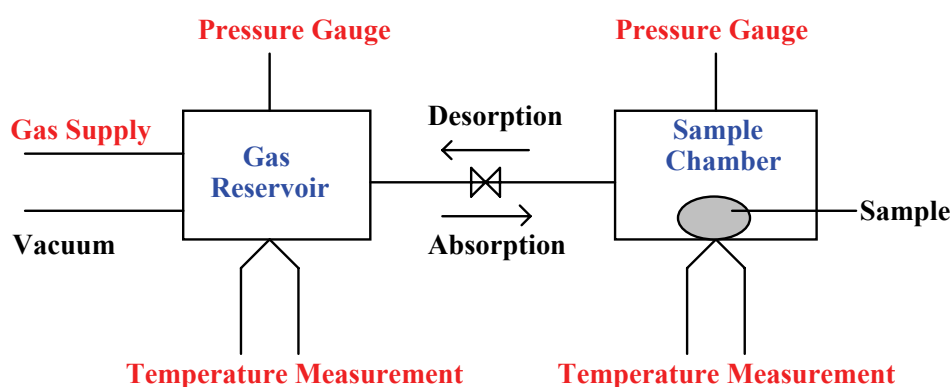


Figure 3.8 Working scheme of Sievert's volumetric apparatuses.

where n is the number of gas moles, p the pressure, T the absolute temperature, R the gas constant, $B(T)$, $C(T)$ and $D(T)$ the second, third and fourth virial coefficients that depend on the temperature. The number of moles n is calculated by numerical iteration.

Release Mode: Before the measurement start the sample chamber is filled with a hydrogen pressure higher than the plateau pressure in order to keep the sample hydrogenated. It is then connected to the high pressure manifold and low pressure manifold previously evacuated. These two volumes are about 20 times larger than the sample chamber and, when the valves are open, the reached pressure equilibrium is lower than the system plateau pressure. The sample starts then desorbing hydrogen. The amount of desorbed gas is calculated from the pressure increase. The data are collect analogously as for *soak mode*.

PCI Adsorption Mode: Determines the pressure-composition isotherms of the system at constant temperature. The sample chamber is periodically connected to the “high pressure manifold” in order to increase the pressure by adjustable small steps. In between each step the instrument waits for the system to reach the equilibrium pressure.

PCI desorption Mode: As in the previous measurement mode, but decreasing the system pressure by small steps.

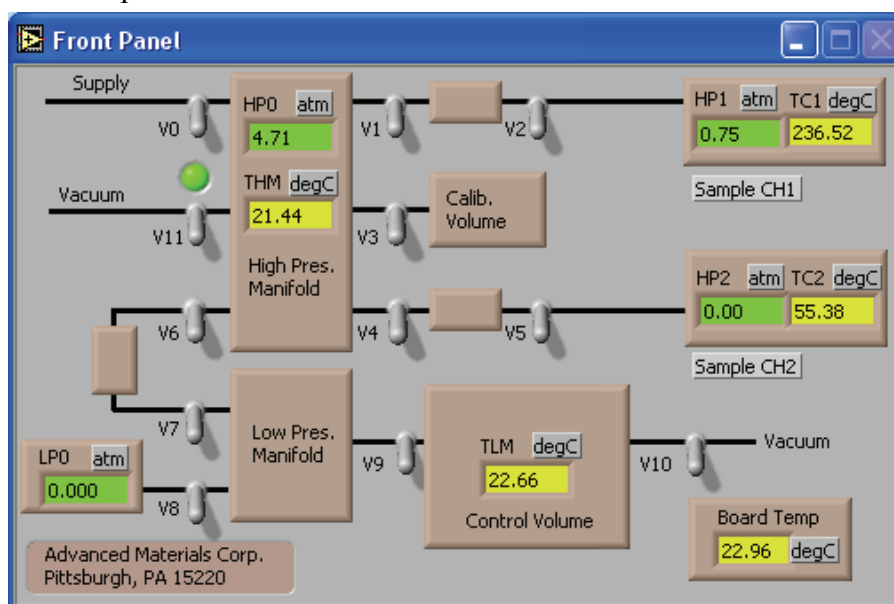


Figure 3.9 Control panel of the LabView-based software also representing the calibrated volumes, pressure gauges, thermocouples and solenoid valves.

3.5 Measurement of Specific Surface Area of solids by BET method

The measurements of specific surface area of solids by BET method uses the process of physical adsorption of a gas on the surface of the solid. It is a spontaneous process dominated

by molecular interaction forces (e.g. van der Waals and dispersion forces) driven by the decrease of entropy, since the molecule in the gas phase have three degrees of freedom while in the adsorbent phase it has only two. For this reason the process is always exothermic. The physically adsorbed gases on the surface of the solid can be easily removed by evacuation at the same temperature at which adsorption occurred.

The adsorption is measured looking at the volume of adsorbed gas measured in cm^3 at Standard Pressure and Temperature (STP) vs. the pressure (measured in mm Hg) of the adsorbing gas at constant temperature. For this reason these measurements are named *isotherms*. Several types of isotherms exist with different shapes, depending on the adsorption mechanism. Examples of isotherm types are shown in figure 3.10.

Type I isotherms occur when the adsorption does not go beyond one monolayer and is found in porous materials with pore size comparable with the molecular dimensions. Types IV and V are typical of multilayer adsorption where the flat region at the higher pressures is due to the filling of capillaries. Type II isotherms are the most commonly observed and are the same of type IV except for the filling of capillaries. Type III are the most rarely observed and occur for nonwetting systems.

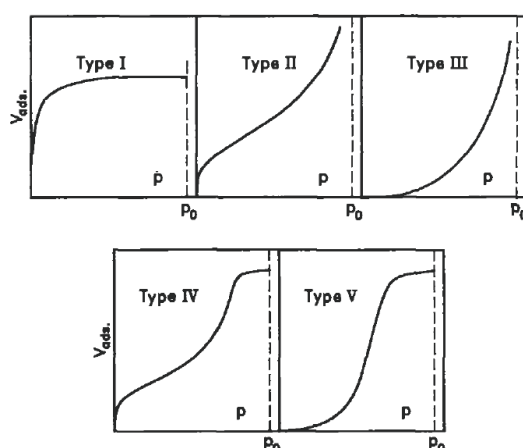


Figure 3.10 The five types of physical adsorption isotherms. p_0 is the vapour pressure [3.8].

Usually, volumetric systems similar to that shown in the previous paragraph are used. Here N_2 is the adsorbing gas and the sample is taken at liquid N_2 temperature (77 K). In this work a Quantachrome Nova 1200e analyzer has been used. The first step in the experimental procedure to get an adsorption isotherm is the sample outgassing, needed to remove adsorbed water or other gases on the surface. The second step is the calculation of the *effective* volume of the sample cell, using a non adsorbing gas as helium when the cell is at 77 K. The amount of used gas is measured with a calibrated volume and an accurate measurement of the pressure with a gauge. Subsequently, N_2 is used for the surface area determination. Its pressure in the sample cell is increased by steps after the equilibrium pressure has been reached each time. The amount of adsorbed gas is recorded at each step. Knowing the

effective volume of the system, it is possible to calculate the adsorbed gas volume by measuring the pressure drop with respect to that expected in absence of the sample.

It is possible to evaluate the specific surface area of a sample from an isotherm, using the BET equation developed by Brunauer, Hemmet and Teller in 1938 [3.11]:

$$\frac{p}{v(p_0 - p)} = \frac{1}{v_m} + \left(\frac{c-1}{v_m c} \right) \frac{p}{p_0}, \quad (3.9)$$

where v is the volume of adsorbed gas in cm^3 at SPT per gram of solid at the pressure p , v_m is the monolayer volume measured in cm^3/g and c is related to the heat of adsorption. Plotting $p/v(p_0-p)$ vs. p/p_0 a straight line is obtained from the experimental data. From the slope $((c-1)/v_m c)$ and from the intercept $(1/v_m)$ it is possible to calculate v_m and c . From v_m it is possible to calculate the specific surface area Σ by using the equation:

$$\Sigma = 0.269 \sigma v_m, \quad (3.10)$$

where σ is the molecular area that for N_2 is 16.2 \AA^2 and the numerical factor comes from the Loschmidt's number (molecules per cm^3 at STP). When the isotherms are obtained near the boiling point of the adsorbed gas as for N_2 at 77K, the BET equation is valid in the relative pressure p/p_0 range of 0.05÷0.35.

- [3.1] Benjamin J. S., *Mechanical alloying*, Sci. Amer. (1976) **234**, 40.
- [3.2] Benjamin J. S. In: Arzt E, Schultz L, ed.. *New materials by mechanical alloying techniques* (1989). Oberursel, Germany: DGM Informationgesellschaft.
- [3.3] Benjamin J. S., Metal Powder Rep. (1990) 45, 122.
- [3.4] Suryanarayana C., *Mechanical alloying and milling*, Progr. Mater. Sci. (2001) **46**, 1.
- [3.5] El-Eskandarany M. S., *Mechanical Alloying For Fabrication Of Advanced Engineering Materials*, William Andrew Publishing, Norwich, New York, U.S.A.
- [3.6] Johnson, W. L., *Thermodynamic and kinetic aspects of the crystal to glass transformation in metallic materials*, Prog. Mater. Sci. (1986) **30**, 81.
- [3.7] Cullity B. D., *Elements of X-ray Diffraction* (2nd edition), Addison-Wesley Publishing Company Inc.
- [3.8] Brundle C. R., Evans C. A. Jr., Wilson S. (ed.), *Encyclopedia of Materials Characterisation – Surfaces, Interfaces, Thin Films*, Butterworth-Heinemann eds.
- [3.9] Rietveld H. M., *Line profiles of neutron powder-diffraction peaks for structure refinement*, Acta Cryst. (1967) **22**, 151.
- [3.10] Will G., *Powder Diffraction: The Rietveld Method and The Two Stage Method*, Springer-Verlag Berlin Heidelberg 2006.
- [3.11] Brunauer S., Emmett P. H., Teller E., *Adsorption of Gases in Multimolecular Layers*, J. Amer. Chem. Soc. (1938) **60**, 309.

Chapter 4

Reaction of hydrogen with the $\text{TiCr}_{1.78-x}\text{Mn}_x$ Laves phase (C14)

4.1 Motivation for this study

Recently the AB_2 Laves phase $\text{Ti}(\text{Cr},\text{Mn})_{1.8}$ has attracted a lot of attention for its potential use with hybrid hydrogen storage tanks, which are found to allow higher hydrogen mass densities than those only containing compressed H_2 gas (35 MPa). Figure 4.1 represents some typical PCI curves for the Ti-Cr-Mn-H system, showing a reversible H_2 capacity of 1.8 wt% at 23 °C, an absorption pressure of 320 atm and desorption of 1 atm [4.1]. According to the model proposed by Takeichi et al. [4.2] such a material could be viable to be used on a storage system, schematically represented in figure 4.2, combining the advantage of gravimetric capacity of high pressure vessels with the high volumetric capacity of metal hydrides. This system has attracted the interest of the automotive industry like in the case of Toyota Motors [4.3].

In spite of this interest, the $\text{TiCr}_{1.8-x}\text{Mn}_x$ system appears not to have been extensively studied from various points of view. For example, H diffusion data are only available for the binary compound TiCr_2 [4.4, 4.5]. Also the thermodynamic behaviour of the H solid solution (α -phase) is scarcely known, since only the C15 form of the binary compound has been investigated so far [4.6].

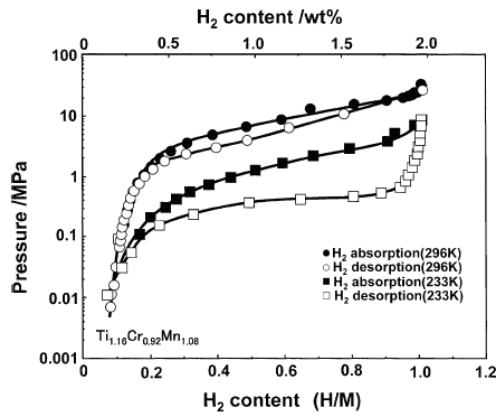


Figure 4.1 H_2 absorption and desorption isotherms for Ti-Cr-Mn-H system [4.3].

Thus, an investigation has been performed on this pseudo-binary compound. In this chapter, pressure-composition isotherms (PCI curves) are presented for the $TiCr_{1.8-x}Mn_xH_y$ system, together with the thermodynamic quantities derived from the associated van't Hoff plots.

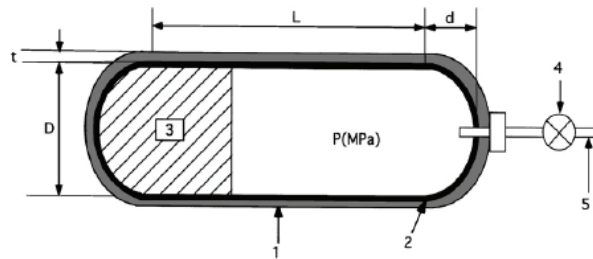


Figure 4.2 A schematic view of a hybrid hydrogen storage vessel: (1) carbon fiber and epoxy resin, (2) thin aluminium liner, (3) hydrogen storage alloy, (4) valve, (5) tube for hydrogen [4.2].

4.2 Sample preparation and analysis of $TiCr_{1.78-x}Mn_x$ alloy

Four $TiCr_{1.78-x}Mn_x$ alloys ($x=0, 0.4, 0.6, 0.8$) were prepared by arc melting at the Institute for Energy and Interphases (IENI) of CNR in Lecco. The as cast buttons were re-melted several times for homogenisation and ground in a mortar for the subsequent structural and thermodynamic characterization. The structure of the as cast and H-cycled materials was checked by XRD diffraction. The PCI curves were obtained at a given constant temperature with the sample holder in an oven or in a cryogenic bath. The pressure was changed step by step whenever the system approached the equilibrium. The kinetic curves were obtained step by step at equal time intervals measuring far from equilibrium the corresponding pressure variations due to the absorption or desorption processes. After every hydrogen absorption and

desorption cycle, an annealing at 400 °C under rotary pump vacuum was performed in order to desorb all the stored hydrogen before the subsequent absorption.

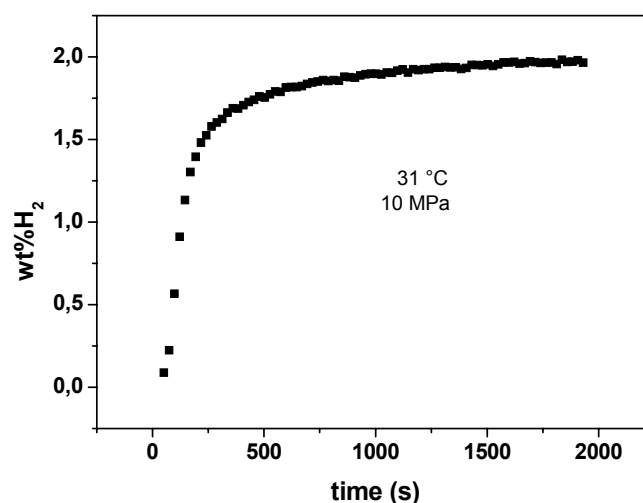


Figure 4.3 Kinetic absorption isotherm of the $\text{TiCrMn}_{0.8}$ compound at 31 °C and 10 MPa.

The compounds in the as cast state could absorb hydrogen without any surface activation. In figure 4.3 a typical kinetic absorption isotherm of the $\text{TiCrMn}_{0.8}$ compound is reported. As seen, the absorption starts immediately after the introduction of the H_2 gas, and a final mass density ρ_{H} (ratio of the hydrogen mass to the hydride total mass) of about 1.98 (corresponding to number of H atoms to the number of total metal atoms per formula unit $n_{\text{H}}=\text{H}/\text{Me}\cong 1$) was reached for a pressure of 10 MPa. The chemical formula of the obtained hydride can be written as $\text{TiCrMn}_{0.8}\text{H}_{\sim 2.8}$.

4.3 Structure of the $\text{TiCr}_{1.78-x}\text{Mn}_x$ alloy as cast and cycled

Diffraction patterns of the as cast compounds revealed the hexagonal C14 structure for all the compositions. Figures 4.4a) and 4.4b) show the XRD patterns of the $\text{TiCrMn}_{0.8}$ and $\text{TiCr}_{1.78}$ as cast and ground samples and after hydrogen a/d. The behaviour of the obtained lattice parameters a and c is shown in figure 4.5. As seen, a is sensibly reduced by substitution of Mn for Cr, while c remains almost unchanged.

As a result, the average atomic volume of the compound decreases as well as the tetrahedral A_2B_2 site holes, whose radius for ideal packing turns out to be equal to $0.074475 a$ [4.7, 4.8]. The XRD patterns of the samples obtained after hydrogenation cycles gave larger lattice parameters, indicating that some hydrogen had remained within the material after evacuation of the reactor chamber from the H_2 gas. This effect decreases by increasing the Mn content in

the alloy, as shown in figure 4.6, where the cell volume change, determined after a hydrogen a/d cycle in the Sievert's apparatus, is plotted against the Mn content.

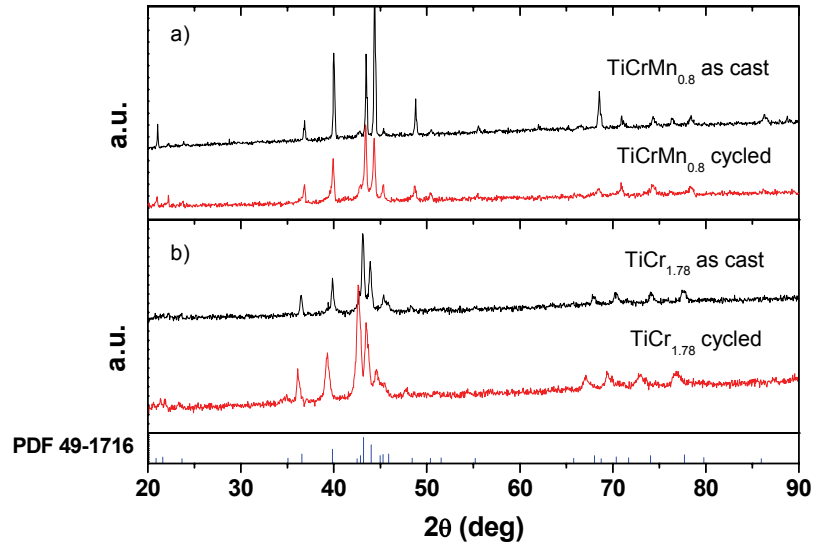


Figure 4.4 X-ray diffraction patterns of the $\text{TiCrMn}_{0.8}$ (a) and the $\text{TiCr}_{1.78}$ (b) compounds.

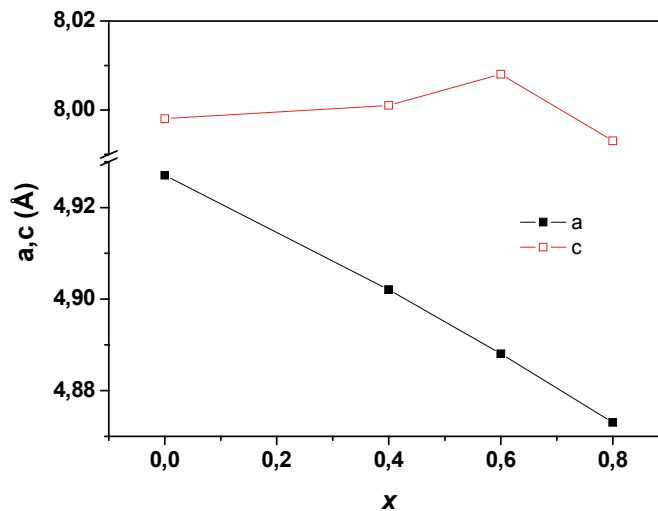


Figure 4.5 Dependence of the cell parameters a and c of the $\text{TiCr}_{1.78-x}\text{Mn}_x$ compounds on the Mn content x .

As a tentative explanation we can consider that hydrogen is trapped at the defects of the crystalline structure and, particularly in this case, at A_3B or A_4 sites that cause a stress in the lattice, since the A atoms have a larger metallic radius than B. When the cell volume is reduced by the presence of more Mn, having a smaller metallic radius with respect to Cr, the

probability of the formation of these defects is lower because their formation causes a higher stress in the crystal structure.

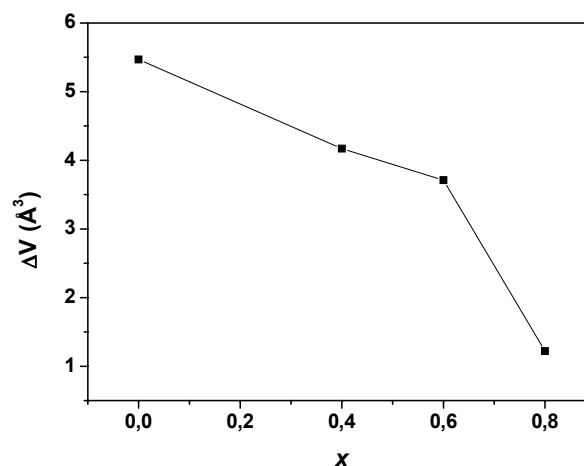


Figure 4.6 Dependence of the difference in cell volume for the $\text{TiCr}_{1.78-x}\text{Mn}_x$ compounds between the as cast material and after absorption/desorption of hydrogen on the Mn content x .

4.4 Thermodynamics of hydrogen a/d by the $\text{TiCr}_{1.78-x}\text{Mn}_x$ alloy

A series of PCI curves and the related van't Hoff plot taken on desorption mode with the $\text{TiCr}_{1.78}$ sample is shown in figure 4.7a). The steep portion of the curves on the left hand side of the diagram corresponds to the H solid solution (α -phase), while the sloping pseudo-plateau occurring at intermediate H contents ($0.35 < \rho_H < 1.1$) represents a region where the solid solution coexists with a hydride phase. A second higher pressure plateau, which appears at the lowest temperature (-60 °C), is indicative of the existence of a higher pressure hydride, where also the AB_3 sites are occupied by H in addition to the A_2B_2 ones. This behaviour of the curves is qualitatively the same as the one reported by Johnson et al. [4.9] and more recently by Beeri et al. [4.10, 4.11].

The van't Hoff plot of figure 4.7a), which has been built taking the dissociation pressure at the inflexion point of the plateaus, provides the values for the decomposition partial molar enthalpy and entropy of the lower pressure hydride. These values, which are reported on the plot, are in reasonable agreement with literature for $\text{TiCr}_{1.9}$ (C14) [4.11]:

$$\Delta\bar{H}_{H_2} = 26.5 \pm 1 \text{ kJmol}^{-1}H_2 \text{ and } \Delta\bar{S}_{H_2} = 122 \pm 4 \text{ JK}^{-1}\text{mol}^{-1}H_2.$$

The desorption isotherms of the ternary $\text{TiCr}_{1.78-x}\text{Mn}_x$ compounds ($x=0.4$; 0.6 and 0.8) are shown in figures 4.7b), 4.7c), and 4.7d), where a single pseudo-plateau is visible. The

thermodynamic quantities derived from the van't Hoff plots associated with figures 4.7b), 4.7c), and 4.7d) are reported on each graph and plotted for more clarity in figure 4.8.

With increasing x , the partial molar enthalpy and entropy both decrease, particularly for values of $x > 0.4$. This behaviour is in agreement with data available in the literature for a series of $\text{TiCr}_{2-x}\text{Mn}_x$ compounds [4.10, 4.11], which also show a decrease in $\Delta\bar{H}_{\text{H}_2}$ and $\Delta\bar{S}_{\text{H}_2}$ with increasing x .

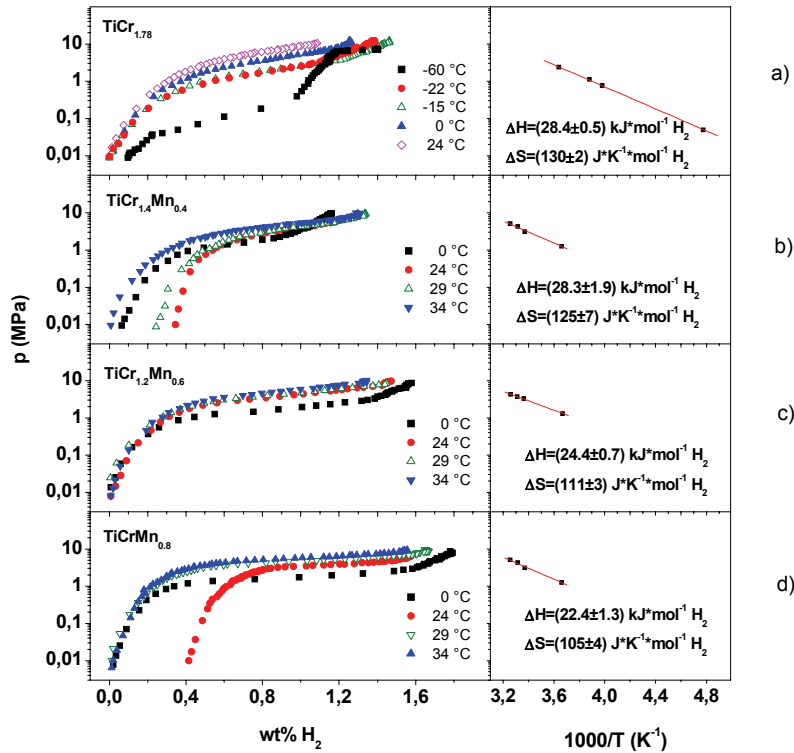


Figure 4.7 PCI curves for the $\text{TiCr}_{1.78-x}\text{Mn}_x$ compounds ($x=0; 0.4; 0.6; \text{ and } 0.8$) and related van't Hoff plots.

With respect to the binary compound $\text{TiCr}_{1.78}$, the PCI curves of the ternary compounds exhibit flatter plateaus and, for comparable temperatures, slightly lower plateau pressures p_d . This second aspect of the curves is more clearly shown in figure 4.9, where p_d is plotted against the Mn content x . As seen, the decomposition pressure p_d appreciably decreases going from $x=0$ to $x=0.4$, while slightly increases for higher values of x . The large initial decrease of p_d is an exception to a rather general rule that a decrease in the cell volume leads to an increase in the plateau pressure. This behaviour, which has also been found for other alloy compositions of the TiCrMn system and for other pressure ranges [4.3], stems from the fact that substitution of Mn for Cr atoms, besides giving rise to a decrease in the cell volume, also affects the transition enthalpy and entropy. Apparently, the overall effect is that of decreasing the absolute value of $\Delta\bar{G}_{\text{H}_2}$ and, consequently, of increasing the hydride stability.

With the $\text{TiCr}_{1.2}\text{Mn}_{0.6}$ and $\text{TiCrMn}_{0.8}$ compounds both absorption and desorption isotherms were measured and little a/d hysteresis was observed, as shown in figure 4.10 for the $\text{TiCr}_{1.2}\text{Mn}_{0.8}$ compound. This hysteresis is low and this is an interesting feature of the ternary hexagonal (C14) TiCrMn system, similarly to the cubic (C15) binary compound $\text{TiCr}_{1.8}$ [4.9], being beneficial for possible applications.

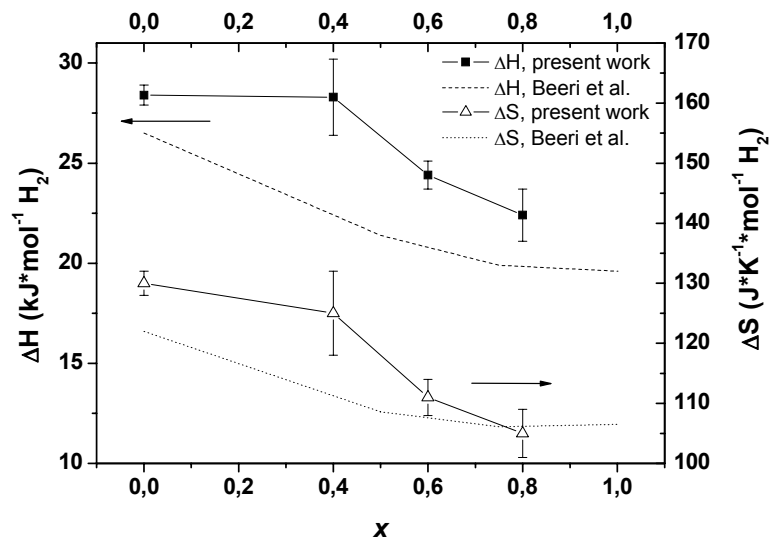


Figure 4.8 Dependence of the ΔH and ΔS of dissociation for the $\text{TiCr}_{1.78-x}\text{Mn}_x$ compounds on the Mn content x .

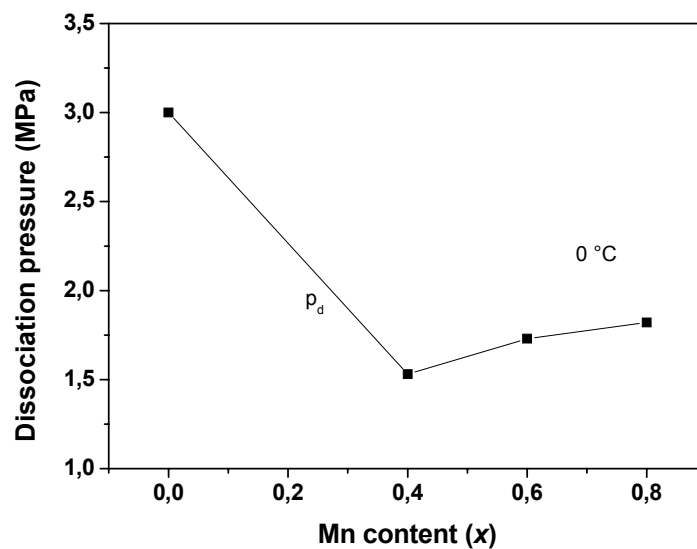


Figure 4.9 Dependence of dissociation pressure for the $\text{TiCr}_{1.78-x}\text{Mn}_x$ compounds on the Mn content x at $0\text{ }^\circ\text{C}$.

In conclusion, the results obtained in this work show that the $\text{TiCr}_{1.78-x}\text{Mn}_x$ compounds under hydrogen pressure absorb considerable amounts of hydrogen at room temperature without needing any surface activation. Increasing the Mn content leads to some interesting advantages for practical applications, such as improved gravimetric capacity, flatter plateau and lower hysteresis.

The results reported in this chapter have been published in [4.12].

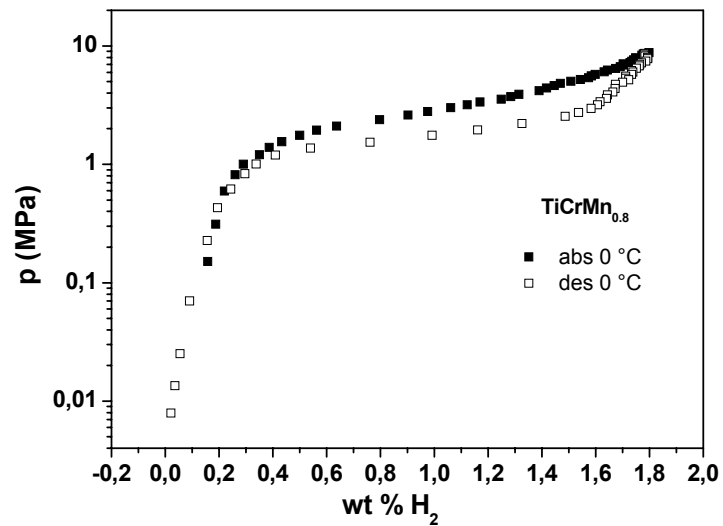


Figure 4.10 PCI curves in absorption and desorption at 0°C for the $\text{TiCrMn}_{0.8}$ compound.

- [4.1] Kojima Y., Kawai Y., Towata S., Matsunaga T., Shinozawa T., Kimbara M., *Development of metal hydride with high dissociation pressure*, J. Alloys Compd. (2006) **419**, 256.
- [4.2] Takeichi N., Senoh H., Yokota T., Tsuruta H., Hamada K., Takeshita H. T., Tanaka H., Kiyobayashi T., Takano T., Kuriyama N., *"Hybrid hydrogen storage vessel", a novel high-pressure hydrogen storage vessel combined with hydrogen storage material*, Int. J. Hydrogen Energ. (2003) **28**, 1121.
- [4.3] Mori D., Haraikawa N., Kobayashi N., Kubo H., Toh K., Tsuzuki M., Shinozawa T., Matsunaga T., *High-Pressure Metal Hydride Tank for Fuel Cell Vehicles*, Proc. MRS Fall Meeting, Boston 2005.
- [4.4] Bowman R. C., Craft B. D., Attalla A., Johnson J. R., *Diffusion behavior in titanium-chromium hydrides*, Int. J. Hydrogen Energ. (1983) **8**, 801.
- [4.5] Campbell S. I., Kemali M., Ross D. K., Bull D. J., Fernandez J. F., Johnson M. R., *Quasi-elastic neutron scattering study of the hydrogen diffusion in the C15 Laves structure, $\text{TiCr}_{1.85}$* , J. Alloys Compd. (1999) **293-295**, 351.
- [4.6] Lynch J. F., Johnson J. R., Reilly J. J., *The Dilute Solution of Hydrogen and Deuterium in (C-15) $\text{TiCr}_{1.8}$* , Z. Phys. Chem. N. F. (1979) **117**, 113.
- [4.7] Magee C. B., Liu J., Lundin C. E., *Relationships between intermetallic compound structure and hydride formation*, J. Less-Common Metals (1981) **78**, 119.
- [4.8] Westlake D. G., *Site occupancies and stoichiometries in hydrides of intermetallic compounds: Geometric considerations*, J. Less-Common Metals (1983) **90**, 251.
- [4.9] Johnson J. R., Reilly J., *Reaction of hydrogen with the low-temperature form (C15) of titanium-chromium (TiCr_2)*, Inorg. Chem. (1978) **17**, 3103.
- [4.10] Beeri O., Cohen D., Gavra Z., Johnson J. R., Mintz M. H., *Thermodynamic characterization and statistical thermodynamics of the $\text{TiCrMn-H}_2(\text{D}_2)$ system*, J. Alloys Compd. (2000) **299**, 217.
- [4.11] Beeri O., Cohen D., Gavra Z., Mintz M. H., *Sites occupation and thermodynamic properties of the $\text{TiCr}_{2-x}\text{Mn}_x\text{-H}_2$ ($0 \leq x \leq 1$) system: statistical thermodynamics analysis*, J. Alloys Compd. (2003) **352**, 111.

- [4.12] Agresti F., Lo Russo S., Maddalena A., Principi G., Mazzolai G., Coluzzi B., Biscarini A., Mazzolai F.M., Tuissi A., *Reaction of hydrogen with the Laves phase (C14) $TiCr_{1.78-x}Mn_x$ compounds*, J. Mater. Sci. Eng. A (2009) **521-522**, 143.

Chapter 5

The hydrogen storage in Mg-Al based pellets

5.1 The problem of Mg-based upscaled system degradation with cycling

As already discussed in chapter 2, MgH_2 is one of the most studied materials among those able to store hydrogen in solid state, having many assets in its favour, like low cost, abundance, light weight and a theoretical storage capacity of 7.6 wt%. However, concerning the practical applications, it has the limitations of high thermodynamic stability and slow hydrogen a/d kinetics [5.1, 5.2]. Many efforts have been made to come out of these practical shortcomings by using MgH_2 in nano-crystalline form obtained by high energy ball milling and using transition metal oxides as catalysts to improve the hydrogen a/d kinetics with little reduction in the gravimetric capacity [5.3-5.7]. Particularly, addition of Nb_2O_5 catalyst during milling has shown one of the fastest kinetics [5.8-5.10].

During scaling up studies of MgH_2 based powders in a specially designed reactor, containing 500 g of material, it was observed that the hydrogen storage capacity as well as the a/d kinetics decreased with the ongoing cycles [5.11]. Figure 5.1 shows the kinetic and hydrogen capacity degradation experienced in the reactor: after only 20 cycles about half of hydrogen capacity is lost and a/d kinetics is much slower than the first cycles. It was argued that this degradation was due to a close compaction of the powder particles inside the reaction chamber associated with local overheating, with the detrimental effect of strongly reducing the free flow of hydrogen through the storage material. The compaction of the powders was probably due to pressure a gradient that built up during the first stages of hydrogen absorption

process given by the difficult gas transport through the Mg bed. An example of the powder compaction in the reactor is shown in figure 5.2.

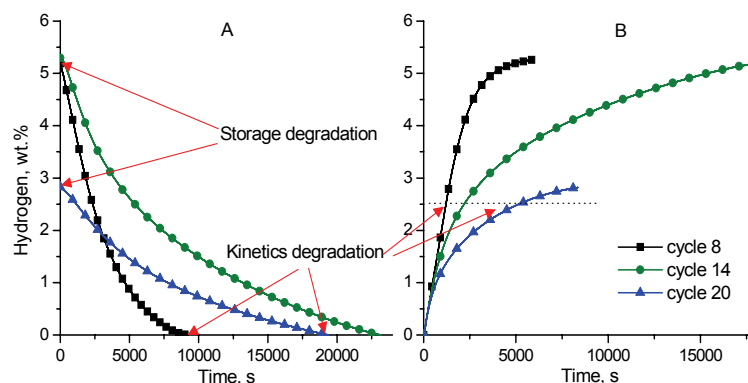


Figure 5.1 Performance degradation of scaled up device in desorption (A) and absorption (B) modes [5.11].

These observations motivated the study of MgH_2 based powders moderately pressed in the form of pellets with the addition of some binding agent in order to retain stable mechanical consistency and structure with persistent free paths for hydrogen diffusion. The use of pellets instead of powder should improve the hydrogen transport inside the storage vessel avoiding pressure gradients and further compaction of the material. Moreover, in principle, each pellet should behave as an independent system reducing scaling up effects on the a/d kinetics.



Figure 5.1 Mg/MgH_2 powder compaction during cycling experienced in the reactor studied in ref. [5.11].

In this chapter the hydrogen storage properties and the mechanical stability of catalysed and ball milled MgH_2 powders mixed with different amounts of Al powder as a binder are presented. The powders have been pressed with an electro-mechanical press, following an approach already preliminarily tested [5.12]. The crystalline structure, the hydrogen a/d properties and the mechanical strength of the samples have been analysed before and after hydrogen a/d cycling by X-ray diffraction.

Recently, Chaise et al. [5.13] have reported the improvement of thermal conductivity in case of compacted MgH_2 disks by incorporation of expanded natural graphite. In our case, the incorporation of aluminium is supposed to further enhance the thermal conductivity in the pellets.

5.2 Samples preparation and analysis

MgH_2 powder (as-received from Th. Goldschmidt GmbH) mixed with Nb_2O_5 (5 wt %) as catalysts of the gas-solid reaction and graphite (1 wt%), was ball-milled in a SPEX 8000M shaker mill for 20 hours using steel balls with ball to powder ratio of 10:1 (hereafter as-milled MgH_2 mixed with Nb_2O_5 and graphite is referred to as catalyzed MgH_2 and denoted as cat- MgH_2). To avoid oxygen contamination, milling was carried out under a little overpressure of argon atmosphere and samples were handled in an argon filled glove-box (M-Braun LABstar MB10 compact). This study was performed on two types of pellets. One made up of as-milled cat- MgH_2 powder and in the other case 5 and 20 wt% of Al powder was homogeneously mixed by ball-milling for 5 min with cat- MgH_2 to act as a binding agent (hereafter these last two types of samples are referred to as cat- MgH_2 -Al5 and cat- MgH_2 -Al20, respectively). All pellets (weighing about 0.3 g and with diameter of 0.7 cm and average height of 0.7 cm) were obtained by pressing the powders in Ar atmosphere with a uniaxial pressure of 180 MPa by means of an Instron 1121 tester. The load was applied with a compressive strain rate of 1 mm/min up to 180 MPa, then the pellet was kept under uniaxial pressure for 60 s, during which the stress was partially reduced, and finally loaded a second time under the same conditions. Structural characterization of the as-prepared powders and of the pellets after a number of hydrogen a/d cycles was done by X-ray diffraction. Samples were prepared in a glove box and covered with a kapton foil to prevent atmospheric contamination. Kinetic and thermodynamic tests were performed using a Sievert's apparatus. Annealing of samples containing Al powder was performed at 450°C in the Sievert's apparatus for 10 min under a rotary pump vacuum before starting the hydrogen a/d cycles. Environmental scanning electron microscopy (ESEM) pictures were acquired with a FEI XL 30 ESEM instrument operated at 20 kV. In order to test the compressive strength resistance of the pellets after different a/d cycles, compression tests were performed using the same Instron 1121 tester at the compressive strain rate of 1 mm/min controlled by the automation software CatMan.

5.3 Cycling of pellets

For all samples the hydrogen release processes were performed at the temperature of 320°C and H_2 pressure of 1.2 atm, while the soak processes were performed at the same

temperature and H_2 pressure of 15 atm. Figure 5.3a) shows the release kinetics for the pellet of cat-MgH₂ and indicates that the maximum stored and released hydrogen in this case was 5.6 wt %, which remained stable for all the hydrogen a/d cycles. The time for a 90% desorption after 20 cycles reduced to 660 s compared to 790 s for the first desorption cycle. During cycling, the pellet lost gradually its mechanical consistency and after 20 cycles got completely powdered. This behaviour is in agreement with the observed continuous reduction of desorption time by cycling, considering that a not close compacted powder favours the hydrogen flow through the material. The breaking of the pellets is due to the stress induced during absorption with an increase of 32% of the volume for the host Mg forming MgH₂.

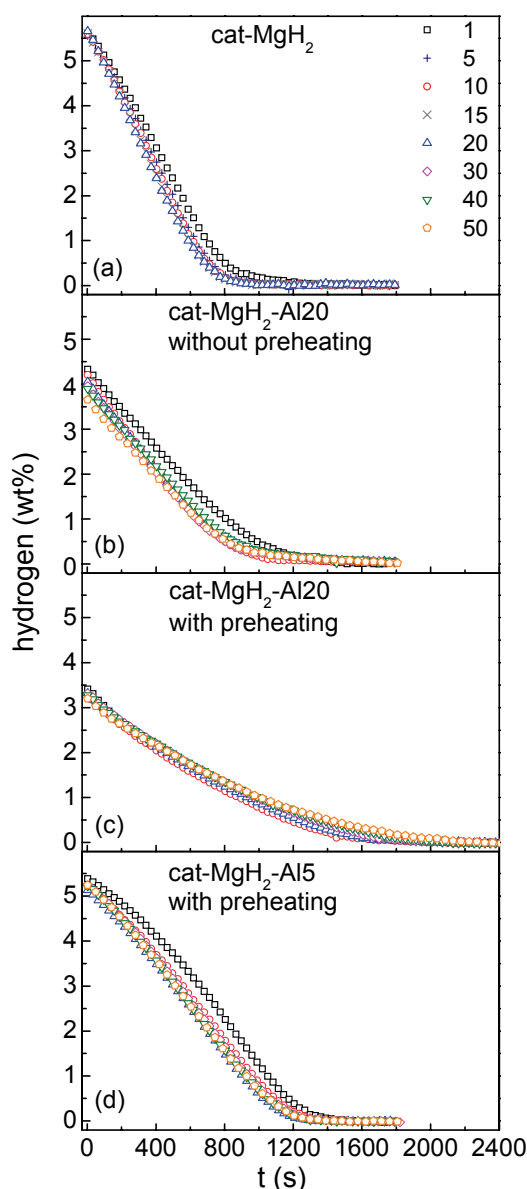


Figure 5.3 Desorption cycles performed at 320 °C and 1.2 atm H_2 of pellets cat-MgH₂ (a), cat-MgH₂-Al₂₀ without preheating (b), cat-MgH₂-Al₂₀ with preheating (c) and cat-MgH₂-Al₁₅ with preheating (d).

Figure 5.3b) gives the desorption curves for pellet cat-MgH₂-Al₂₀, where is shown that the time for 90% desorption is about 1020 s and the hydrogen content goes from the initial 4.3 wt% to about 3.6 wt% after 50 cycles. This decrease can be explained in terms of Mg-Al phases formation during cycling, slowly reacting with hydrogen due to a higher plateau pressure with respect to pure Mg. Moreover, it was observed that the compactness of the pellet started degrading before 20 cycles and was completely lost before 50 cycles. Another similar pellet was then first heated in vacuum at 450 °C, for 10 minutes, in order to facilitate, according the Mg-Al phase diagram [5.14], the formation of some intermetallic phases and/or solid solution and then submitted to 50 a/d cycles. As shown in figure 5.3c), the maximum hydrogen content of this pellet was about 3.3 wt% and the time for 90% desorption increased to 1320 s. The hydrogen content was now almost constant under cycling, in contrast to the pellet without pre-heating, and the degradation of mechanical compactness resulted less. However, the pellet started to degrade before about 50 cycles.

Cat-MgH₂-Al₅ pellets were cycled under similar conditions after pre-heating as in the previous case. Figure 5.3d) shows that in this case almost all the absorbed hydrogen (5.3 wt%) was released in about 1500 s. The desorption behaviour became almost stable just after 10 cycles and the pellet remained mechanically consistent and hard even after 50 cycles. Pictures of the cycled cat-MgH₂ and cat-MgH₂-Al₅ pellets are shown in figure 5.4. It is visible that the pellets not containing aluminium have a larger volume after 10 and 20 cycles compared to the pellets containing 5 wt% Al, due probably to a more advanced disgregation process of pellets without Al. After 50 a/d cycles, the pellet containing aluminium is still intact, while the one without aluminium got powdered.

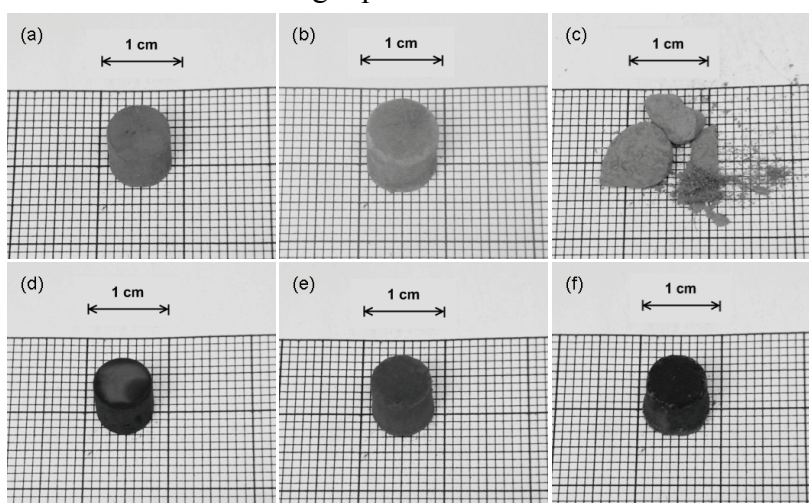


Figure 5.4 Pictures of the pellets after different cycles. (a), (b) and (c) are the pellets cat-MgH₂ after 10, 20 and 50 hydrogen a/d cycles, respectively, while (d), (e) and (f) are the pellets cat-MgH₂-Al₅ preheated at 450 °C after 10, 20 and 50 hydrogen a/d cycles, respectively.

5.4 Structural analysis and PCI of pellets

Figure 5.5 shows the XRD patterns of cat-MgH₂-Al5 and cat-MgH₂-Al20 hydrogenated and dehydrogenated pellets after heat treatment and 50 hydrogen a/d cycles. The relative abundance of the phases has been estimated by means of Rietveld refinement on the basis of the Al-Mg phase diagram [5.14] and is reported in table I.

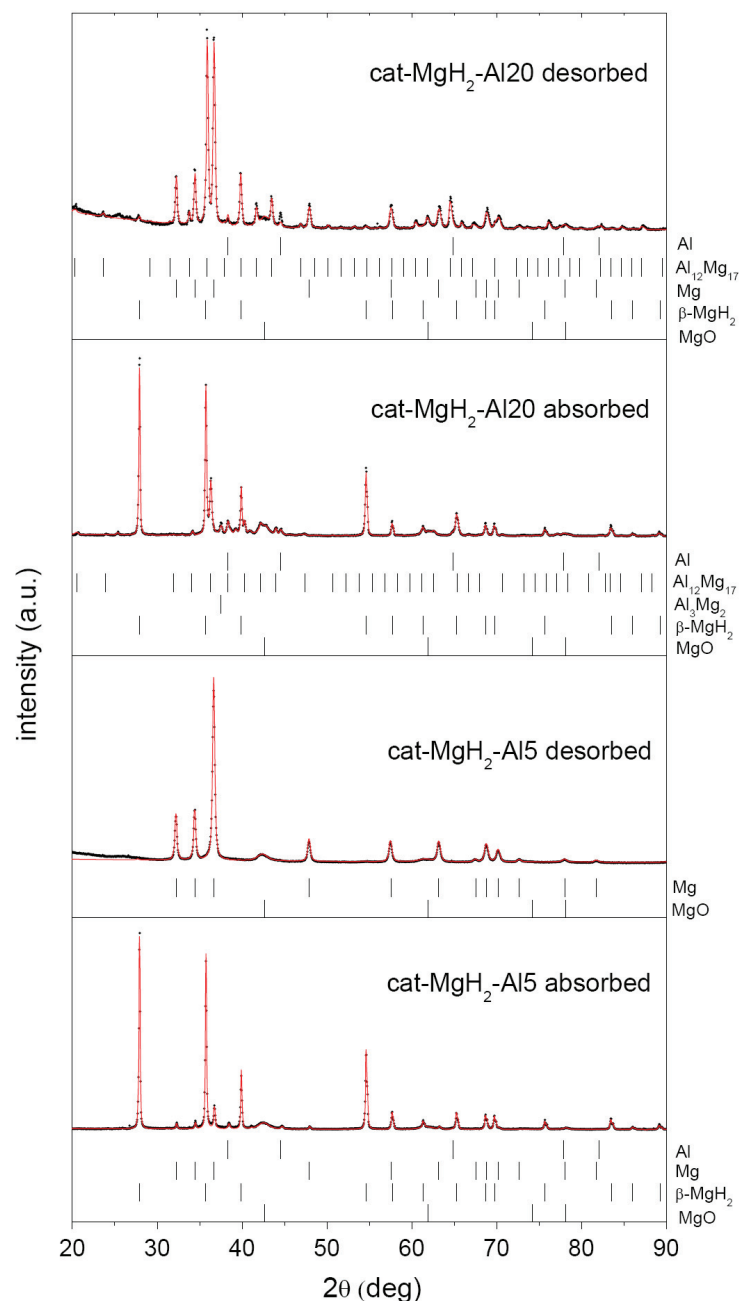


Figure 5.5 XRD patterns (black points) and Rietveld fit (red line) of preheated cat-MgH₂-Al20 and cat-MgH₂-Al5 pellets in the dehydrogenated and hydrogenated states after 50 hydrogen a/d cycles.

The cat-MgH₂-Al₂₀ sample displays the Mg phase (39 wt%), intense peaks of the intermetallic eutectic phase Al₁₂Mg₁₇ (43 wt%) and other residual phases as MgH₂, MgO plus a small amount of Al (<3 wt%). In the pattern of the cat-MgH₂-Al₂₀ sample hydrogenated after 50 a/d cycles, it is possible to notice the presence of Al₁₂Mg₁₇ phase (13 wt%) along with the Al₃Mg₂ phase (15 wt%) in addition to the obvious presence of MgH₂ (51 wt%). This agrees with the study of hydrogenation process of ball milled Mg-Al powders by Crivello et al. [5.15, 5.16], which occurs in two completely reversible steps:



Reaction (5.2) did not reach completion in our operating conditions, probably due to the higher relevant plateau pressure. The estimated amount of Al (4 wt%) in the cat-MgH₂-Al₂₀ hydrogenated sample is larger than in the case of dehydrogenated sample. This is due to the fact that a certain amount of Al is in solid solution in the structure of Mg and during hydrogenation is expelled, according to the disproportionation reaction [5.17]



Table 5.1 Quantitative analysis derived from the Rietveld refinement of the XRD patterns of the cycled pellets.

Sample	β -MgH ₂ (wt %)	Mg (wt%)	MgO (wt %)	Al (wt %)	Al ₃ Mg ₂ (wt %)	Al ₁₂ Mg ₁₇ (wt %)
cat-MgH ₂ -Al ₂₀ 450°C (des.)	<2	39 ± 2	14 ± 2	<3	-	43 ± 2
cat-MgH ₂ -Al ₂₀ 450°C (abs.)	51 ± 3		17 ± 2	4 ± 1	15 ± 2	13 ± 1
cat-MgH ₂ -Al ₅ 450°C(des.)	5 ± 1	73 ± 2	22 ± 1	-	-	-
cat-MgH ₂ -Al ₅ 450°C(abs.)	72 ± 1	7 ± 1	18 ± 1	<3	-	-

In the XRD pattern of cat-MgH₂-Al₅ dehydrogenated pellet, after heat treatment and 50 a/d cycles, there is no evidence of the presence of any Mg-Al intermetallic phase. According to the Mg-Al phase diagram, the smaller amount of Al is not sufficient for the precipitation of the eutectic phase and leads only to a solid solution of Al in Mg. The presence of Al in solid solution is also supported by the fact that the estimated amount of Al in the dehydrogenated sample is negligible. In the XRD profile of the same sample after hydrogenation there is no evidence of the presence of Mg-Al intermetallic phases. But, accordingly to the behaviour for the cat-MgH₂-Al₂₀ sample, the observed amount of Al (<3 wt%) is anyway more than in the dehydrogenated sample, in agreement with reaction (3). It is not possible to evaluate the actual amount of Al possibly incorporated into the residual Mg (7 wt%) and maybe into some intermetallic phases not detected by XRD.

The lattice parameters of Mg estimated by Rietveld refinement for some of the dehydrogenated samples are shown in figure 5.6. These values are smaller compared to those

of pure Mg (taken from PDF sheet 35-821) and this is certainly due to the presence of Al in Mg(Al) solid solution, considering the smaller metallic radius of Al compared to that of Mg [5.18]. The smallest lattice parameters are observed for the cat-MgH₂-Al5 sample after heat treatment and 50 a/d cycles, which shows that in this case Al prefers to form only a solid solution with Mg instead of forming Mg-Al intermetallic phases. On the contrary, in the case of the cat-MgH₂-Al20 samples the precipitation of the eutectic phase Al₁₂Mg₁₇ retards the complete formation of Mg(Al) and the lattice parameters are larger.

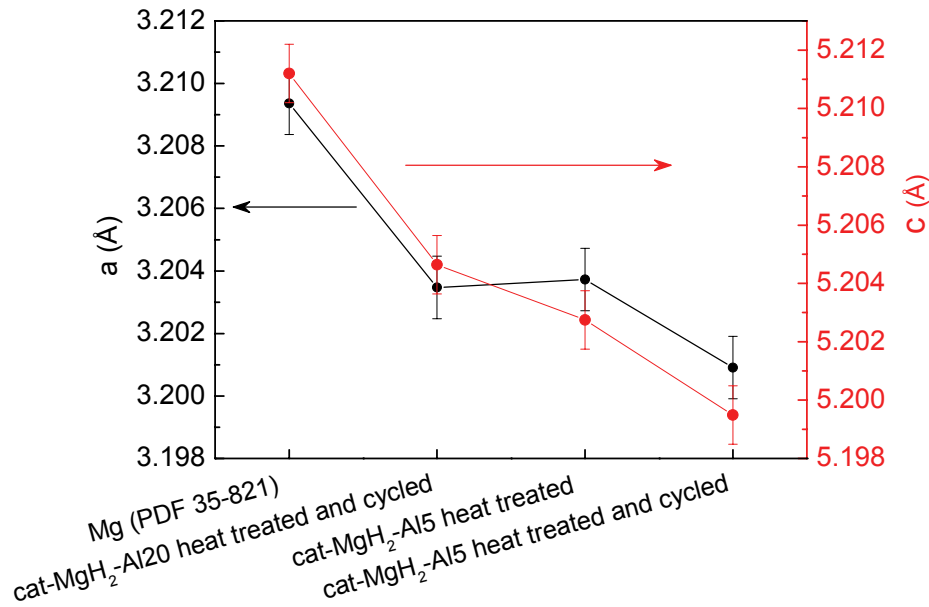


Figure 5.6 Lattice parameters of Mg estimated by Rietveld refinement for some of the studied dehydrogenated samples. The values are compared to the lattice parameters of pure Mg (PDF sheet 35-821).

PCI curves of the cat-MgH₂-Al5 pellet preheated at 450 °C are reported in figure 5.7, showing a single plateau in correspondence to the equilibrium pressure of pure MgH₂ phase at a given temperature. There is not a second plateau corresponding to the reaction of intermetallic phases with hydrogen, which would further justify the above discussion. Moreover, the values of the enthalpy (ΔH) and the entropy (ΔS) changes, as deduced from the van't Hoff plot (inset of figure 5.7), are -73 kJ/mol H₂ and -135 J/K·mol H₂, respectively, in good agreement with the values for pure MgH₂ phase [5.19].

The better mechanical resistance to a/d cycles of the dehydrogenated cat-MgH₂-Al5 samples with respect to the cat-MgH₂-Al20 samples are probably related to the presence in the first case of Al only in solid solution and, in the second case, of Al also in the Al₁₂Mg₁₇ intermetallic phase. This is supported by the following considerations. Solutioning of Al in Mg results in the strengthening of bulk polycrystalline materials because of the increase of the

critical resolved shear stress, i. e., the stress needed to start the slip of crystal planes along the basal plane [5.20].

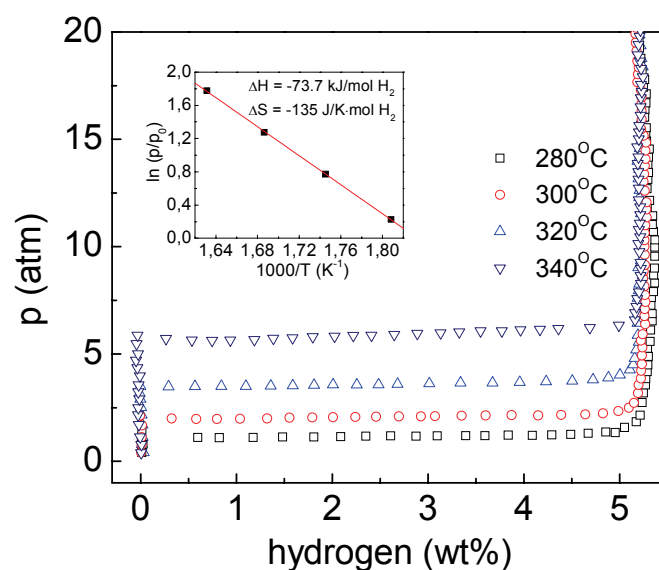


Figure 5.7 Lattice Pressure-composition-isotherms at different temperatures for the cat-MgH₂-Al₅ pellet preheated at 450 °C. The inset shows the corresponding van't Hoff plot.

However, at the same time the critical resolved shear stress for the prismatic slip is reduced, with improvement of ductility and then of the resistance of the material to fracture. In particular, the strengthening of Mg-Al alloys increases proportionally to the presence of Al up to 10 wt%, while the elongation (ductility) shows a maximum around 4 wt% Al [5.17]. The best compromise between hardness and ductility is estimated to be around 6 wt% Al. It has also been reported that the presence of Al in solid solution favours the superplasticity of Mg at temperatures >300 °C [5.21, 5.22], meaning that at these temperatures the material presents a high deformability before fracture. It should also be taken into account that the eutectic phase Al₁₂Mg₁₇, being very fragile, can cause a general embrittlement of the material. Therefore, the ductility of the material can be improved by reducing the amount of this phase [5.23], even in view of its localization along grain boundaries of the hosting Mg alloy [5.24]. Finally, since the bcc structure of Al₁₂Mg₁₇ is not compatible with the hcp structure of Mg, this leads to the embrittlement of the Mg/Al₁₂Mg₁₇ interface [5.25].

Figure 5.8 shows the results of the mechanical tests for hydrogenated pellets without Al and with 5 wt% Al after 0 and 50 a/d cycles. It is evident the better behaviour of pellets containing Al, while, in absence of aluminium, even a stress of 30.1 N/mm² is sufficient to break the pellet after 10 a/d cycles, decreasing to 8.1 N/mm² after 20 cycles. As said before and shown in figure 5.4, it is not possible to recover the pellet after 50 a/d cycles. The better behaviour of pellets containing 5 wt% Al can be attributed to the presence, according to reaction (5.3), of

an Al matrix surrounding the MgH_2 particles. Anyway, the strength decreases to 43.7 N/mm^2 and 13.9 N/mm^2 after 20 and 50 cycles, respectively, likely due to the progressive increase of porosity.

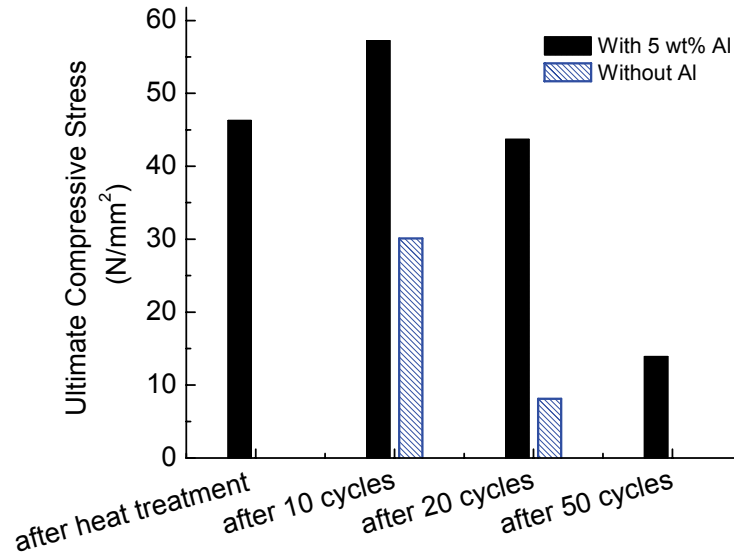


Figure 5.8 Results of the compression tests to estimate the mechanical strength of the pellets without and with 5 wt% Al.

Figure 5.9a) shows the SEM micrograph of the cat- MgH_2 -Al5 pellet after heat treatment at 450°C . The formation of aluminium connected matrix, used above to justify the improvement of mechanical properties of hydrogenated samples, is shown along with the grey spots, corresponding to MgH_2 and the white spots corresponding to well dispersed Nb_2O_5 particles. Figure 5.9b) gives the SEM pattern for the same pellet after 50 a/d cycles, showing that the cycling increases the homogeneity of the observed aluminium matrix and the MgH_2 phase.

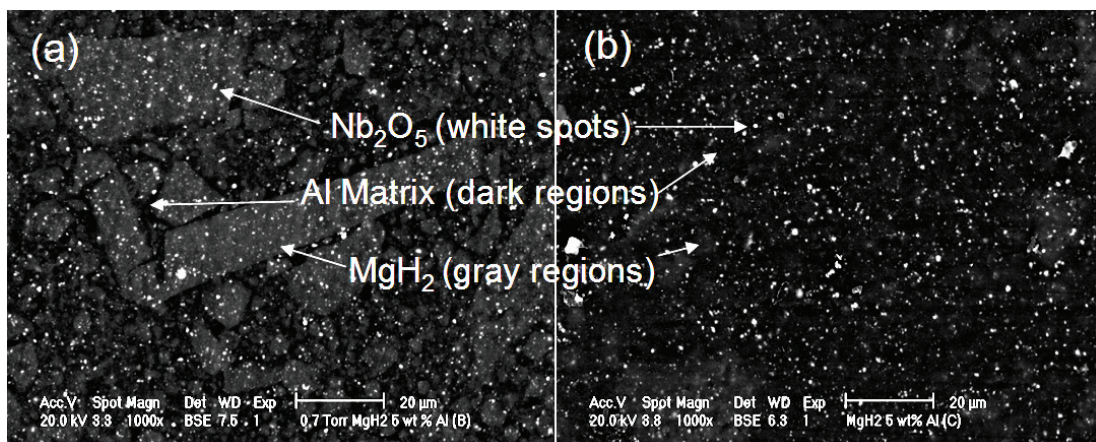


Figure 5.9 SEM micrographs for the cat- MgH_2 -Al5 pellet (a) preheated at 450°C and (b) after 50 hydrogen a/d cycles. The gray scale contrast of the above images is influenced by the presence of carbon in the starting powder mixture.

In conclusion, the mechanical strength of pellets made by catalysed MgH_2 mixed with crystalline aluminium powder as binding agent has been tested after hydrogen a/d cycles. It is found that a pre-heating treatment of the pellet to the temperature sufficient to form intermetallic phases and/or solid Mg-Al solutions ($450\text{ }^\circ\text{C}$) increases the resulting performance of the material, as concerns both functional and mechanical stability. The pellets with 20 wt% aluminium degrade by cycling and, moreover, the hydrogen content is low and decreases with the ongoing cycles. A good mechanical stability has been observed instead in the case of pellets with 5 wt% Al. These pellets show a constant 5.3 wt% hydrogen capacity up to 50 cycles and constant kinetics after 10 cycles. The enhanced stability of the pellets in this case has been attributed to the presence of the Al in solid solution with Mg.

The results reported in this chapter have been published in [5.26].

- [5.1] Dornheim M., Doppiu S., Barkhordarian G., Boesenberg U., Klassen T., Gutfleisch O., Bormann R., *Hydrogen storage in magnesium-based hydrides and hydride composites.*, Scripta Mater. (2007) **56**, 841.
- [5.2] Mushnikov N. V., Ermakov A. E., Uimin M. A., Gaviko V. S., Terent'ev P. B., Skripov A. V., Tankeev A. P., Soloninin A. V., Buzlukov A. L., *Kinetics of Interaction of Mg-based mechanically activated alloys with hydrogen.* Phys. Met. Metallogr. (2006) **102**, 421.
- [5.3] Gupta R., Agresti F., Lo Russo S., Maddalena A., Palade P., Principi G., *Structure and hydrogen storage properties of MgH₂ catalysed with La₂O₃.* J. Alloys Compd. (2008) **450**, 310.
- [5.4] Oelerich W., Klassen T., Bormann R., *Metal oxides as catalysts for improved hydrogen sorption in nanocrystalline Mg-based materials.* J. Alloys Compd. (2001) **315**, 237.
- [5.5] Polanski M., Bystrzycki J., Plocinski T., *The effect of milling conditions on microstructure and hydrogen absorption/desorption properties of magnesium hydride (MgH₂) without and with Cr₂O₃ nanoparticles.* Int. J. Hydrogen Energ. (2008) **33**, 1859.
- [5.6] Schulz R., Huot J., Liang G., Boily S., Lalande G., Denis M. C., Dodelet J. P., *Recent developments in the applications of nanocrystalline materials to hydrogen technologies.* Mater. Sci. Eng. A (1999) **267**, 240.
- [5.7] Zaluska A., Zaluski L., Ström-Olsen J. O., *Nanocrystalline magnesium for hydrogen storage.* J. Alloys Compd. (1999) **288**, 217.
- [5.8] Barkhordarian G., Klassen T., Bormann R., *Fast hydrogen sorption kinetics of nanocrystalline Mg using Nb₂O₅ as catalyst.* Scripta Mater. (2003) **49**, 213.
- [5.9] De Piccoli C., Dal Toé S., Lo Russo S., Maddalena A., Palade P., Saber A., Sartori S., Principi G., *Hydrogen storage in magnesium hydride doped with niobium pentaoxide and graphite.* Chem. Eng. Trans. (2004) **4**, 343.
- [5.10] Friedrichs O., Aguey-Zinsou F., Ares Fernández J. R., Sánchez-López J. C., Justo A., Klassen T., Bormann R., Fernández A., *MgH₂ with Nb₂O₅ as additive, for hydrogen storage: Chemical, structural and kinetic behavior with heating.* Acta Mater. (2006) **54**, 105.

- [5.11] Verga M., Armanasco F., Guardamagna C., Valli C., Bianchin A., Agresti F., Lo Russo S., Maddalena A., Principi G., *Scaling up effects of Mg hydride in a temperature and pressure-controlled hydrogen storage device*, Int J. Hydrogen Energ. (2009) **34**, 4602.
- [5.12] Glage A., Ceccato R., Lonardelli I., Girardi F., Agresti F., Principi G., Molinari A., Gialanella S., *A powder metallurgy approach for the production of a MgH₂-Al composite material*, J. Alloys Compd. (2009) **478** 273.
- [5.13] Chaise A., De Rango P., Marty Ph., Fruchart D., Miraglia S., Olivès R., Garrier S., *Enhancement of hydrogen sorption in magnesium hydride using expanded natural graphite*, Int. J. Hydrogen Energ. (2009) **34** 8589.
- [5.14] ASM Handbook, vol. 3, Alloy Phase Diagrams, ASM International; 1992. P. 305-6.
- [5.15] Crivello J. C., Nobuki T., Kato S., Abe M., Kuji T., *Hydrogen absorption properties of the γ -Mg₁₇Al₁₂ phase and its Al-rich domain*, J. Alloys Compd. (2007) **446**, 157.
- [5.16] Crivello J. C., Nobuki T., Kuji T., *Improvement of Mg-Al alloys for hydrogen storage applications*. Int J. Hydrogen Energ. (2009) **34**, 1937.
- [5.17] Andreasen A., *Hydrogenation properties of Mg-Al alloys*, Int. J. Hydrogen Energ. (2008) **33**, 7489.
- [5.18] Raynor G. V., *The Physical Metallurgy of Magnesium and Its Alloys*, New York: Pergamon Press; 1959 p. 73.
- [5.19] Sandia National Laboratories – Hydride Information Centre, available at: <http://hydpark.ca.sandia.gov/>
- [5.20] Caceres C. H., Rovera D. M., *Solid solution strengthening in concentrated Mg-Al alloys*, J. Light Metals (2001) **1**, 151.
- [5.21] Ceschini L., Balloni L., Boromei I., Mehtedi M. El, Morri A., *Superplastic behaviour of the AZ31 magnesium alloy produced by twin roll casting*. Met. Ital. (2007) **9**, 5.
- [5.22] Watanabe H., Tsutsui H., Mukai T., Kohzu M., Tanabe S., Higashi K., *Deformation mechanism in a coarse-grained Mg-Al-Zn alloy at elevated temperatures*. Int. J. Plasticity (2001) **17**, 387.

- [5.23] Kleiner S., Beffort O., Wahlen A., Uggowitzer P. J., *Microstructure and mechanical properties of squeeze cast and semi-solid cast Mg-Al alloys*. J. Light Metals (2002) **2**, 277.
- [5.24] Kostka A., Coelho R. S., Dos Santos J., Pyzalla A. R., *Microstructure of friction stir welding of aluminium alloy to magnesium alloy*, Scripta Mater. (2009) **60**, 953.
- [5.25] Zhang L., Cao Z. Y., Liu Y. B., Su G. H., Cheng L. R., *Effect of Al content on the microstructure and mechanical properties of Mg-Al alloys*. Mater. Sci. Eng. A (2009) **508**, 129.
- [5.26] Khandelwal A., Agresti F., Capurso G., Lo Russo S., Maddalena A., Gialanella S., Principi G., *Pellets of MgH₂-based composites as practical material for solid state hydrogen storage*, Int. J. Hydrogen Energ. (in press).

Chapter 6

Effect of high energy ball milling on the hydrogen storage properties of Li-Mg-N-H system

6.1 The Li-Mg-N-H system

In section 2.4.3 it has been seen that the Li-Mg-N-H system, obtained by milling and activating a $2\text{LiNH}_2 + \text{MgH}_2$ mixture, due to the favourable thermodynamics, presents a high desorption plateau pressure at the operating temperature slightly above $200\text{ }^\circ\text{C}$, with a theoretical hydrogen capacity of 5.6 wt%. The system is activated according the reaction:



and works reversibly according the reaction:



In figure 6.1 typical PCI curves obtained during hydrogen desorption are shown.

Up to now the absorption kinetics of this system has not been studied in detail and a study to relate the milling time of the mixture with the rate of hydrogen a/d is not yet available. Aim of the work presented in this chapter is to test the effectiveness of the presence of additives and of a prolonged milling time in improving the kinetics of hydrogen a/d processes.

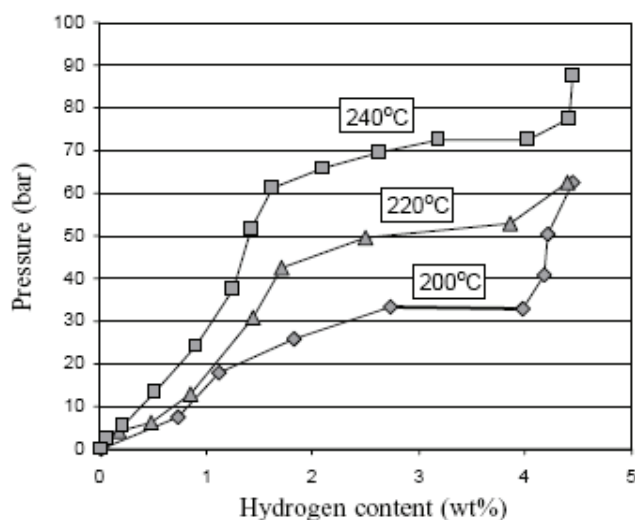


Figure 6.1 PCI curves during hydrogen desorption corresponding to the equilibrium $Mg(NH_2)_2 + 2LiH \rightleftharpoons Li_2Mg(NH)_2 + 2H_2$ [6.1]

6.2 Preparation of samples

In this work samples of 2.5 g were obtained mixing powders of $LiNH_2$ (Sigma Aldrich, 95 % purity) and MgH_2 (Th. Goldschmidt GmbH, 95% MgH_2 + 5% Mg) in the stoichiometric ratio 2:1.1. The samples were ball milled in argon atmosphere using stainless steel spheres with a ball to powder ratio of 10:1. The milling times were 2h, 12h, 24h and 48h and every sample was labelled accordingly. The milling process was carried out alternating 5 min of milling and 5 min of stop in order to avoid an excessive heating of the powders inside the vial. All the procedure of the powder handling before and after milling were carried out inside a glove box in argon atmosphere.

The thermodynamic and kinetic properties of hydrogen storage of samples were measured by means of Sievert's volumetric apparatus.

The microstructure of the samples was analysed by means of Rietveld refinement of X-ray diffraction patterns. The XRD measurements were carried out on samples prepared into the glove box by protecting them with a thin kapton film (8 μm). The diffraction peaks originated by kapton film are within $10-20^\circ 2\theta$, far from the sample region of interest.

The milled samples were activated by means of a 18-20 h heat treatment at 220-230 $^\circ C$ in hydrogen high pressure (11-12 MPa), following the procedure suggested by Yang et al. [6.2].

6.3 Structure of milled, activated and cycled samples

The XRD patterns of 2h, 12h, 24h and 48h as milled samples are shown in figure 6.2. The crystallite size, as obtained from Rietveld analysis of all samples, is reported in Table 1 for all recognised phases, except for metallic Mg and MgO, present in a too small amount for quantitative determinations.

After a milling time of 2 h is possible to recognize two main phases: LiNH_2 , $\beta\text{-MgH}_2$ and a small amount of metastable $\gamma\text{-MgH}_2$ and metallic Mg. Metallic Mg is already present in the provided commercial MgH_2 and probably derives also from the partial decomposition of the hydride during the milling process. The average crystallite size is less than 25 nm for $\beta\text{-MgH}_2$ and $\gamma\text{-MgH}_2$ and less than 35 nm for LiNH_2 .

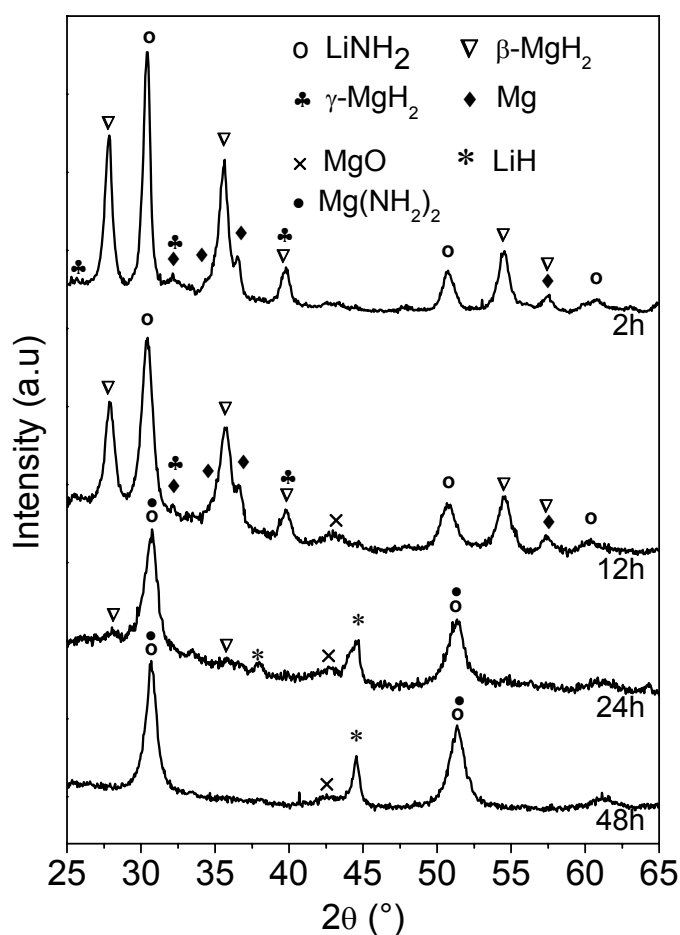


Figure 6.2 XRD patterns of $2\text{LiNH}_2+1.1\text{MgH}_2$ samples milled for the indicated times.

The XRD patterns of 2h and 12h as milled samples are similar, as can be seen in figure 6.2, meaning that the phases within the two samples are the same, and differ only in the peak broadening due to the smaller crystallite size of 12h sample. This is quantitatively confirmed

by the results of Rietveld analysis reported in Table 1: after milling for 12 h the average crystallite size is less than 25 nm for all the phases. Particularly for LiNH_2 and $\beta\text{-MgH}_2$ the average crystallite size decreases more than 40% with respect to 2h sample.

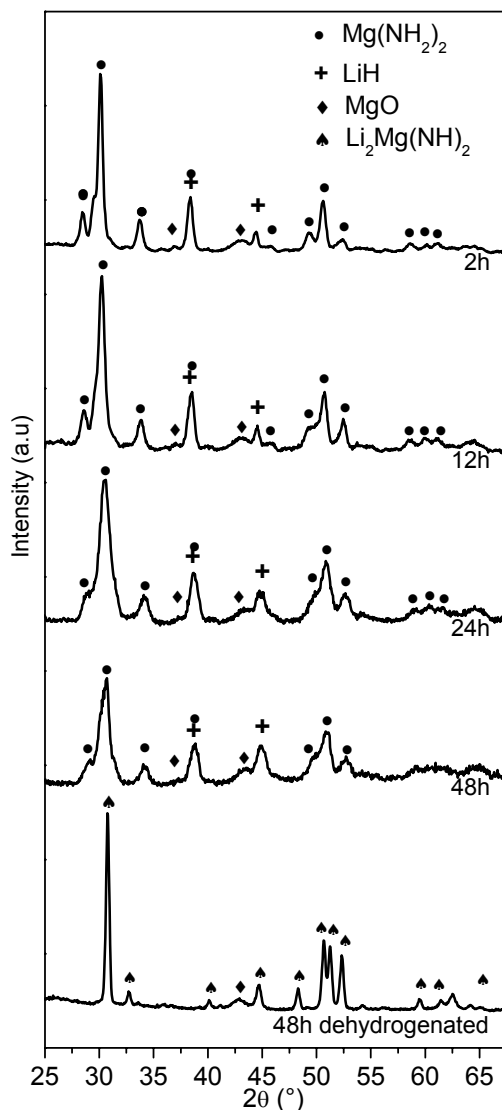


Figure 6.3 XRD patterns of rehydrogenated samples; for comparison also the pattern of 48 h milled dehydrogenated sample is reported.

When the milling time exceeds 12 h, the characteristic peaks related to $\beta\text{-MgH}_2$ and $\gamma\text{-MgH}_2$ disappear, while those of the LiNH_2 remain and the peaks related to LiH appear. This suggests that a certain quantity of the starting mixture has reacted to form $\text{Mg}(\text{NH}_2)_2$ and LiH according to reaction (6.1). Anyway, it is difficult to establish the real presence of $\text{Mg}(\text{NH}_2)_2$, because the peaks of this phase are overlapped with those of LiNH_2 . However, the Rietveld refinement worked better including this phase in the calculation. The presence of $\text{Mg}(\text{NH}_2)_2$ and LiH can be justified by the fact that during milling the local temperature of the powders could raise remarkably. The fact that the peaks related to LiNH_2 are still present in the XRD

pattern suggests that also β -MgH₂ must be present in the sample, even if the characteristic peaks are not observable.

A possible explanation is a crystal degradation together with a very fine dispersion of the remaining MgH₂ into the 24h and 48h samples due to the prolonged milling time. A small amount of MgO (less than 1-2 vol%) can be observed in the XRD patterns of 24h and 48h milled samples, probably due to oxidation of Mg during milling by traces of oxygen inside the vial. LiNH₂ is the only phase displayed in all the XRD patterns of as milled samples and it is possible to notice from Table 1 that the average crystallite size decreases by increasing milling time.

Table 6.1 Results of Rietveld analysis of studied samples.

Sample	As milled		Rehydrogenated	
	Phases	Crystallite size (nm)	Phases	Crystallite size (nm)
Milled 2h	LiNH ₂ tetragonal	31 ± 4	Mg(NH ₂) ₂ tetragonal	38 ± 4
	β -MgH ₂ tetragonal	22 ± 3	LiH cubic	130 ± 10
	γ -MgH ₂ orthorombic	15 ± 4	MgO cubic	/
	Mg hexagonal	/		
Milled 12h	LiNH ₂ tetragonal	18 ± 3	Mg(NH ₂) ₂ tetragonal	30 ± 5
	β -MgH ₂ tetragonal	13 ± 2	LiH cubic	110 ± 15
	γ -MgH ₂ orthorombic	23 ± 5	MgO cubic	/
	Mg hexagonal	/		
	MgO cubic	/		
Milled 24h	LiH cubic	70 ± 15	Mg(NH ₂) ₂ tetragonal	16 ± 2
	LiNH ₂ tetragonal	17 ± 3	LiH cubic	110 ± 10
	Mg(NH ₂) ₂ tetragonal	20 ± 7	MgO cubic	/
	MgO cubic	/		
Milled 48h	LiH cubic	80 ± 20	Mg(NH ₂) ₂ tetragonal	15 ± 2
	LiNH ₂ tetragonal	15 ± 3	LiH cubic	60 ± 7
	Mg(NH ₂) ₂ tetragonal	15 ± 6	MgO cubic	/
	MgO cubic	/		

The XRD patterns of rehydrogenated samples are shown in figure 6.3. The phases present in these samples are Mg(NH₂)₂ and a small amount of MgO. Also in this case (see table 1) it is possible to note that the average crystallite size of Mg(NH₂)₂ and LiH decreases with milling time. Moreover, in 2h, 12h and 24h samples the average crystallite size of LiH is quite larger compared to Mg(NH₂)₂, while in 48h sample they are close. In particular, the crystallite size related to Mg(NH₂)₂ decreases by more than 50% going from 2h-12h samples to 24h-48h samples. Concerning LiH, the crystallite size decreases remarkably only after 48 h of milling. The XRD pattern related to 48h milled dehydrogenated sample is shown in figure 6.3 and is very similar to that reported in the literature [6.2, 6.3, 6.4]. The dehydrogenated material is

composed essentially by a mixed Li and Mg imide ($\text{Li}_2\text{Mg}(\text{NH})_2$), whose structure has been recently resolved by Rijssenbeek et al. [6.4] by means of neutron diffraction. The crystal structure of this phase belongs to the orthorhombic system at room temperature and can be described as a supercell of the high temperature cubic form of Li_2NH . The Li and Mg atoms are randomly distributed over two crystallographic sites, (4b) and (8c). The Rietveld analysis of the XRD profile carried out using the structure suggested by Rijssenbeek et al. [6.4] (space group Iba2) gave the following cell parameters:

$$a = (9.781 \pm 0.003) \text{ \AA}$$

$$b = (4.990 \pm 0.003) \text{ \AA}$$

$$c = (5.195 \pm 0.003) \text{ \AA},$$

in agreement with their results.

6.3 Hydrogen a/d kinetics and thermodynamics

The a/d kinetics has been studied at 220 °C for all samples in order to investigate the effect of milling time. It has been found that none of the additive tested has a significant effect on the kinetics, then only the results obtained with samples free of additives are shown in the following. In figure 6.4 the absorption kinetics at 220 °C and a starting hydrogen pressure of 9 MPa is shown for all samples. Sample milled 48 h displays the maximum measured hydrogen capacity, 4.7 wt.%.

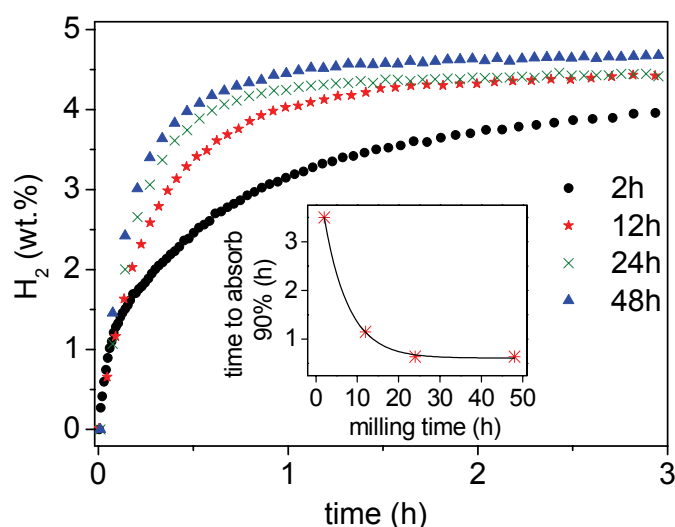


Figure 6.4 Absorption kinetics of 2h, 12h, 24h, 48h samples at 220°C and 9 MPa of H_2 . The inset shows the time to absorb 90% of total hydrogen capacity vs. milling time.

It is possible to observe that the hydrogen absorption kinetics of studied samples is improved by increasing the milling time. While 60 min and more than 3 hours are necessary to 12h e 2h samples, respectively, in order to absorb 4.0 wt.% of H₂ (about 85% of the maximum hydrogen capacity), 24h sample needs 40 min in order to absorb the same amount. Samples milled for 24 h and 48 h have, approximately, the same kinetics: the small difference is due to the higher hydrogen capacity of 48h sample (4.7 wt.% H₂ against 4.5).

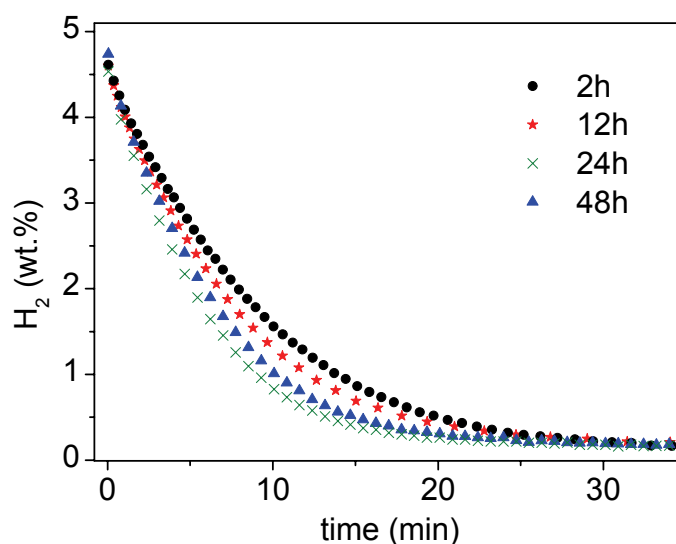


Figure 6.5 Desorption kinetics of 2h, 12h, 24h, 48h samples at 220°C and 0.25 MPa of H₂.

Desorption kinetics, shown in figure 6.5 results considerably faster than absorption and less sensitive to milling time: faster for 12h sample than for 2h sample, while for 24h and 48h samples is almost the same.

Chen et al. [6.5] reported that the reversibility of this system is dominated by a local interaction between Mg(NH₂)₂ and LiH. The samples milled for a longer time (24 h and 48 h) are characterized by lower crystallite size and more homogeneous inter-dispersion of the phases; this assures a higher contact surface by which Mg(NH₂)₂ and LiH can interact. The higher capacity of 48h sample should be justified by a finer and homogeneous dispersion of MgH₂ inside the starting mixture. This fact assures that MgH₂ is closely in contact with LiNH₂ during the activation reaction, in order to convert a greater quantity of material according to reaction (6.1).

The better desorption kinetics of 24h and 48h samples can be directly connected to the average crystallite size of Mg(NH₂)₂ and LiH hydrogenated phases, that are remarkably smaller in comparison with 2h and 12h samples: in particular, the decrease is more than 50% for Mg(NH₂)₂. A smaller crystallite size reduces the average diffusion paths of hydrogen during desorption.

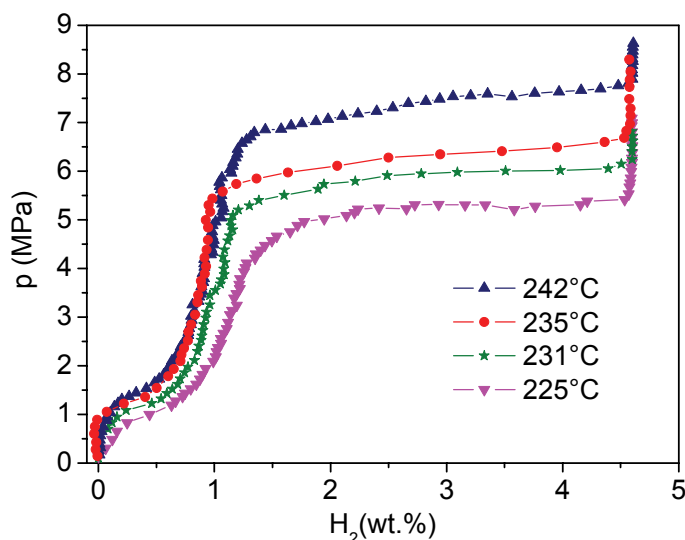


Figure 6.6 Desorption pressure composition isotherms at 225, 231, 235 e 242 °C for 12h sample.

This peculiarity of hydrogenated state ($\text{Mg}(\text{NH}_2)_2$ and LiH) probably leads, after the release of hydrogen, to the nucleation of a dehydrogenated phase characterized by a microstructure that enhances the absorption kinetics. Moreover, a prolonged milling leads to a higher concentration of structural defects that can represent preferential nucleation sites characterized by lower activation energy for the hydrogenated phases.

The thermodynamic characterisation of the system has been carried out measuring pressure-composition isotherms (PCI) at 225, 231, 235 and 242 °C for 12h sample (see figure 6.6), showing a reversible capacity of 4.6 wt.% H_2 , according to the kinetics measurements. The isotherms exhibit two plateaus which may correspond, in agreement with Luo et al. [6.3], to the following reactions:



From the PCI plateau pressures and the corresponding temperatures a van't Hoff plot of figure 6.7 has been built up in order to evaluate the reaction desorption enthalpy, which results to be 40.4 kJ/mol H_2 , in agreement with the literature data [6.1, 6.2, 6.6, 6.7].

It can be concluded that for the studied system a milling time of 24h (or longer) gives a better kinetics compared to 2h and 12h milled samples, the improvement being higher in absorption mode, where the system shows worse kinetics than desorption. The sample milled for 48 h shows an higher hydrogen capacity with respect to the other samples. In this case, the prolonged milling leads to a reciprocal better dispersion of LiNH_2 and MgH_2 which leads to a more efficient activation of the material. The kinetics improvement is due to the reduced average crystallite size, which gives rise to increase of surface to bulk ratio, enhancing the solid-solid reactivity and shortening the hydrogen diffusion paths.

The results reported in this chapter have been published in [6.8].

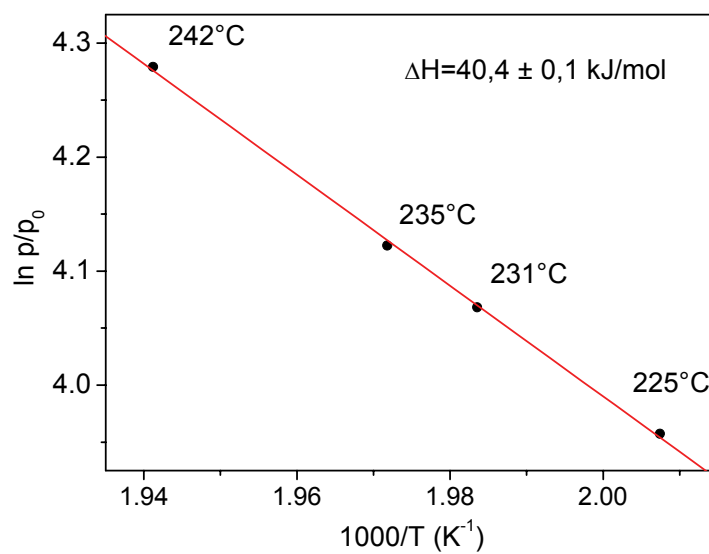


Figure 6.7 Van't Hoff plot for the Li-Mg-N-H system.

- [6.1] Luo W., (*LiNH₂-MgH₂*): a viable hydrogen storage system, *J. Alloys Compd.* (2004) **381**, 284.
- [6.2] Yang J., Sudik A., Wolverton C., *Activation of hydrogen storage materials in the Li-Mg-N-H system: Effect on storage properties*, *J. Alloys Compd.* (2006) **430**, 334.
- [6.3] Luo W., Sickafoose S., *Thermodynamic and structural characterization of the Mg-Li-N-H hydrogen storage system*, *J. Alloys Compd.* (2006) **407**, 274.
- [6.4] Rijssenbeek J., Gao Y., Hanson J., Huang Q., Jones C., Toby B., *Crystal structure determination and reaction pathway of amide-hydride mixtures*, *J. Alloys Compd.* (2008) **454**, 233.
- [6.5] Chen Y., Wu C. Z., Wang P., Cheng H. M., *Structure and hydrogen storage property of ball-milled LiNH₂/MgH₂ mixture*, *Int. J. Hydrogen Energ.* (2006) **31**, 1236.
- [6.6] Xiong Z., Hu J., Wu G., Chen P., Luo W., Gross K., Wang J., *Thermodynamic and kinetic investigations of the hydrogen storage in the Li-Mg-N-H system*, *J. Alloys Compd.* (2005) **398**, 235.
- [6.7] Luo W., Rönnebro E., *Towards a viable hydrogen storage system for transportation application*, *J. Alloys Compd.* (2005) **404-406**, 392.
- [6.8] Barison S., Agresti F., Lo Russo S., Maddalena A., Palade P., Principi G., Torzo G., *A study of the LiNH₂-MgH₂ system for solid state hydrogen storage*, *J. Alloys Compd.* (2008) **459**, 343.

Chapter 7

Mechano-chemical direct synthesis of LiBH₄ and improvement of decomposition kinetics

7.1 LiBH₄, an intensively studied complex hydride

LiBH₄ is known as one of the most used compounds in organic chemistry as reducing agent for aldehydes, ketones, acid chlorides, lactones, epoxides, esters [7.1]. LiBH₄ is also known as one of the best energy density carriers. In fact, it is one of the most interesting and studied complex hydrides for hydrogen storage, due to its high theoretical gravimetric hydrogen capacity (18.4 wt%). It can be industrially prepared by metathesis reaction starting from NaBH₄ and Li halides or chlorides [7.2, 7.3]. Recently, LiBH₄ has been directly synthesized from a mixture of elements exposed to hydrogen at 700 °C and 150 bar [7.4]. LiBH₄ starts decomposing above 300 °C according the following reaction:



having a maximum desorption rate between 400 °C and 500 °C and releasing 13.4 wt% H₂. Not all the theoretical hydrogen content can be easily released, due to the high stability of LiH since it desorbs hydrogen only above 730 °C [7.5]. In figure 7.1(a) typical TPD measurements obtained at different heating rates are shown, while figure 7.1(b) gives a schematic enthalpy diagram showing the transformations occurring during LiBH₄ decomposition. Besides the high dehydrogenation temperature, the problem of using LiBH₄ as a hydrogen storage material is the complexity of the recycling mechanism: as reported by Orimo et al. [7.6],

reaction (7.1) is reversible only in extreme pressure and temperature conditions (350 bar H_2 and 600 °C).

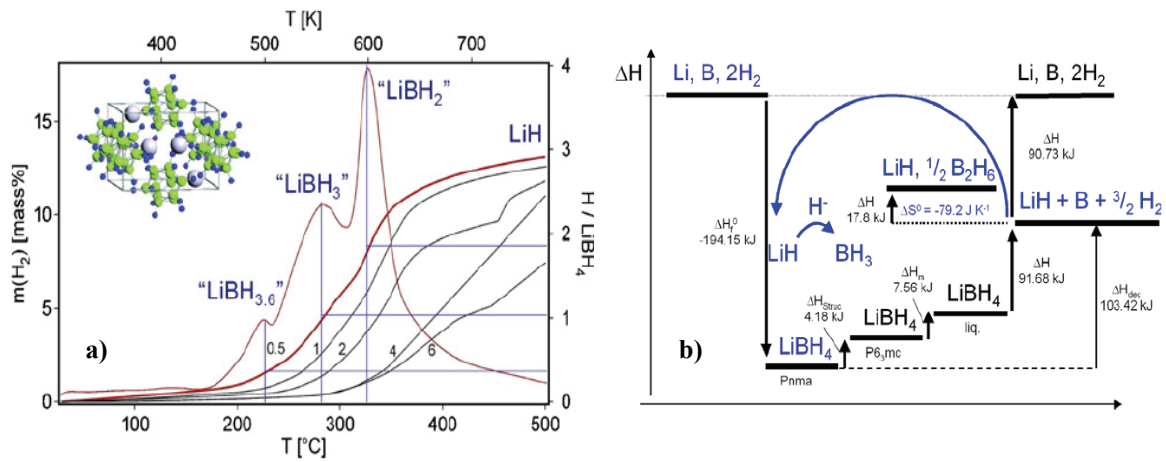


Figure 7.1 TPD measurements at different heating rates during the dehydrogenation of $LiBH_4$ (a) and schematic enthalpy diagram of transformations during the process (b) [7.5].

In this chapter two approaches are proposed with the aim of facing the mentioned problems that limit the possibility of using $LiBH_4$ as a practical hydrogen storage system. The first approach is related to the problem of reversibility of reaction (7.1): the possibility of obtaining $LiBH_4$ through a direct mechano-chemical synthesis starting from the decomposition products of reaction is shown.

The second approach is related to the high decomposition temperature of the same reaction. In order to improve thermodynamics and kinetics of dehydrogenation of light metal hydrides, Vajo et al. [7.7] have proposed to confine them in nanoporous scaffolds, exploiting the favourable properties of nanostructured materials and avoiding sintering and agglomeration during cycling. In recent papers it has been shown that $LiBH_4$ milled with carbon nanotubes [7.8] and included in mesoporous carbon [7.9] displays a decrease of dehydrogenation temperature. Beneficial effects of carbon addition on the dehydrogenation kinetics have also been observed for the Li-B-Mg-H system [7.10]. In section 7.3 it is shown that $LiBH_4$ deposited on MWCNTs previously modified by ball milling exhibits a lower dehydrogenation temperature compared to the pure material. It is also shown that, even if the thermodynamics remains unchanged with respect to the pure $LiBH_4$, the dehydrogenation temperature is lower when the specific surface area (SSA) of the support is larger. This improvement may be correlated to a heterogeneous nucleation process of the solid decomposition products of reaction (1) on the surface of carbon.

7.2 Direct mechanochemical synthesis of LiBH_4

7.2.1 Preparation of samples

Samples of 1.0 g were obtained by mixing LiH powder (Sigma–Aldrich, 95% purity) and small (less than 1 cm size) B pieces (Sigma–Aldrich, >99% purity) in the stoichiometric ratio 1:1. Boron in pieces is used to reduce the natural passivating oxide layer that could reduce reactivity. The samples were processed in hydrogen atmosphere by high energy ball milling with a SPEX 8000M mill in a stainless steel vial using stainless steel and WC balls (ball to mixture ratio of 30:1). Five different samples were prepared: samples A, B, C, D by ball milling with stainless steel balls in 3 atm H_2 for 12 h, 3 atm H_2 for 30 h, 4.5 atm H_2 for 120 h and 10 atm H_2 for 138 h, respectively; sample E was milled using WC balls in 10 atm H_2 for 138 h. A slight pressure drop in the vial was observed during milling, so it was periodically refilled by hydrogen in order to reproduce the desired overpressure.

One g of milled sample E was put in 70 ml of methyl *tert*-butyl ether, in which LiBH_4 is soluble, and stirred for 12 h under argon atmosphere. Methyl *tert*-butyl ether was used due to its much lower tendency to form explosive organic peroxides with respect to other ethers like THF and moreover, it is not forming adducts with LiBH_4 . The suspension was then filtered and the obtained solution was evaporated under dynamic rotary pump vacuum. After the complete evaporation of solvent a white crystalline light powder was obtained.

7.2.2 dehydrogenation profiles of as milled samples

Thermal Programmed Desorption (TPD) measurements were performed on milled samples by means of a Sievert's volumetric apparatus. Before the measurements, the sample chamber was evacuated at room temperature. The temperature was then changed from ambient to 507 °C at a heating rate of 2.5 °C/min.

In figure 7.2 the TPD of all studied samples are shown. Under the assumption that only hydrogen is desorbed from them, sample A starts desorbing H_2 at around 300 °C with the maximum rate at around 460 °C, while samples B, C, D, E start desorbing at temperatures slightly higher than RT (about 80 °C). The maximum desorption rate is around 255 °C, 347°C, 335°C and 364 °C for sample B, C, D and E, respectively. It is evident that the desorbed H_2 increases with increasing time of milling and hydrogen pressure inside the vial. Moreover, it is higher in case of WC balls used instead of stainless steel balls. In particular, sample E desorbs about 3 wt% H_2 .

This hydrogen desorption may be due to a new phase formed during ball milling, since LiH, the only starting phase containing hydrogen, desorbs hydrogen only above 730 °C [7.5]. As an alternative explanation, B could destabilize LiH producing a Li-B compound and H_2 at a temperature lower than that of LiH decomposition. A similar mechanism has been already reported by Vajo [7.11] for a LiH/Si mixture

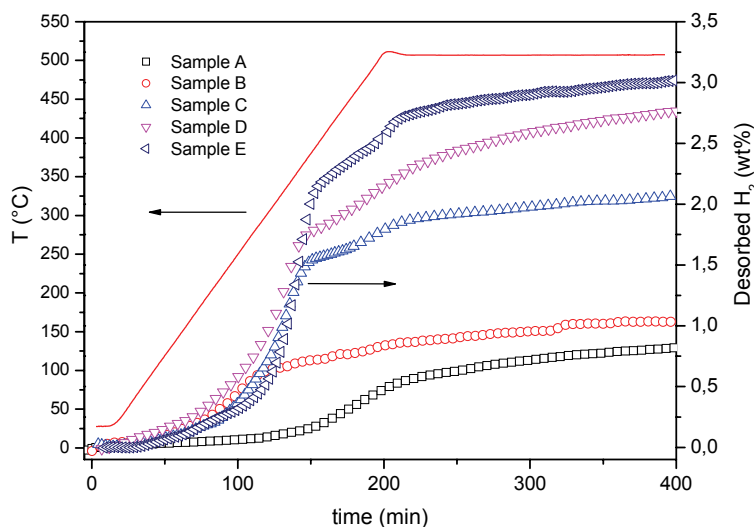


Figure 7.2 Comparison of dehydrogenation profiles of samples A, B, C, D and E.

7.2.3 Structure and thermodynamics of synthesised samples

The XRD measurements were carried out on samples handled into a MBraun glove box equipped with gas purification system (less than 1ppm humidity, 1 ppm O₂) by protecting them with a thin kapton foil (8 μm).

In figure 7.3 the XRD patterns of sample E before and after desorption are shown. The two patterns are similar, apart from the peak intensities, that are low for the as milled sample which is almost completely amorphous due to the treatment. The main peaks are related to LiH and to WC, the latter being a contaminant coming from the balls due to the high hardness of boron and having high peak intensities due to the high atomic weight of W. However, quantitative analysis of the profiles shows that the amount of WC is less than 0.05 % by volume. No peaks related to B are visible in both patterns due its tendency to amorphization [7.12, 7.13]. Moreover, peaks that could be related to Li-B compounds are not present in the pattern of desorbed sample, hence the desorbed hydrogen should reasonably come from an amorphous hydrogenated phase like LiBH₄ formed during the reactive milling.

Differential scanning calorimetry (DSC) measurements were performed using a TA Instrument DSC Q200, under Ar at a heating rate of 10 °C/min from 23 °C to 300 °C.

The DSC profile taken for the as milled sample E, shown in figure 7.4 (a), resembles that of LiBH₄ reported in the literature [7.6]. The peak at 114 °C, quite broad probably due to the initial amorphous-like state, should be due to the transition to hexagonal phase and the one at 254 °C should be due to melting of LiBH₄.

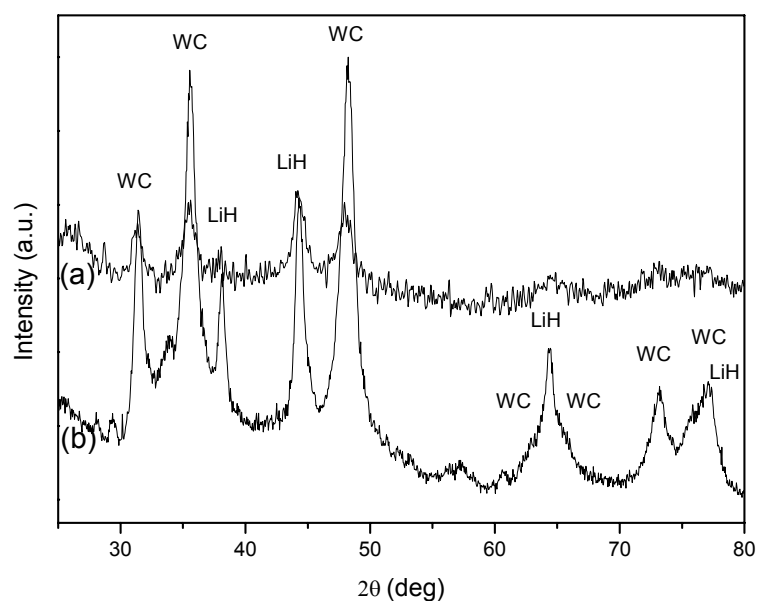


Figure 7.3 XRD patterns of sample E in the as milled (a) and dehydrogenated (b) states.

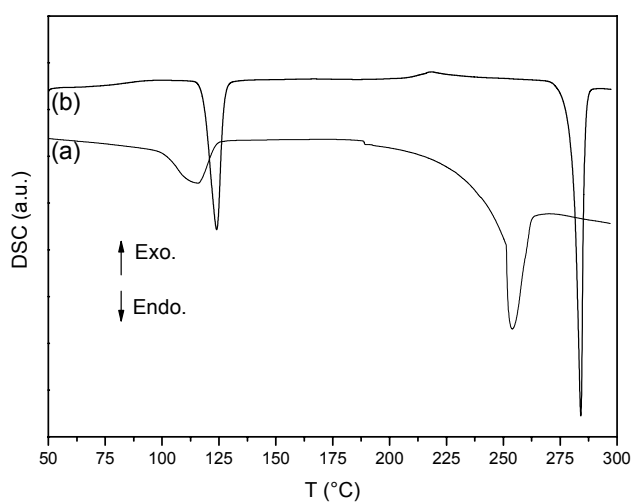


Figure 7.4 Comparison of DSC profiles of as milled (a) and solvent separated (b) sample E.

A shoulder starts from 188 °C, probably due to hydrogen desorption, confirming the results shown in figure 7.2. This shoulder starts at a temperature much lower than that reported for the TPD of pure LiBH_4 , which shows two desorption peaks: the first, small, between 300 °C and 400 °C and the main between 400 °C and 500 °C [7.14]. This effect may be due to several reasons, as the presence of the decomposition products, LiH and B, acting as “seeds” for decomposition, or the amorphous like state of LiBH_4 or maybe its nanostructured nature.

In figure 7.5 the XRD pattern of the powder obtained by solvent separation is shown together that of the kapton foil that can be subtracted. All peaks not due to kapton foil belong to orthorhombic low temperature LiBH₄.

To confirm this structural result, in figure 7.4(b) is shown the DSC profile of the crystallized powder, which results very similar to that reported by Orimo [7.6] for pure LiBH₄, with phase transition and melting temperature at 124 °C and 284 °C, respectively. The peaks are sharper than in figure 7.4(a) due to the increased crystallinity and shifted towards higher temperatures with respect to the as milled powder. No shoulders due to decomposition are visible up to 300 °C.

In figure 7.6 the TPD of crystallized LiBH₄ is shown, together with an inset plotting the desorption rate vs. temperature. The desorption rate has two maxima, the less intense at 309 °C and the most intense at 442 °C. The desorbed hydrogen is about 11 wt%. This results are in agreement with literature data for pure LiBH₄ decomposition [7.14].

The mechanism proposed here for the formation of LiBH₄ during the ball milling process proceeds through the reaction of B with H₂ to give diborane according the following reaction:

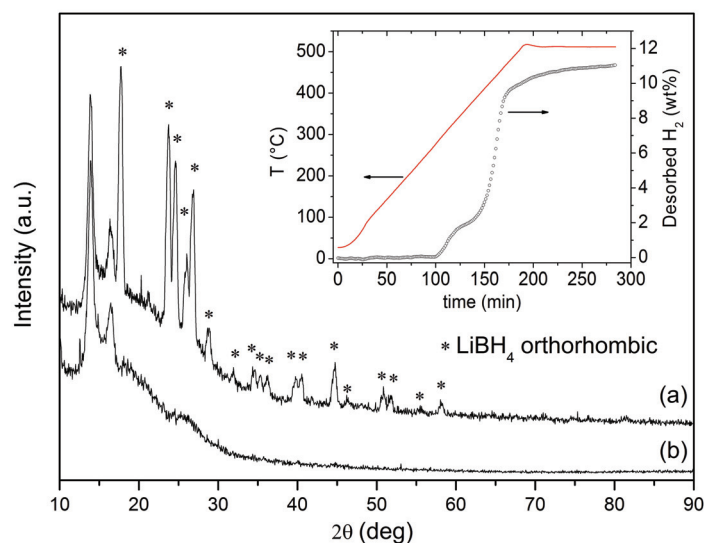
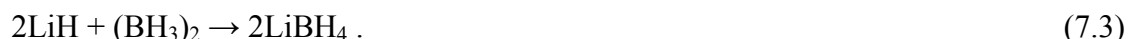


Figure 7.5 Comparison of the XRD patterns of solvent separated sample E (a) and kapton foil (b). The inset shows the dehydrogenation profile of same sample.

The latter reaction is endothermic ($\Delta H^0=35.6$ kJ/mol H₂, $\Delta S^0=-79.2$ J/K·mol H₂) [7.15], hence it proceeds only at high temperature and pressure (reaction driven by entropy) [7.16]. Being the high energy ball milling a non-equilibrium technique that in many cases easily allows to obtain metastable phases and mechano-chemical reactions not thermodynamically possible at ambient conditions, it is reasonable to think that the reported reaction can occur

even if the system is globally far from the equilibrium conditions. The diborane formed during the reaction could then react with LiH leading to the corresponding borohydride:



The reaction is already known to occur for the synthesis of other borohydrides like NaBH_4 [7.17].

The results presented in this section have been published in [7.18]

7.3 Improvement of dehydrogenation kinetics of LiBH_4 dispersed on modified multi-walled carbon nanotubes

7.3.1 Preparation of samples

Commercial MWCNTs, provided by CNT Co., Ltd. (Korea), were modified by high energy ball milling in order to increase the SSA. A ball to powder ratio of 10:1 has been used. The modified MWCNTs were then poured into a 0.1 M solution of LiBH_4 (Sigma-Aldrich, purity >95%) in methyl tert-butyl ether (MTBE) (Sigma-Aldrich, anhydrous, 99.8%). The suspension was stirred for 12 h and the solvent was then removed by evaporation under rotary pump vacuum. Three samples with different LiBH_4 :MWCNTs mass ratio were prepared: sample 1c (1:1.8), sample 2 (1:0.9), and sample 3 (1:0.45). The MWCNTs used for this first set of samples was ball milled for 90 min. In order to better understand the effect of carbon on the dehydrogenation kinetics of LiBH_4 , samples with the same composition of sample 1c (having the highest carbon content) were prepared using MWCNTs milled for 0, 15, 90 and 600 min; in the following discussion these samples will be called sample 1a, sample 1b, sample 1c, sample 1d, respectively.

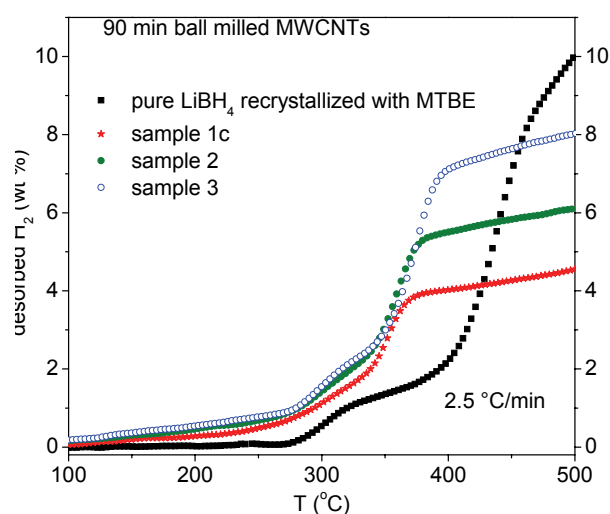


Figure 7.6 Comparison of dehydrogenation profiles of samples 1c, 2, 3, and pure LiBH_4 recrystallized with MTBE. The wt% of desorbed H_2 is related to the total weight of the sample.

7.3.2 Kinetic, structural and morphological characterization of samples

TPD measurements have been performed as explained in the previous section. Before the TPD measurements, the sample chamber with the sample inside was evacuated at room temperature. The total volume of the Sievert's device was chosen large enough to avoid kinetics being affected by the increase of hydrogen pressure during the measurements. The temperature was then raised from ambient to 507 °C at a heating rate of 2.5 °C/min. Figure 7.6 shows that the dehydrogenation reaction of supported LiBH_4 has almost the same two step behaviour for samples 1c, 2 and 3: the first onset occurs at about 270 °C both for all the infiltrated samples and for pure LiBH_4 obtained after re-crystallization in MTBE; the second onset occurs at about 340 °C, 60 °C lower than that of pure LiBH_4 . The results are in agreement with those reported by Yu et al. [7.8].

XRD diffraction measurements were carried out on samples protected with a thin kapton foil (8 μm). The XRD patterns of sample 1c as prepared and after complete dehydrogenation are reported in figure 7.7. The as prepared sample displays the broad peaks of carbon along with peaks of LiBH_4 , while the decomposed sample presents, in addition to the peaks of carbon, weak peaks of LiH and Li_2C_2 .

Figure 7.8 reports the effect of ball milling on the SSA of MWCNTs, which increases with ball milling time and is almost twice after 600 min milling with respect to the as received material.

Scanning electron microscopy (SEM) micrographs were acquired with a JEOL JSM-6490 Scanning Electron Microscope operated at 20 kV. From the SEM micrographs shown in figure 7.9 it is possible to see the evolution of nanotubes morphology with ball milling time. Figure 7.9(a) shows the morphology of the as received nanotubes with an average diameter of about 60 nm. As already reported in [7.19, 7.20], carbon nanotubes are shortened by the ball milling process while the average diameter remains unchanged.

This is shown in figures 7.9(b) and 7.9(c) for the 15 min and 90 min MWCNTs, respectively. The material in both cases looks more compact with respect to the as received one. After 600 min ball milling the structure of nanotubes vanishes resulting in the typical morphology of an amorphous-like carbon.

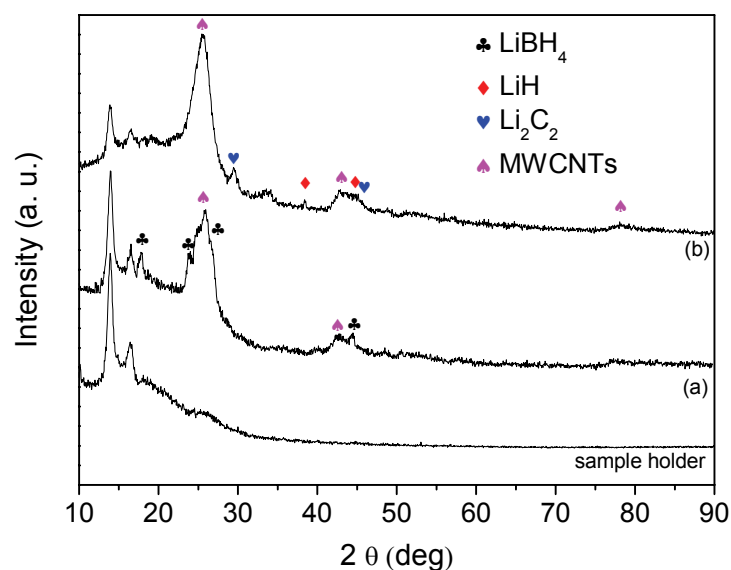


Figure 7.7 Comparison of the XRD patterns of sample 1c as prepared (a) and after dehydrogenation (b). The XRD profile of Kapton foil (sample holder) is also reported.

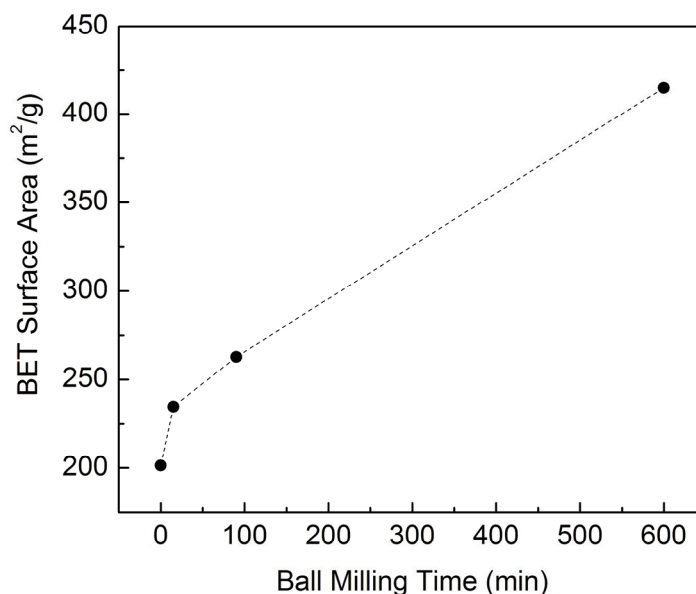


Figure 7.8 BET surface area of MWCNTs as a function of high energy ball milling time.

The BET surface area of as received and ball milled MWCNTs were determined from N_2 adsorption experiments at 77 K. The samples were degassed for 6 h at 300 °C to remove any moisture or adsorbed contaminants that might be present on the surface. It is clearly evident from figure 7.10 that increasing the SSA of the carbonaceous support leads to the decreasing of the onset temperature of the main dehydrogenation process, going from about 350 °C in the

case of the as received MWCNTs to about 310 °C in the case of sample 1d. Hence, the SSA of the carbonaceous support seems to have an important effect on the dehydrogenation kinetics of LiBH₄.

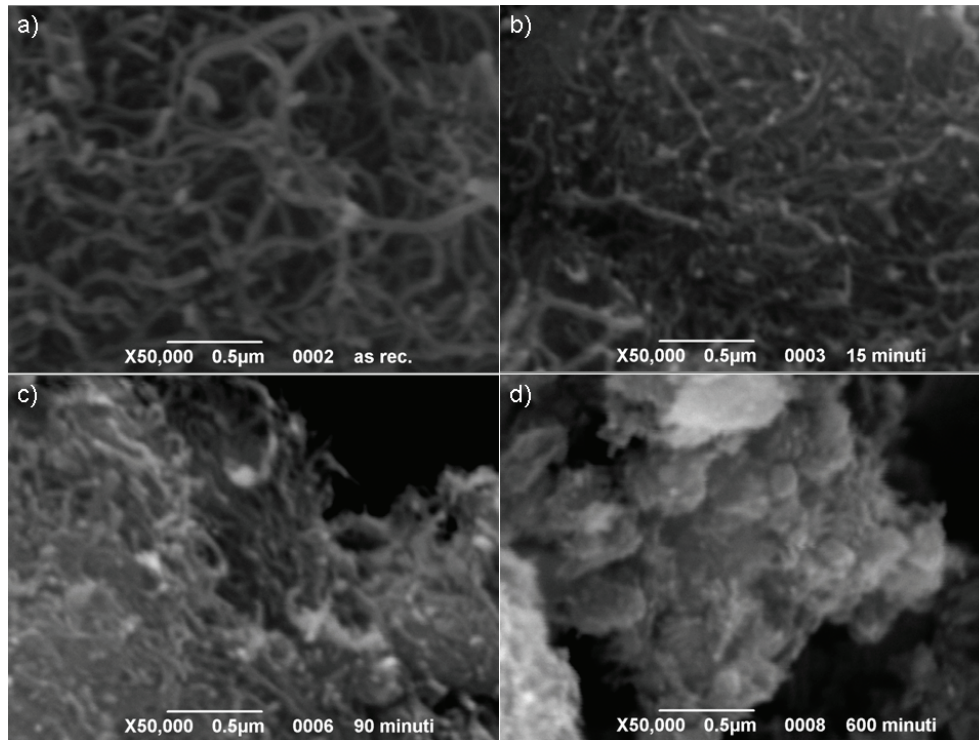


Figure 7.9 SEM micrographs of MWCNTs as received (a) and high energy ball milled for 15 min (b), 90 min (c), 600 min (d).

7.3.3 Interpretation of kinetic mechanism

This effect may be explained considering the surface of the support not only as a mean to disperse the active material, but also as a nucleation centre for the solid decomposition products of LiBH₄. This complex hydride melts at 268 °C [7.21] then, when dehydrogenation starts, some solid LiH and B particles start nucleating from liquid LiBH₄ along with hydrogen desorption. The high surface area of the carbonaceous material probably acts as a centre for heterogeneous nucleation of the decomposition products. If we consider a spherical cluster having radius r that nucleates from the melt, the free energy needed for its nucleation is:

$$\Delta G = \frac{4}{3}\pi r^3 \Delta G_v + 4\pi r^2 \sigma \quad (7.4)$$

where ΔG_v is the free energy gain for volume unit and σ the interfacial energy [7.22]. To increase the radius of the nuclei the system needs free energy if $\frac{d\Delta G}{dr} > 0$ and the growth of the nuclei is limited by nucleation. This occurs when the radius is less than the critical radius r_c defined as:

$$r_c = -\frac{2\sigma}{\Delta G_v} \quad (7.5)$$

to which corresponds a maximum of free energy:

$$\Delta G^* = \frac{16\pi\sigma^3}{3(\Delta G_v)^2} \quad (7.6)$$

When the nuclei reach the radius r_c the energy barrier ΔG^* for nucleation has been overcome and nucleation proceeds. If the products nucleate on a surface wetting it with a contact angle θ , the heterogeneous nucleation process occurs and the energy barrier for nucleation is:

$$\Delta G_{hetero}^* = \Delta G^* \cdot S(\theta) \quad (7.7)$$

where $S(\theta)$ is the shape factor defined as:

$$S(\theta) = \frac{(2 + \cos\theta)(1 - \cos\theta)^2}{4} \quad (7.8)$$

$S(\theta)$, that is smaller than 1, corresponds to the ratio of the volume of the particle nucleated on the surface and the volume of the sphere having the same radius of curvature r . This means that in this case the nuclei that can overcome the nucleation energy barrier have the same critical radius but need a much smaller volume. Hence, it is obvious that increasing the available surface for heterogeneous nucleation (the SSA of the support), it is possible to increase the reaction kinetics. According to this interpretation it could be possible in principle to further reduce the dehydrogenation temperature of LiBH_4 choosing a high surface area support on which the contact angle of solid decomposition products is smaller than in the case of a carbonaceous support. Work is in progress to verify this hypothesis.

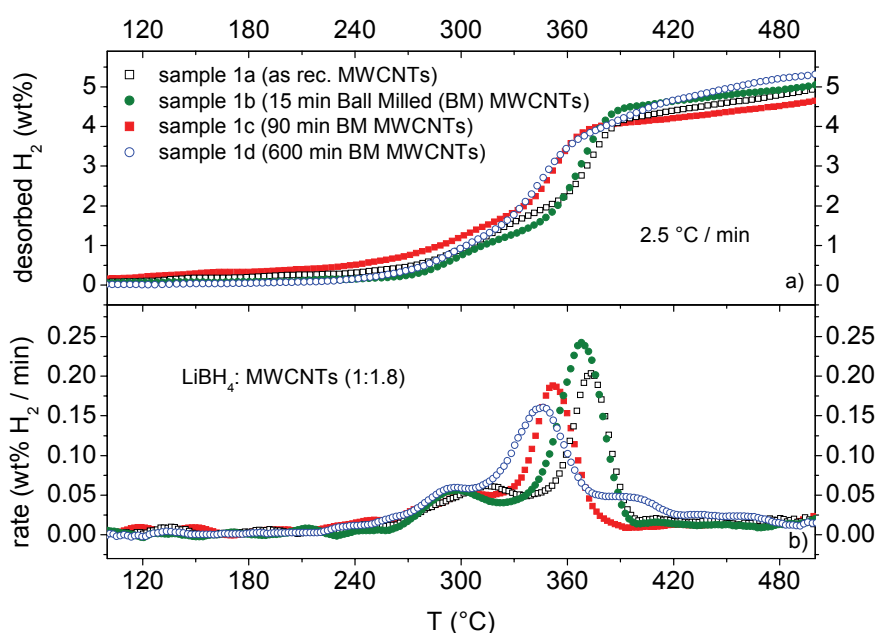


Figure 7.10 Dehydrogenation profiles of samples 1a, 1b, 1c, 1d (a) and corresponding dehydrogenation rates (b). The wt% of desorbed H_2 is related to the total weight of the sample.

7.3.4 Thermodynamic characterization

In the previous discussion only kinetics has been considered. Anyway, the infiltration of LiBH_4 in an high surface area material could also lead to the formation of nanoparticles that, due to a size effect, could show modified and favourable thermodynamic properties. In order to check this possibility, the PCI curves of figure 7.11 have been measured at different temperatures during the desorption of sample 1d.

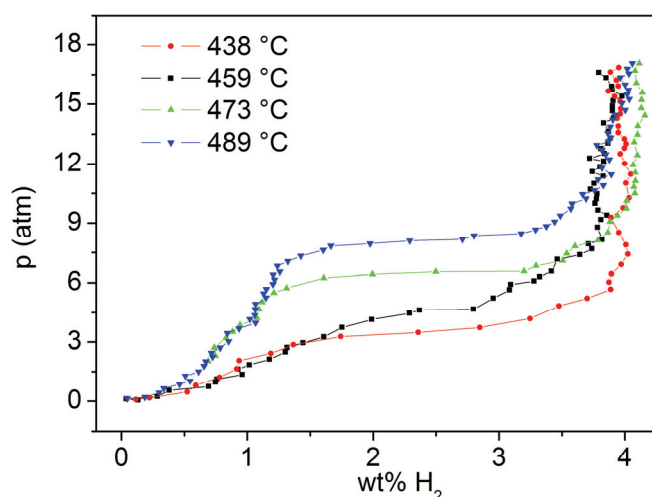


Figure 7.11 Pressure Composition Isotherms obtained during dehydrogenation of sample 1d.

Usually, the poor kinetics of LiBH_4 does not allow to measure equilibrium pressures, but in this case it has been possible thanks to the improved kinetics. The corresponding van't Hoff plot is shown in figure 7.12. The estimated values for dehydrogenation enthalpy and entropy changes obtained by fitting the experimental data with the van't Hoff law are $\Delta H^d = (78 \pm 5)$ kJ/mol H_2 and $\Delta S^d = (120 \pm 7)$ J/(K·mol H_2). The equilibrium pressure p_{eq} for each PCI has been evaluated at the inflexion point of the curve.

The estimated values are in good agreement with $\Delta H^d = 74$ kJ/mol H_2 and $\Delta S^d = 115$ J/(K·mol H_2), recently derived for pure LiBH_4 by Mauron et al. [7.23] using the same law. In our case the equilibrium pressure looks slightly lower probably because of not perfectly reached equilibrium, due to poor kinetics especially at the lower temperatures. This means that the dispersion of LiBH_4 on high surface area carbonaceous supports does not lead to thermodynamic destabilization of LiBH_4 as argued by Yu et al. [7.8].

The results reported in this section have been published in [7.24].

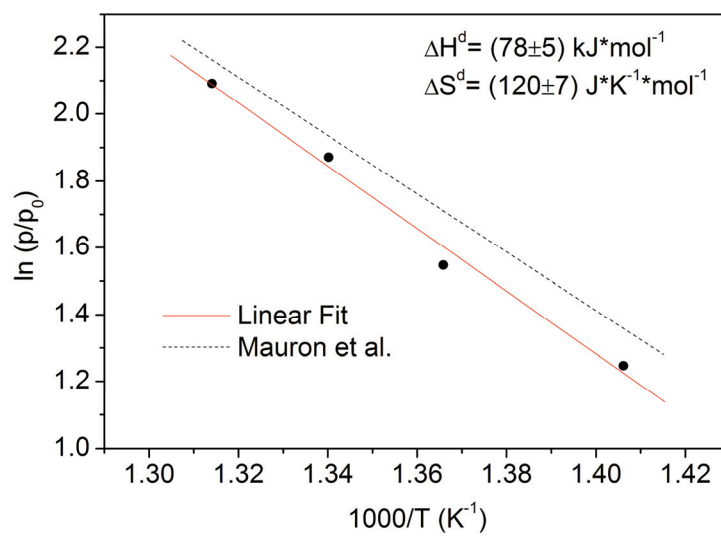


Figure 7.12 Van't Hoff plot related to Pressure Composition Isotherms of figure 7.11. The plot published in ref. [7.23] is also shown.

- [7.1] Fieser M., *Reagents for Organic Synthesis* (1989) vol 14, (New York: Wiley).
- [7.2] Brown H. C., Choi Y. M., Narasimhan S., *Addition Compounds of Alkali Metal Hydrides. 22. Convenient Procedures for the Preparation of Lithium Borohydride from Sodium Borohydride and Borane-Dimethyl Sulfide in Simple Ether Solvents*, Inorg. Chem. (1982) **21**, 3657.
- [7.3] Schlesinger H. I., Brown H. C., Hyde E. K., *The Preparation of Other Borohydrides by Metathetical Reactions Utilizing the Alkali Metal Borohydrides*, J. Am. Chem. Soc. (1953) **75**, 209.
- [7.4] Friedrichs O., Buchter F., Borgschulte A., Remhof A., Zwicky C. N., Mauron Ph., Biemann M., Züttel A., *Direct synthesis of Li[BH₄] and Li[BD₄] from the elements*, Acta Mater. (2008) **56**, 949.
- [7.5] Züttel A., Borgschulte A., Orimo S., *Tetrahydroborates as new hydrogen storage materials*, Scripta Mater. (2007) **56**, 823.
- [7.6] Orimo S., Nakamori Y., Kitahara G., Miwa K., Ohba N., Towata S., Züttel A., *Dehydriding and rehydriding reactions of LiBH₄*, J. Alloys Compd. (2005) **404-406**, 427.
- [7.7] Vajo J. J., Olson G. L., *Hydrogen storage in destabilized chemical systems*, Scripta Mater. (2007) **56**, 829.
- [7.8] Yu X. B., Wu Z., Chen Q. R., Li Z. L., Weng B. C., Huang T. S., *Improved hydrogen storage properties of LiBH₄ destabilized by carbon*, Appl. Phys. Lett. (2007) **90**, 034106.
- [7.9] Cahen S., Eymery J. B., Janot R., Tarascon J. M., *Improvement of the LiBH₄ hydrogen desorption by inclusion into mesoporous carbons*, J. Power Sources (2009) **189**, 902.
- [7.10] Wang P., Fang Z., Ma L., Kang X., Wang P., *Effect of carbon addition on hydrogen storage behaviors of Li-Mg-B-H system*, Int. J. Hydrogen Energ. (2009) (in press), doi:10.1016/j.ijhydene.2009.07.041.
- [7.11] Vajo J. J., Mertens F., Ahn C. C., Bowman R. C., Fultz B., *Altering Hydrogen Storage Properties by Hydride Destabilization through Alloy Formation: LiH and MgH₂ Destabilized with Si*, J. Phys. Chem. B (2004) **108**, 13977.
- [7.12] Tsomaya K. P., Gabunia D. L., Tavadze F. N., *An investigation of dispersed fractionated boron powders*, J. Less-Comm. Met. (1979) **67**, 425.

- [7.13] Morris M. A., Morris D. G., *Ball-milling of elemental powders—compound formation and/or amorphization*, J. Mater. Sci. (1991) **26**, 4687.
- [7.14] Züttel A., Wenger P., Rentsch S., Sudan P., Mauron Ph., Emmenegger Ch., *LiBH_4 a new hydrogen storage material*, J. Power Sources (2003) **118**, 1.
- [7.15] Gunn S. R. Green L. G., *Heat of Formation of Deuterated Diborane*, J. Chem. Phys. (1962) **36**, 1118.
- [7.16] Orimo S., Nakamori Y., Eliseo J. R., Züttel A., Jensen C. M., *Complex hydrides for hydrogen storage*, Chem. Rev. (2007) **107**, 4111.
- [7.17] Soldate A. M., *Crystal structure of sodium borohydride*, J. Am. Chem. Soc. (1947) **69**, 987.
- [7.18] Agresti F., Khandelwal A., *Evidence of formation of LiBH_4 by high-energy ball milling of LiH and B in a hydrogen atmosphere*, Scripta Mater. (2009) **60**, 753.
- [7.19] Pierard N., Fonseca A., Konya Z., Willems I., Van Tendeloo G., Nagy J. B., *Production of short carbon nanotubes with open tips by ball milling*, Chem. Phys. Lett. (2001) **335**, 1.
- [7.20] Pierard N., Fonseca A., Colomer J. F., Bossuot C., Benoit J. M., Van Tendeloo G., Pirard J. P., Nagy J. B., *Ball milling effect on the structure of single-wall carbon nanotubes*, Carbon (2004) **42**, 1691.
- [7.21] Lide D. R., *Handbook of Chemistry and Physics* (84th edition), (CRC Press).
- [7.22] Abraham F. F., *Homogeneous nucleation theory* (1974), (New York: Academic Press)
- [7.23] Mauron Ph., Buchter F., Friedrichs O., Remhof A., Biemann M., Zwicky C. N., Züttel A., *Stability and Reversibility of LiBH_4* , J. Phys. Chem. B (2008) **112**, 906.
- [7.24] Agresti F., Khandelwal A., Capurso G., Lo Russo S., Maddalena A., Principi G., *Improvement of dehydrogenation kinetics of LiBH_4 dispersed on modified multi-walled carbon nanotubes*, Nanotechnology (2010) **21**, 065707.

Chapter 8

Concluding remarks

The goal of this thesis is to investigate and improve among several classes of materials promising systems for solid state hydrogen storage. The investigation started from systems almost ready for niche applications, moving towards other very promising systems but still far from practical use.

Among the AB₂ alloys, the TiCr_{1.78-x}Mn_x system is one of the more promising for the use in hybrid hydrogen storage vessels, combining the advantages of high pressure and hydrogen hosted in a metal lattice. The results reported in this thesis show that the TiCr_{1.78-x}Mn_x compounds under hydrogen pressure absorb considerable amounts of hydrogen at room temperature without needing any surface activation. The effect of partial substitution of Cr with Mn has been studied and it has been found that increasing the Mn content leads to some interesting advantages for practical applications, such as improved gravimetric hydrogen capacity, flatter plateau and lower hysteresis.

It is discussed and proposed the controlled compaction of the Mg/MgH₂ system in form of pellets, a novel approach to overcome the kinetic and hydrogen capacity degradation found during the scaling-up of this hydrogen storage system in form of powder. The mechanical strength of pellets made by catalysed MgH₂ mixed with crystalline aluminium powder as binding agent has been tested after a number of hydrogen a/d cycles. It is found that a pre-heating treatment of the pellet to the temperature sufficient to form intermetallic phases and/or solid Mg-Al solutions increases the resulting performance of the material, as concerns both functional and mechanical stability. The best mechanical stability has been observed in the case of pellets containing 5 wt% Al. These pellets show a constant 5.3 wt% hydrogen

capacity up to 50 cycles and constant kinetics after 10 cycles. The enhanced stability of the pellets in this case has been attributed to the presence of solid solution of Al in Mg, leading to both improved ductility and mechanical strength. Work is in progress to better understand, with a higher resolution investigation, the microstructural evolution of the pellets in the different stages of a/d cycling. Moreover, the preparation of a small vessel to study the hydrogen a/d behaviour of a metal hydride in form of pellets instead of powder is under way.

The effect of high energy ball milling on the a/d kinetics of the composite system $\text{LiNH}_2/\text{MgH}_2$ is reported. A milling time of 24h or longer gives a better kinetics compared to 2h and 12h milled samples, especially during hydrogen absorption. After 48 h of milling the system shows an higher hydrogen capacity with respect to the other samples, likely due to a reciprocal better dispersion of LiNH_2 and MgH_2 which leads to a more efficient activation of the material. The kinetics improvement is due to the reduced average crystallite size, enhancing the solid-solid reactivity and shortening the diffusion paths.

The main problems limiting the practical use of LiBH_4 , one of the most promising materials for hydrogen storage, have been faced: reaction reversibility and slow dehydrogenation kinetics. Concerning reversibility, it is proposed a novel synthesis of LiBH_4 at room temperature by reactive high energy ball milling of its decomposition products under a hydrogen atmosphere. Increasing hydrogen pressure, time of milling and hardness of milling medium leads to the enhancement of the yield of formation of LiBH_4 . Moreover, the amorphous-like state of produced LiBH_4 and its chemical surrounding in the as milled samples seem to considerably enhance the decomposition kinetics. Pure LiBH_4 has been obtained from milled sample by solvent separation. Concerning the problem of slow decomposition kinetics, it has been shown that LiBH_4 dispersed on MWCNTs by solvent infiltration shows a decreased dehydrogenation temperature with respect to the pure material by more than 60 °C. The dehydrogenation temperature of LiBH_4 further decreases with increasing the specific surface area of MWCNTs, likely due to heterogeneous nucleation of decomposition products or intermediate phases from liquid LiBH_4 on the carbon surface. Finally, it has been concluded from equilibrium pressure measurements at different temperatures that the dispersion of LiBH_4 on the high SSA of MWCNTs does not seem to lead to thermodynamic destabilization with respect to pure material due to size effect. Further investigation is under way in order to study the same effect on other borohydrides as $\text{Mg}(\text{BH}_4)_2$ and $\text{Ca}(\text{BH}_4)_2$.

Curriculum Vitae

Filippo Agresti was born in Policoro (Italy) on July 9th 1980. 2006, Materials Science Degree (110/110) at University of Padova, with graduation work entitled "Study on magnesium hydrides for solid state hydrogen storage". Since Jan. 2007, PhD student at the University of Padova, Materials Science and Engineering School, research on materials for solid state hydrogen storage under the supervision of Prof. Giovanni Principi.

List of publications

1. F. Agresti, A. Khandelwal, G. Capurso, S. Lo Russo, A. Maddalena, S. Gialanella, G. Principi, *Improvement of dehydrogenation kinetics of LiBH₄ dispersed on modified multi-walled carbon nanotubes*, Nanotechnology (2010) **21**, 065707.
2. Khandelwal, F. Agresti, G. Capurso, S. Lo Russo, A. Maddalena, S. Gialanella, G. Principi, *Pellets of MgH₂-based composites as practical material for solid state hydrogen storage*, Int. J. Hydrogen Energ. (in press).
3. F. Agresti, A. Khandelwal, A. Maddalena, G. Principi, S. Lo Russo, *Recent achievements on materials for hydrogen storage*, International Journal of Nuclear Hydrogen Production and Applications (2009) **2**, 122–136.
4. S. Bianco, M. Giorcelli, S. Musso, M. Castellino, F. Agresti, A. Khandelwal, S. Lo Russo, M. Kumar, Y. Ando, A. Tagliaferro, *Hydrogen adsorption in several types of Carbon Nanotubes*, J. Nanosci. Nanotechnol. (2009) **9**, 6806-6812.
5. F. Agresti, A. Khandelwal, *Evidence of formation of LiBH₄ by high energy ball-milling of LiH and B in a hydrogen atmosphere*, Scripta Mater. (2009) **60**, 753-755.

6. Glage, R. Ceccato, I. Lonardelli, F. Girardi, F. Agresti, G. Principi, A. Molinari, S. Gialanella, *A powder metallurgy approach for the production of a MgH_2 -Al composite material*, J. Alloys Compd. (2009) **521-522**, 273-280.
7. Molinas, A.A. Ghilarducci, M. Melnichuk, H.L. Corso, H.A. Peretti, F. Agresti, A. Bianchin, S. Lo Russo, A. Maddalena and G. Principi, *Scaled-up production of a promising Mg-based hydride for hydrogen storage*, Int. J. Hydrogen Energy (2009) **34**, 4597-4601.
8. F. Agresti, S. Lo Russo, A. Maddalena, G. Principi, G. Mazzolai, B. Coluzzi, A. Biscarini, F. M. Mazzolai and A. Tuissi, *Reaction of hydrogen with the Laves phase (C14) $TiCr_{1.78-x}Mn_x$ compounds*, Mater. Sci. Eng. A (2009) **521-522**, 143-146.
9. G. Mazzolai, B. Coluzzi, A. Biscarini, F.M. Mazzolai, A. Tuissi, F. Agresti, G. Principi, S. Lo Russo, *Hydrogen diffusion in the Laves-phase compound $TiCr_{1.78}$* , Mater. Sci. Eng. A (2009) **521-522**, 139-142.
10. G. Principi, F. Agresti, A. Maddalena, S. Lo Russo, *The problem of solid state hydrogen storage*, Energy (2009) **34**, 2087-2091.
11. M. Verga, F. Armanasco, C. Guardamagna, C. Valli, A. Bianchin, F. Agresti, S. Lo Russo, A. Maddalena, G. Principi, *Scaling up effects of Mg hydride in a temperature and pressure controlled hydrogen storage device*, Int. J. Hydrogen Energy (2009) **34**, 4602-4610.
12. G. Mazzolai, B. Coluzzi, A. Biscarini, F.M. Mazzolai, A. Tuissi, F. Agresti, S. Lo Russo, A. Maddalena, P. Palade and G. Principi, *Hydrogen-storage capacities and H diffusion in bcc $TiVCr$ alloys*, J. Alloys Compd. (2008) **466**, 133-139.
13. B. Coluzzi, A. Biscarini, G. Mazzolai, F.M. Mazzolai, A. Tuissi, F. Agresti, S. Lo Russo, A. Maddalena, P. Palade, G. Principi, *Physical properties of hydrogen in $TiVMnCr$ bcc alloys as deduced from hydrogen absorption/desorption and mechanical spectroscopy experiments*, J. Alloys Compd. (2008) **456**, 118-124.
14. R. Gupta, F. Agresti, S. Lo Russo, A. Maddalena, P. Palade, G. Principi, *Structure and hydrogen storage properties of MgH_2 catalysed with La_2O_3* , J. Alloys Compd. (2008) **450**, 310-313

15. S. Barison, F. Agresti, S. Lo Russo, A. Maddalena, P. Palade, G. Principi, G. Torzo, *A study of the $\text{LiNH}_2\text{-MgH}_2$ system for solid state hydrogen storage*, J. Alloys Compd. (2008) **459**, 343-347.
16. S. Lo Russo, F. Agresti, S. Barison, A. Maddalena, P. Palade, G. Principi, G. Torzo, *Nanomaterials for solid state hydrogen storage*, Recent Res. Devel. Mat. Sci. (2007) **7**, 81-90 ISBN: 81-308-0145-0.
17. G. Principi, P. Palade, S. Sartori, A. Maddalena, F. Agresti, S. Lo Russo, B. Molinas, H. A. Peretti, *Investigations on light metal hydrides at Padova, the city of San Antonio*, Advanced Materials for Energy conversion III (2006) 109-115.

Presentations at scientific meetings

G. Principi, F. Agresti, A. Khandelwal, A. Maddalena, S. Lo Russo, *Recent Achievements on nanocrystalline materials for solid state hydrogen storage*, oral presentation at VII National INSTM Conference on Material Science and Technology, June 9-12 2009, Tirrenia, Italy.

A. Khandelwal, F. Agresti, G. Capurso, S. Lo Russo, A. Maddalena, G. Principi, *Improvement of decomposition properties of LiBH_4 dispersed on multi-walled carbon nanotubes*, poster presentation at Metal-Hydrogen Systems Gordon Conference, July 12-17 2009, Barga (LU), Italy.

F. Agresti, A. Khandelwal, *Evidence of formation of LiBH_4 by high energy ball-milling of LiH and B in a hydrogen atmosphere*, poster presentation at 3rd Symposium Hydrogen and Energy, January 25-30 2009 Braunwald, Switzerland.

F. Agresti, S. Lo Russo, A. Maddalena, G. Principi, G. Mazzolai, B. Coluzzi, A. Biscarini, F. M. Mazzolai and A. Tuissi, *Reaction of hydrogen with the Laves phase (C14) $\text{TiCr}_{1.78-x}\text{Mn}_x$ compounds*, poster presentation at MH2008 Conference, June 24-28 2008, Reykjavik, Iceland.

M. Verga, F. Armanasco, C. Guardamagna, C. Valli, A. Bianchin, F. Agresti, S. Lo Russo, A. Maddalena, G. Principi, *Scaling up effects of Mg hydride in a temperature and pressure controlled hydrogen storage device*, oral presentation at 2nd Symposium Hydrogen and Energy, January 21-25 2008 Braunwald, Switzerland.

S. Barison, F. Agresti, S. Lo Russo, A. Maddalena, P. Palade, G. Principi, G. Torzo, *Li amide mixed with Mg hydride, a promising system for solid state hydrogen storage*, oral presentation at WHTC Convention, November 20-25 2007, Montecatini ,Italy.

S. Barison, F. Agresti, S. Lo Russo, A. Maddalena, P. Palade, G. Principi, G. Torzo, *A study of the $\text{LiNH}_2\text{-MgH}_2$ system for solid state hydrogen storage*, poster presentation at Metal-Hydrogen Systems Gordon Conference, July 8-13 2007, Waterville, USA

Acknowledgements

I would like to thank Prof. Giovanni Principi for the supervision of this work, for the very useful discussions we had on scientific topics during these last years, for his incomparable willingness and for the pleasant company during conferences.

My most sincere gratitude goes to Prof. Sergio Lo Russo Prof. Amedeo Maddalena for helpful conversations and support to my work and for the advices on experiments and instrumental setup. They can be considered as co-tutors.

Thanks to Petru Palade and Sabrina Sartori who introduced me in this field and gave the basic knowledge to continue my work.

Thanks to my colleagues Silvio Barison, Alvisè Bianchin, Ashish Khandelwal and Giovanni Capurso for their help in the laboratory during these years and for their friendship.

Thanks to Prof. Stefano Gialanella for useful conversations and help with SEM measurements.

Thanks to Prof. Fabio Mazzolai for proposing the work on the $\text{TiCr}_{1.78-x}\text{Mn}_x$ system and for providing samples.

Thanks to Prof. Andreas Züttel and Andreas Borgschulte for giving me the opportunity to spend a very useful and instructive period in their laboratories.

Finally, I would like to specially thank my family, Barbara and all my friends for the continuous support and love.